DISSERTATION

QUANTIFYING FUNCTION IN THE ZEBRAFISH EMBRYONIC HEART:

A STUDY ON THE ROLE OF TIMED MECHANICAL CUES

Submitted by

Brennan Michael Johnson

Graduate Degree Program in Bioengineering

In partial fulfillment of the requirements

For the Degree of Doctor of Philosophy

Colorado State University

Fort Collins, Colorado

Summer 2014

Doctoral Committee:

Advisor: Lakshmi Dasi
Co-Advisor: Deborah Garrity

John Kisiday
Christopher Orton
Karan Venayagamoorthy

ABSTRACT

QUANTIFYING FUNCTION IN THE ZEBRAFISH EMBRYONIC HEART: A STUDY ON THE ROLE OF TIMED MECHANICAL CUES

Congenital heart defects are a relatively common problem, yet the cause is unknown in the large majority of cases. A significant amount of past research has shown that there is a link between altered blood-induced mechanical stress and heart development. However, very little research has been done to examine the effect of altered loading timing. During embryonic development, the heart undergoes a drastic change in morphology from its original valveless tube structure to a complete multi-chambered pump with valves. Blood flow dynamics are consequently altered significantly as well. Given the changes occurring through this period, it is hypothesized that significant and persistent decreases in heart function occur when cardiac loading is altered during certain time windows of early development.

The main objectives of this work were to (1) develop a methodology to quantify heart function in the embryonic zebrafish from high-speed bright field images, (2) develop a model for temporary and noninvasive alteration of cardiac loading, and (3) apply the methodology to normal and treated embryos to determine whether certain time windows of altered loading are more impactful than others. Results indicated that altered loading during the tube and early looping stages of development produce persistent changes in heart morphology along with accompanying decreases in cardiac function. Altered

loading during late cardiac looping resulted in temporary changes in function which did not persist through the latest time point measured.

This work has produced extensive tools for quantifying heart function from high speed images and presents a new model for altered cardiac loading in the zebrafish. Results support the hypothesis that the heart is more sensitive to altered loading during certain windows in development. This provides new insight into how congenital defects may develop and sets the stage for future experiments investigating the effects of altered loading on heart development.

ACKNOWLEDGEMENTS

I would like to acknowledge the people who have helped me throughout my graduate career. First, I would like to recognize Dr. Prasad Dasi. You have been an outstanding advisor. I am extremely thankful and lucky to have had the chance to work with you over the past five years. Should my career lead down a similar path, I hope that I will be as good a leader and mentor as you have been. I also want to thank my co-advisor, Dr. Debbie Garrity. Your careful edits and thoughtful insights have greatly improved every publication and poster I've run past you. Dr. Chris Orton, I learned a lot in my brief rotation in your lab and I cannot even express how much respect I have for you. From watching you perform open-heart surgeries to getting smoked by your outrageous cycling endurance, your skills and dedication are an inspiration to me. Dr. John Kisiday and Dr. Karan Venayagamoorthy, you have both provided extremely helpful feedback that has kept me focused on the big picture, and you have helped me realize what it takes to be a PhD-level researcher.

I would also like to acknowledge the members of the Dasi and Garrity labs. I have enjoyed working with you and the feedback and friendship you've all provided over the years is much appreciated. I would especially like to thank John Fitts—I appreciate the time you've spent teaching me various lab techniques and brainstorming new zebrafish methods with me. You are one of the nicest and most genuine people I've met. Dr. Niel Stafford, although I was supposed to be teaching you zebrafish protocols, I think I actually learned more from you—your continuous scientific inquiries and logical

approach to solving problems has inspired me as a researcher and engineer. Bryce Schroder, although we've been through some frustrating and demoralizing times in the optical tweezers lab, I'm proud of the work we've done together, I'm excited to see where it leads in the future.

Of course I would also like to acknowledge my parents for raising me to be the person I am. And finally, I want to acknowledge my wonderful fiancée, Katie. You have been there for me throughout my entire graduate journey and I'm looking forward to spending the rest of my life by your side.

TABLE OF CONTENTS

ABSTRACT ii

ACKNOWLEDGEMENTS iv

TABLE OF CONTENTS vi

LIST OF FIGURES xi

CHAPTER 1: HYPOTHESIS AND AIMS 1

1.1 Chapter Introduction 1

1.2 Aim 1 2

1.3 Aim 2 2

1.4 Aim 3 3

1.5 Overview of Results 4

1.6 Dissertation Organization 5

CHAPTER 2: LITERATURE REVIEW 6

2.1 Congenital Heart Defect Statistics 6

2.2 Epigenetics 6

2.3 Animal Models in Heart Development Research 7

2.4 Early Heart Development in the Zebrafish 10

2.5 Pumping Mechanics of the Embryonic Heart 13

2.6 Mechanical Stress and Fluid Dynamics in the Embryonic Heart 16

2.7 Cellular Response to Mechanical Stress 21

2.8 Effect of Blood Flow on Heart Development 24

2.9 Gene Expression and Mechanical Force 28
2.10 Imaging Modalities 29
2.11 Measuring Embryonic Heart Function 32
2.12 Chapter Summary 36
CHAPTER 3: METHODS 37
3.1 Chapter Introduction 37
3.2 Zebrafish Breeding and Egg Handling 37
3.3 Zebrafish Imaging 38
3.4 Alternate Zebrafish Preparation Protocols 40
CHAPTER 4: AIM 1 43
4.1 Chapter Introduction 43
4.2 Failed Approach 1: Particle Image Velocimetry 43
4.3 Failed Approach 2: Manual Cell Tracking 47
4.4 Overview of the Final Methodology Used for Calculating Heart Function 49
4.5 Image Intensity Normalization 50
4.6 Isolation of Movement within Image Sequences 51
4.7 Creation of Spatiotemporal Plots 52
4.8 Advantages and Limitations of ST Plots 54
4.9 Location of ST Plot Measurements 55
4.10 Determination of the Profile Coefficient 56
4.11 Determination of ST Plot Streak Angle using Radon Transforms 59
4.12 Signal to Noise of Velocity 62
4.13 Measurement of Cardiac Lumen Diameter 62

4.14 Estimation of Derived Parameters 64
4.15 Automated Calculation of Heart Rate 66
4.16 Test Experiment Setup 67
4.17 Test Experiment Results 68
4.18 Test Experiment Discussion 71
4.19 Advantages of Calculations based on Flow Rate 73
4.20 Introduction to Methodology Validation and Modifications 75
4.21 Effect of Bin Size 75
4.22 Effect of Averaging Span 77
4.23 Reference Line Orientation Error 79
4.24 Streak Angle Determination Error 80
4.25 Validation of Radon Streak Angle Measurement 82
4.26 Synthetic Datasets for Validation 85
4.27 Imaging Limitations 88
4.28 Chapter Summary 90
CHAPTER 5: AIM 2 91
5.1 Chapter Introduction 91
5.2 Pumping Mechanics Introduction 91
5.3 Creation of Blood Velocity Vector Fields 92
5.4 Contraction Wave Tracking 93
5.5 Heart Kinematics at 30 hpf 96
5.6 Blood Flow at 30 hpf 97
5.7 Heart Kinematics at 36 hpf 98

5.8 Blood Flow at 36 hpf 99
5.9 Heart Kinematics at 48 hpf 99
5.10 Blood Flow at 48 hpf 100
5.11 Discussion of Transitional Pumping Mechanics 100
5.12 Pumping Mechanics Summary 106
5.13 Quantitatively Benchmarking Heart Function 106
5.14 Benchmark Measurement Methods 107
5.15 Benchmark Results as 48 and 55 hpf 109
5.16 Discussion 112
5.17 Chapter Summary 113
CHAPTER 6: AIM 3 114
6.1 Chapter Introduction 114
6.2 Centrifugation as a Method for Altering Cardiac Loading 114
6.3 Centrifugation Experiment Methods 116
6.4 Centrifugation: Morphological Results 118
6.5 Centrifugation: Blood Flow Results 122
6.6 Centrifugation: Discussion 125
6.7 Study Limitations 128
6.8 Chapter Summary 129
CHAPTER 7: FUTURE WORK 131
7.1 Chapter Introduction 131
7.2 Continued Centrifugation Studies 131
7.3 Gene Expression Studies 132

7.4 Computational Fluid Dynamics 133

CHAPTER 8: CONCLUSION 134

CHAPTER 9: ORIGINAL CONTRIBUTIONS 136

9.1 Peer-Reviewed Publications 136

9.2 Conference Publications 136

9.3 Conference/Seminar Oral Presentations 136

9.4 Conference Poster/Video Presentations 137

9.5 Publications in Progress 137

REFERENCES 138

LIST OF FIGURES

Figure 2.1 Chick embryo 8
Figure 2.2 Zebrafish embryo scale and transparency 9
Figure 2.3 Key stages of zebrafish heart development 11
Figure 2.4 Zebrafish Heart Morphology at 48 and 120 hpf 12
Figure 2.5 Proposed impedance pump wave mechanics 13
Figure 2.6 Hoop Stress and Pressure within the Heart 16
Figure 2.7 Shear Stress along the Heart Wall 17
Figure 2.8 Plot of Shear Stress vs. Shear Rate for Blood 20
Figure 2.9 Endothelial Cell Alignment with Flow In Vitro 21
Figure 2.10 Cellular Response to Shear Stress 22
Figure 2.11 Signaling Cascades Resulting from Mechanical Stretch on Cell 23
Figure 2.12 Septum Defect Resulting from Vitelline Vein Ligation 25
Figure 2.13 Obstruction of Flow in Zebrafish Heart 27
Figure 2.14 PIV Results from Hove et al. 35
Figure 2.15 PIV Results from Jamison et al. 36
Figure 3.1 Schematic of Equipment 40
Figure 3.2 FEP Tubing for Distortion-free Zebrafish Imaging 42
Figure 4.1 PIV Results 45
Figure 4.2 Regions used for Calculating Blood Velocity at Key Points 48
Figure 4.3 Flow Chart of Methodology 49
Figure 4.4 Image Processing 52
Figure 4.5 Creation of Spatiotemporal Plots 53
Figure 4.6 Flow Profile Analysis at the Atrial Inlet 57
Figure 4.7 ST Plot Analysis with Radon Transforms 61
Figure 4.8 Perpendicular ST Plots for Diameter Measurement 64
Figure 4.9 Automated Heart Rate Determination 67
Figure 4.10 Results of Demo Experiment (Velocity and Diameter) 69
Figure 4.11. Results of Demo Experiment (Flow Rate and Accumulated Volume) 70

Figure 4.12 Bin Size Optimization 76
Figure 4.13 Averaging Span Optimization 78
Figure 4.14 Reference Line Orientation Error 79
Figure 4.15 Streak Angle Error 81
Figure 4.16 Creation of Radon Transforms (another example) 83
Figure 4.17 Radon Analysis Comparisons 84
Figure 4.18 Synthetic Data Specification 86
Figure 4.19 Synthetic Data and Corresponding ST Plot 87
Figure 4.20 Analysis Plots Associated with Synthetic Data 88
Figure 5.1 Blood Cell and Wall Tracking 92
Figure 5.2 Describing Wall Mechanics with ST Plots 94
Figure 5.3 Wave Propagation through the Heart 95
Figure 5.4 Contraction Wave Timing 96
Figure 5.5 Relative Blood Velocity at 30 and 48 hpf 98
Figure 5.6 Changes in Cardiac Biomechanics 102
Figure 5.7 Looping Angle and Lumen Ratio Measurement 108
Figure 5.8 Raw Data for All 48 hpf Samples 109
Figure 5.9 Raw Data for All 55 hpf Samples 110
Figure 5.10 Box Plots of Parameters at 48 and 55 hpf 111
Figure 5.11 Stroke Volume vs. Square of Inlet Diameter 112
Figure 6.1 Blood Pooling Resulting from Centrifugation 116
Figure 6.2 Rotation Experiment Setup 117
Figure 6.3 Overview of Study Timing 118
Figure 6.4 Representative Hearts at the end of Atrial Diastole 120
Figure 6.5 Representative Hearts at the end of Atrial Systole 120
Figure 6.6 Low Performing Hearts at the end of Atrial Diastole 121
Figure 6.7 Low Performing Hearts at the end of Atrial Systole 121
Figure 6.8 Box Plots of Looping Angle and Lumen Ratio 122
Figure 6.9 Box Plots of Stroke Volume and Regurgitant Fraction 124

CHAPTER 1: HYPOTHESIS AND AIMS

1.1 Chapter Introduction

Despite the prevalence of congenital heart defects (CHDs), the exact cause is unknown in the large majority of patients. Over a decade of intensive research on CHDs has led to the theory that epigenetic factors may play an important role in heart development. The developing heart is especially susceptible to mechanical influences because it begins to contract and circulate blood long before it has reached its final configuration. It is thus exposed to cyclical changes in pressure, endocardial cell strain, and wall shear stress throughout early development. It has been shown that when these stresses are altered, the heart does not develop normally, and many types of CHDs can result.

A topic that has not been well-studied is the effect of timing. When do altered stresses have an impact on heart development? Is there a period of time when the heart is more susceptible to developing defects than others? **The specific hypothesis of this dissertation is that significant decreases in heart function persist when cardiac loading is altered during certain time windows of early development.** Because a commonly observed effect of altered loading in previous studies is impaired cardiac looping, and because the general morphology of the heart has a tremendous impact on the blood flow dynamics, I expect that the key time windows will be near the beginning of cardiac looping. In order to address the hypothesis, this project was divided into three aims.

1.2 Aim 1

The zebrafish is an important model for development research due in part to its exceptional optical access which provides outstanding opportunities for *in vivo* observations. As of the start of this project, there were limited quantitative techniques for accurately measuring heart function and related parameters in the zebrafish model. In order to understand the variables involved in the creation of CHDs, it is important that quantitative measurements be used.

Building upon techniques used from previous studies, Aim 1 was to develop a methodology for quantifying heart function in the zebrafish embryo. Methods were optimized and validated to ensure effective application to the zebrafish model. The methodology was developed around the use of a high-speed CCD camera with a bright field stereomicroscope. The main parameters to be measured were the blood velocity vs. time, heart lumen diameter vs. time, blood flow rate vs. time, stroke volume, heart rate, cardiac output, and retrograde fraction. These values provide a simple yet quantitative means for examining not only the overall heart function, but also the changing flow dynamics throughout the course of the cardiac cycle.

1.3 Aim 2

The zebrafish embryonic heart begins to beat at approximately 24 hours post-fertilization (hpf), and circulation follows soon afterward at 26-30 hpf. The heart transforms from a simple tube structure to a looped configuration resembling an adult

heart from approximately 36 to 48 hpf. This transition radically changes the stresses on the heart, and considering the evidence pointing to mechanical stress as an important epigenetic variable, this is potentially a very influential stage on the development of CHDs. Many studies have investigated pumping mechanics at the tube stage but very few have examined the mechanics as the heart loops and forms chambers. **The first part of Aim 2 was to closely observe the pumping mechanics throughout the major stages of heart development.** These observations helped in defining the treatment groups in Aim 3.

Given the lack of extensive quantitative data on heart function in the embryonic zebrafish, it was necessary to benchmark normal function. **The second part of Aim 2 was to benchmark heart function in wild-type zebrafish embryos using the methodology developed in Aim 1.** Two time points were chosen for analysis: 48 hpf and 55 hpf. 48 hpf marks the completion of cardiac looping and is the first time point in which treatments from Aim 3 will be complete. 55 hpf is one of the last points before natural pigmentation within the embryo begins to obscure the view of the heart. This data was crucial for making comparisons with treatment groups from Aim 3.

1.4 Aim 3

Most previous studies on the effect of altered hemodynamics on heart development involved invasive and irreversible surgical procedures to alter blood flow to the heart. As a result, there has been a lack of research on the effect of timing of altered

hemodynamics. **Aim 3 was to manipulate cardiac loading in the zebrafish embryo so that the effect of timing can be assessed.** A pilot study was performed in which blood flow was non-invasively manipulated during four different time windows in early development. Cardiac function was assessed at each time point and compared to the baseline values measured in Aim 2.

1.5 Overview of Results

In Aim 1, a methodology was successfully created in which flow rate, stroke volume, regurgitant fraction, and other key parameters can be estimated from 2D high-speed image sequences of the zebrafish heart. This methodology was implemented in Aim 2 and all parameters were benchmarked for 48 hpf and 55 hpf embryos. Low-speed centrifugation was used as a new model for altering cardiac loading in the zebrafish embryo. This resulted in impaired cardiac looping and significantly reduced heart function. These effects were more pronounced when treatment was applied at earlier time windows. Treatments applied at later time windows had immediate effects which mostly dissipated after ~7 hours. Results support the hypothesis that timing of altered loading plays a role in heart development, and that altered loading at earlier time points results in changes in heart morphology and decreases in heart function.

1.6 Dissertation Organization

This dissertation is broken into several chapters. Chapter 2 is a literature review which discusses important topics related to research on heart development, epigenetics, imaging, and measurement of heart function. Chapter 3 discusses methods used throughout the project which are common to all Aims. Chapter 4 is devoted to Aim 1 and discusses the development of the methodology for quantifying heart function, including less successful techniques which were attempted. This chapter includes data on optimization and validation of the methods used. Chapter 5 is devoted to Aim 2 and discusses the changing pumping mechanics in the developing heart as well as quantitative benchmarks for heart function at 48 and 55 hpf. Chapter 6 covers Aim 3 in which a new technique for altering cardiac loading is presented. Results of altered loading are discussed and the central hypothesis is addressed. Chapter 7 discusses possible future research directions related to this research. Chapter 8 lists my original contributions to the field, including publications and conference material. Chapter 9 is a summary of the findings.

CHAPTER 2: LITERATURE REVIEW

2.1 Congenital Heart Defect Statistics

Congenital heart defects (CHDs) are a relatively common problem, with an occurrence of approximately 8 cases in every 1000 live births [1]. Some of the more common defects include atrial and ventricular septal defects, malformed or stenotic valves, and abnormalities of the great arteries. About 8-10% of CHD cases can be attributed to chromosomal abnormalities [2]. Examples include Down syndrome (trisomy 21) and Edwards syndrome (trisomy 18), where patients are afflicted with CHDs in 40-50% and over 90% of cases respectively [3]. Maternal illness and teratogens have also been linked to CHDs and account for approximately 5% of instances [2]. Maternal diabetes can increase the occurrence of CHDs by a factor of 5, and exposure to retinoic acid can increase occurrence by a factor of 25 [2]. Gene mutations can also cause congenital heart defects. Holt-Oram syndrome is a condition caused by a mutation in the Tbx5 gene and results in congenital defects and limb malformations [4]. Only 3-5% of CHDs are known to be attributed to single-gene defects [2]. This leaves a remarkable 80% of CHDs with an unknown origin.

2.2 Epigenetics

The fundamental cause of most cardiac defects is almost certainly abnormal gene expression; gene expression directs cellular behavior and is the overarching force that governs development. Gene expression is not simply determined by which genes are

present in the cell because all cells have the same genes. It is instead governed by a highly complex process that relies on contributions from many variables both within the cell and its environment [5]. This concept of outside influences determining gene expression is termed epigenetics. Mechanical stresses are thought to be an important epigenetic factor in heart development [6-8], and a large amount of research is being conducted to pinpoint the variables involved in this process.

2.3 Animal Models in Heart Development Research

Several models have been used to study heart development, from the mouse [9] to the fruit fly [10]. Although mammalian models such as the mouse are more closely related to humans, *in utero* development makes it exceedingly difficult to observe embryos *in vivo* and typically requires the sacrifice of the mother [11] to gain access. Once removed from the uterus, a mouse embryo can only survive for about two days [12]. This makes extended *in vivo* studies on the same embryo problematic. Imaging of the mouse heart is limited due to the opacity of mammalian tissue. The structure of the heart can be observed using ultrasound [9], but blood-flow based measurements have much lower spatial and/or temporal resolution than imaging modalities available to other models.

The majority of studies investigating epigenetic variables on heart development use either the embryonic chick or the embryonic zebrafish as a model. The major benefit of these models over mammalian models is their external development, which allows for drastically easier *in vivo* observations. Like mammals, the adult chicken heart undergoes the same series of developmental stages to arrive at a four chambered adult

heart [13]. A portion of the egg and underlying membrane can be removed to allow optical access to the embryo within [14]. Inks or dyes can be injected into the circulation of the translucent chick embryo in order to visualize large-scale blood flow patterns [15]. Multiple imaging modalities can be used to observe cardiac function in the chick model. One particularly prevalent and useful option in use today is 4D optical coherence tomography (OCT). OCT is quite powerful for measuring the 3D heart structure but is not particularly good for blood flow measurements. Blood flow is generally estimated by using computational fluid dynamics (CFD). In this case, heart wall spatial measurements and servo-null pressure measurements are used to define boundary conditions [16, 17].

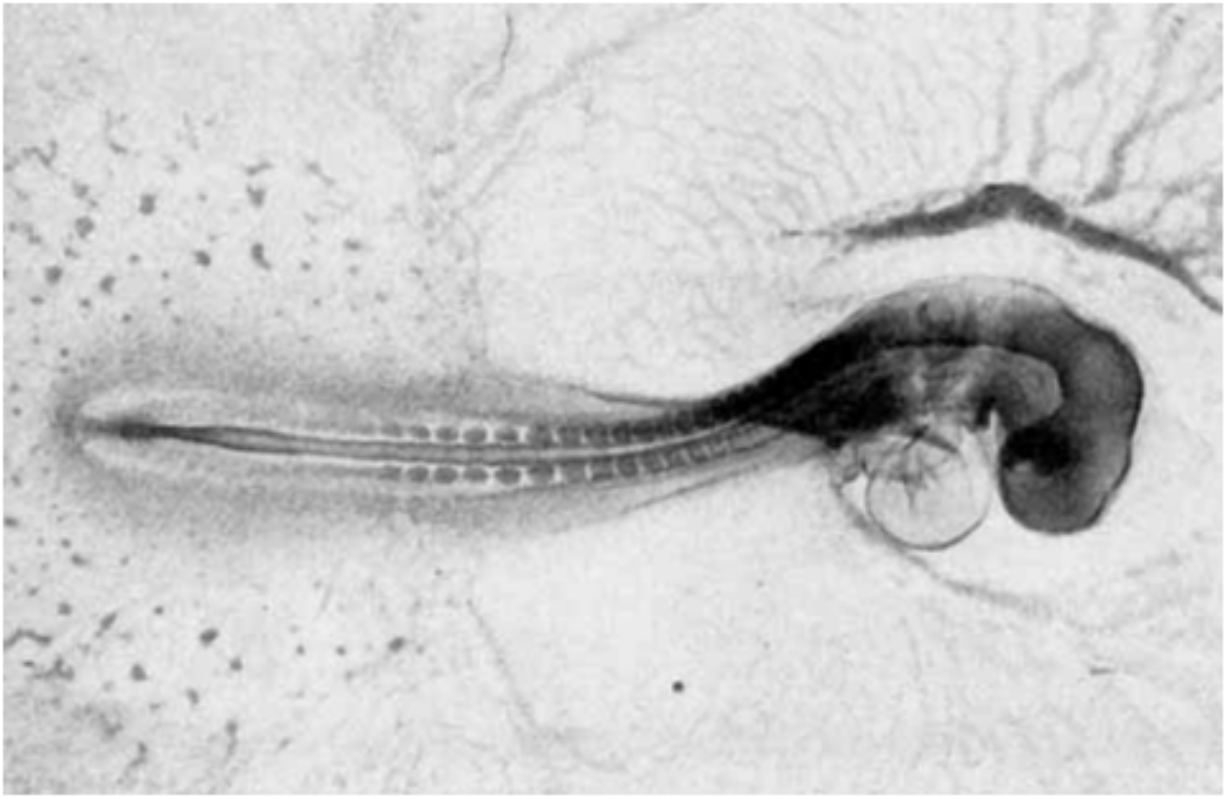

Figure 2.1 Chick embryo
Chick embryo at stage HH14 (late cardiac looping). Image taken from Hamburger and Hamilton, 1951 [18].

The adult zebrafish heart has only two chambers and is therefore quite different than the adult human heart. However, a critical point to note is that the beginning stages of all vertebrate hearts are very similar [19-21]. This makes the zebrafish model relevant for understanding the early stages of heart development [22]. The zebrafish has a strong advantage over the chick in that it develops within a transparent chorion which can safely and easily be removed by the time heart development begins. More importantly, the actual tissue of the zebrafish embryo is transparent. This makes it possible to observe the beating heart and circulating blood cells with standard bright field microscopy (Figure 2.2).

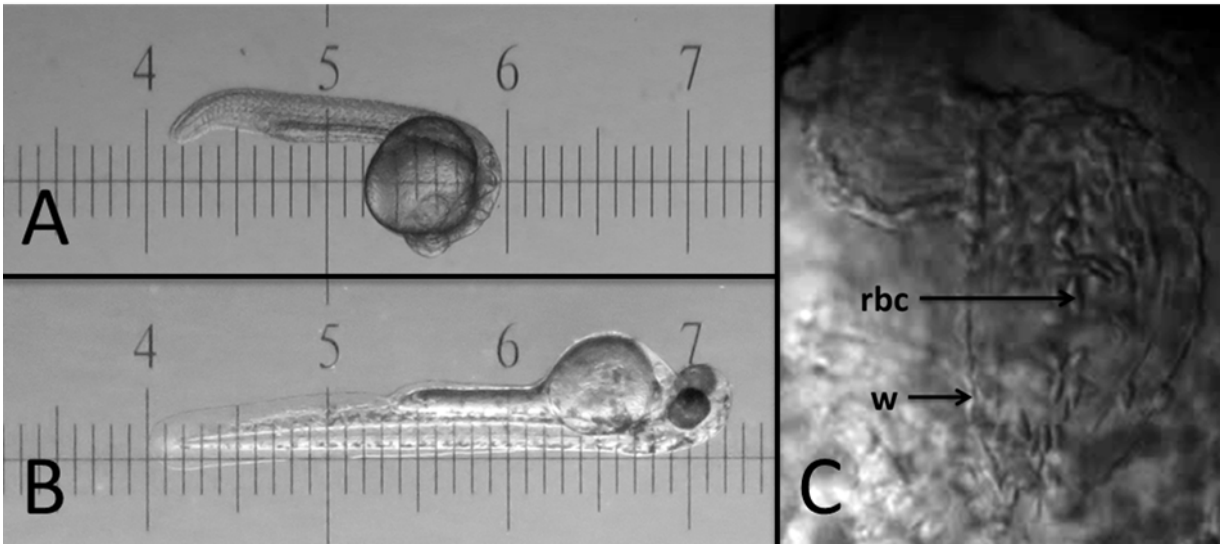

Figure 2.2 Zebrafish embryo scale and transparency
A 24 hpf zebrafish embryo (A) and a 72 hpf embryo (B) on a calibration slide for scale. Units are in millimeters. Note that slide markings are visible through the embryo's transparent tissues. Blood cells (rbc) and the heart wall boundary (w) can easily be observed in vivo using bright field microscopy (C).

The zebrafish model boasts further advantages in that there are literally thousands of different transgenic lines, mutant lines, and morpholinos to work with [23, 24]. This includes transgenic lines with fluorescent blood cells and heart tissue [25, 26] and

mutant lines that express heart defects [5, 27, 28]. Multiple heart-related genes have been discovered which have similar roles in humans [29-32] which further backs up the relevance of the zebrafish model to human heart development. The zebrafish develops quickly, growing from a fertilized egg to an embryo with completed cardiac looping in approximately 48 hours. Oxygen can easily penetrate the tiny zebrafish embryo through passive diffusion, so the zebrafish can survive for several days without any heart function [19]. This makes it possible to study severe cardiac phenotypes well beyond the point at which mammalian models would have died. Finally, the zebrafish produces dozens to hundreds of eggs per clutch and is relatively inexpensive to maintain. A zebrafish handling facility is located at Colorado State University.

2.4 Early Heart Development in the Zebrafish

The heart is one of the first organs to develop [33]. In all vertebrates, the key developmental stages and genes related to heart development are conserved [19, 34]. So although this description is geared toward zebrafish embryos, it is applicable to all vertebrates. The early embryo contains three germ layers: the ectoderm, mesoderm, and endoderm [21]. The heart arises from two fields of pre-cardiac cells in the mesoderm which migrate toward the midline as two cardiogenic plates [35]. By 20 hpf, these plates form two tubes which lie on either side of a group of endocardial progenitor cells [20] (Figure 2.3A). Over the next four hours of development, these tubes fuse around the endocardial progenitor cells and create a single definitive heart tube [20, 22] (Figure 2.3 B-D). This heart tube is made up of a single outer layer of myocardial cells, a single inner layer of endothelial cells, and an intermediate layer of extracellular matrix

called cardiac jelly [13]. Individual cardiomyocytes begin contracting even before the heart tube is finished fusing [20].

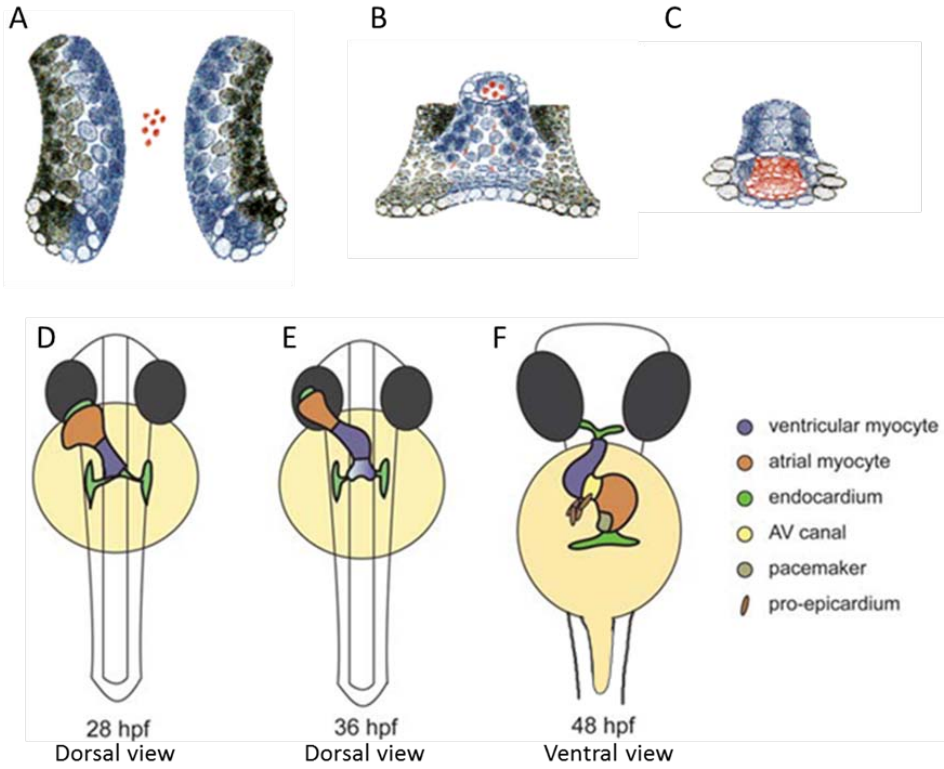

Figure 2.3 Key stages of zebrafish heart development
Tubular primordia migrate toward midline (A) where they fuse around endocardial progenitor cells (B) to form a single heart tube (C). The heart tube (D) loops over the next several hours (E) until reaching a near-adult configuration by 48 hpf (F). Note (D) and (E) are dorsal views and (F) is a ventral view. Adapted from Stainier et al., 1993 [20] (A-C) and Bakkers, 2011 [36] (D-F).

Shortly after the heart tube is formed, contractions become coordinated and circulation begins [20]. The early atrium and ventricle can be distinguished as ballooned regions divided by the atrioventricular canal by 33 hpf [37]. The tube begins to loop toward the right (with respect to the embryo) by 36 hpf (Figure 2.3E), and looping is completed by 48 hpf [36] (Figure 2.3F). Blood circulation at this stage is largely unidirectional despite the fact that valves have not formed [37]. It should be noted that the literature is

inconsistent on exactly when looping occurs and is complete; some articles have claimed that looping takes place between 30 and 36 hpf [20, 29]. Based on my personal experience, looping blatantly continues through 48 hours and the overall heart structure continues to change slightly through 72 hpf. An example of the type continued morphological changes that occur beyond 48 hpf is illustrated in Figure 2.4. Endocardial cushions form by 48 hpf, and fully functional valves take their place by 105-111 hpf [36, 37]. The stages of heart development in the zebrafish are remarkably similar to humans through around 48 hpf. After this equivalent point in development, the human heart develops a much more complicated configuration in which endocardial cushions are transformed into septa and valves which divide the heart into four chambers [13].

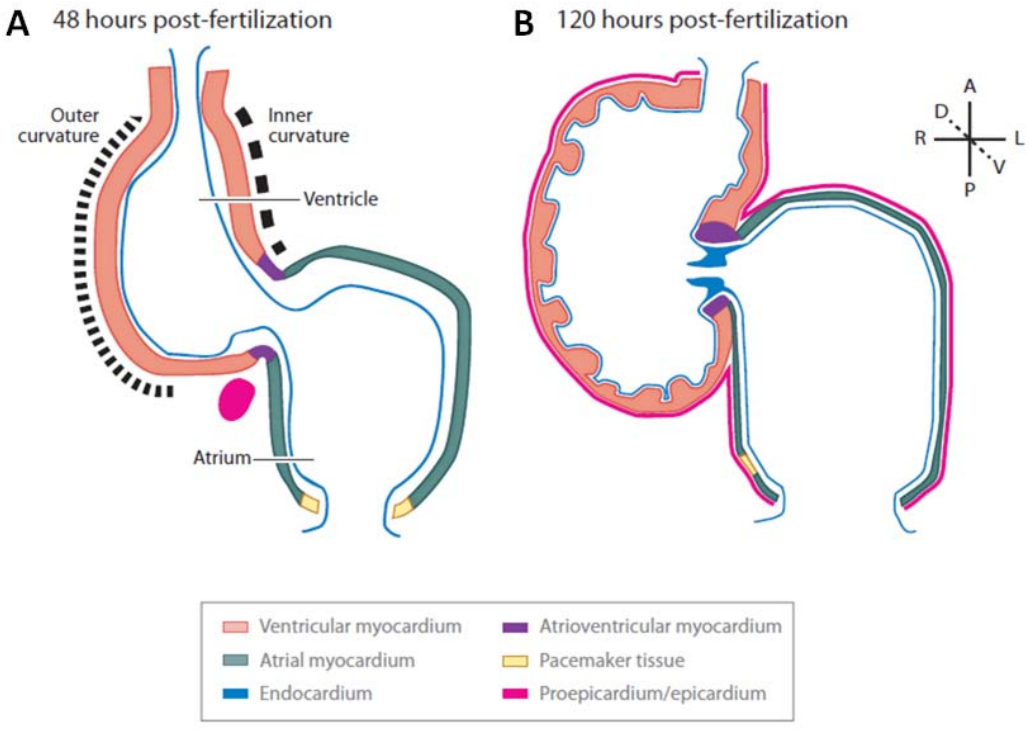

Figure 2.4 Zebrafish Heart Morphology at 48 and 120 hpf
Although many articles agree that cardiac looping is completed between 36 and 48 hpf, the general shape continues to change beyond 48 hpf. A zebrafish heart is illustrated at 48 (A) hpf and 120 hpf (B). Image taken from Staudt and Stainier, 2012 [38].

2.5 Pumping Mechanics of the Embryonic Heart

One might think that something as fundamental as pumping mechanics in the embryonic heart would be well understood. However, the exact pumping mechanics of the embryonic heart tube are still under debate [39]. From the late 1800s through the early 2000s, the embryonic heart tube was thought to function as a simple peristaltic pump [39]. Peristalsis is seen in multiple pumping systems in the body, most notably in the digestive system. In a peristaltic pump, active contraction waves travel down the length of a flexible tube and effectively push fluid forward [40]. In a "technical peristaltic pump", this unidirectional contraction wave moves with a continuous velocity (equivalent to the fluid), and pump output increases linearly with wave frequency [39, 41]. It has been shown that the embryonic heart tube does not exhibit these properties, because blood velocity can be faster than wave speed and cardiac output does not necessarily vary linearly with heart rate [41]. The heart tube has since been presented to function as an impedance pump [41] (also known as a Liebaugh pump or suction pump).

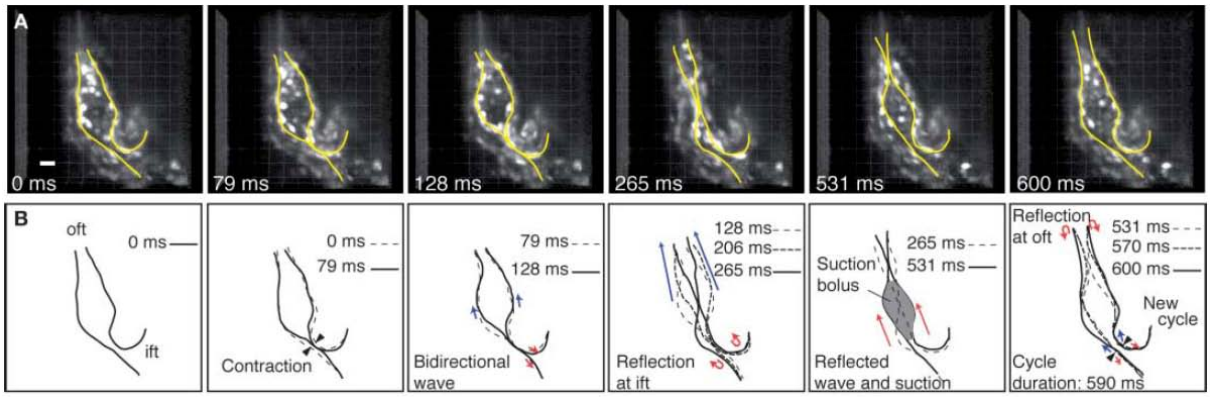

Figure 2.5 Proposed impedance pump wave mechanics
Some evidence suggests that the embryonic heart tube works like an impedance pump, as shown here in a figure taken from Forouhar et al., 2006 [41]. Fluorescence images in (A) show several frames at various points in the cardiac cycle while (B) describes how passive waves may combine to produce an impedance pumping mechanism. ift = inflow tract, oft = outflow tract.

An impedance pump works through the temporary constriction of a single point in a flexible tube which sends a primary wave along the tube in both directions. If the tube has sections with different mechanical impedances, and the constriction point is asymmetrically located within the tube, then the primary wave will be reflected off the impedance boundary. These reflected waves can combine to create a (still passive) wave that pushes fluid in a single direction [41, 42]. Impedance pumps are able to generate flow that is faster than the initial contraction wave, and their output varies nonlinearly with wave frequency [42, 43]. This may explain the flow characteristics seen in the embryonic heart tube. The case is far from closed, however, because there are confounding properties of impedance pumps that do not seem to support the theory. Some studies indicate that the flow in an impedance pump typically moves from the long passive tube region toward the short passive region [39], which is opposite to that seen in the heart tube. It should also be noted that impedance pumps are far more effective when operating near their resonance frequency, and resonance frequencies found from previous studies tend to be notably higher than the 2 Hz seen in the heart tube [42-44]. These discrepancies could be explained by the complex conditions of the embryonic heart tube, which is not simply a single-layer compliant tube in air, but is instead a three-layered tube within the embryo. Computer modeling showed that multilayer impedance pumps are more sensitive to stimulation [44] and therefore may exhibit altered flow behavior given the particular conditions in the embryo. Recent calcium signaling evidence suggests that the contraction wave in the heart tube is in fact active [45]. This speaks against the passive nature of the propagating waves in impedance pumps. The search for the true mechanism(s) is ongoing, but the most likely

explanation seems to be that the embryonic heart tube functions neither as a technical peristaltic pump nor as a technical impedance pump, but perhaps has a combined mechanism of active propagating waves aided by passive reflecting waves [39].

The pumping mechanics of the heart at later stages is less of a mystery. As the heart tube begins to loop, it quickly forms distinct chambers. Constrictions exist at the atrial inlet, the atrioventricular (AV) canal, and the ventricular outlet. No actual valve leaflets are present throughout the looping process, but the coordinated motion of the heart and constriction of these areas helps keep flow moving in mainly the positive direction [46]. During early looping, this motion consists of a prominent active contraction wave that proceeds from the atrial inlet through the ventricular outlet. This wave becomes less continuous throughout the looping stage, and eventually the atrial and ventricular waves appear to be independent [46]. By this stage, endocardial cushions have formed at the constriction sites and are able to prevent most of the backflow that would otherwise result from independent chamber contraction [37]. Finally the endocardial cushions are replaced with functional valves containing leaflets which prevent nearly all backflow. Throughout much of the post-tube stage and into adulthood, the heart works as a classic displacement pump; blood is trapped within one chamber, the chamber is contracted, and blood is forced forward through a one-way valve while being prevented from going backward through another one-way valve.

2.6 Mechanical Stress and Fluid Dynamics in the Embryonic Heart

The cells of the heart are exposed to a variety of forces and stresses. As myocardial cells contract, hoop stress—a mechanical stress that acts circumferentially within the heart wall—is generated. This hoop stress opposes the pressure that builds within the heart as a result of the contraction (Figure 2.6). The pressure and hoop stress are directly related as:

$$p = \frac{\sigma_h t}{R} \quad <--> \quad \sigma_h = \frac{pR}{t}$$

Where p is the interior blood pressure (the intramural pressure), R is the heart radius, and t is the wall thickness [8]. Longitudinal stress is also created at approximately half of the magnitude of the hoop stress [8].

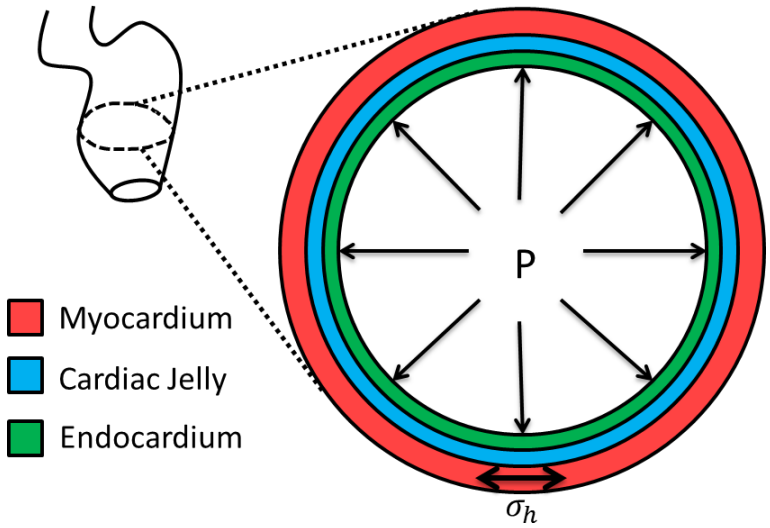

Figure 2.6 Hoop Stress and Pressure within the Heart
Internal pressure, P, within the heart is opposed by hoop stress, σ_h. Hoop stress may be distributed across all layers but the myocardium likely bears the vast majority of the load.

Myocardial cells generate internal forces which work to shorten the cell length. Meanwhile intercellular tension, which works to pull cells apart, builds as pressure and

hoop stress rise. Endocardial cells passively line the heart lumen, but they are squeezed radially between the contracting myocardium (and cardiac jelly) and the pressurized blood within the heart. The amount of compression felt by the endocardium depends on the stage of the cardiac cycle; maximum compression occurs during systole and minimum compression occurs during diastole. It is difficult to know how forces act upon the endocardium in the circumferential direction. Because endocardial cells passively line the heart lumen, they may be stretched or compressed depending on the stage of cardiac cycle and their exact position within the heart.

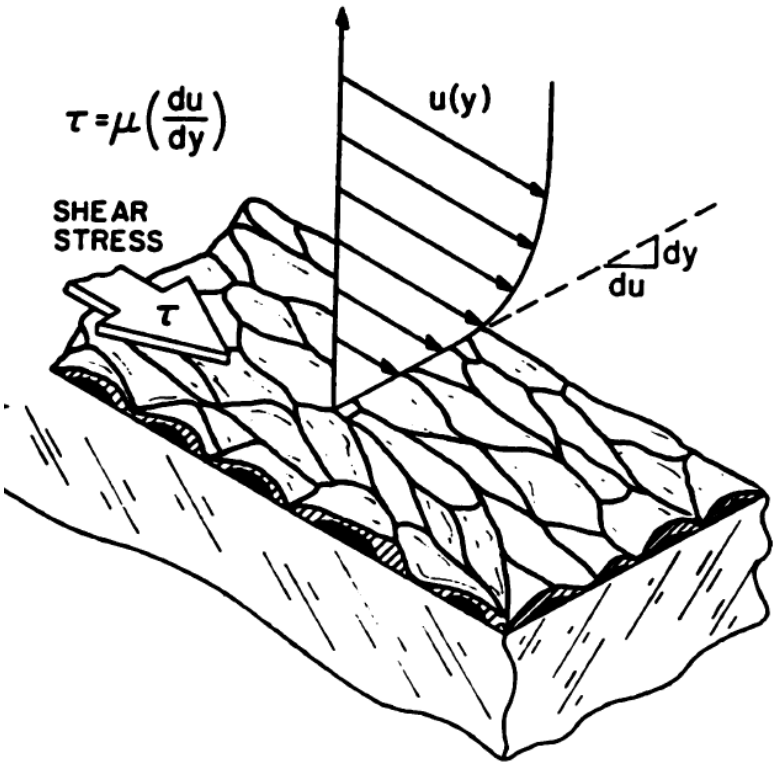

Figure 2.7 Shear Stress along the Heart Wall
As blood flows through the heart, shear stress is exerted along the endocardium. Shear stress is a function of blood viscosity and velocity and appears to play an important role in valve formation. This figure was taken from Davies et al., 1984 [47].

As blood is pumped through the heart, it imparts shear stress along the wall (Figure 2.7). Wall shear stress in the embryonic heart can be defined as:

$$\tau_w = -\frac{2\mu u_{max}}{R} = \frac{R}{2\mu}\frac{dp}{dx} = -\frac{32\mu Q}{\pi D^3}$$

Where μ is the blood viscosity, u_{max} is the maximum blood velocity, R is the heart radius, dp/dx is the change in pressure per unit length, Q is the flow rate, and D is the heart diameter [8]. The negative signs in the first and third forms of the equation are due to the fact that shear stress acts in opposition to the flow direction. Wall shear stress can be thought of as the frictional stress along the wall as a result of blood flow. The equations reflect that shear stress magnitude increases dramatically as cross-sectional area decreases. This means that constricted regions, such as the atrial inlet and atrioventricular canal, are exposed to much higher wall shear stresses than wider sections of the heart which have essentially the same flow rates and blood viscosity. It is in these constricted regions that future valves will form, and it is suspected that shear stress is an important signal for valve formation [48].

The Reynolds and Womersley numbers can be used to describe the overall blood flow conditions within the heart. The Reynolds number is defined as

$$Re = \frac{\rho U L}{\mu}$$

where ρ is the fluid density, U is the characteristic velocity, L is the characteristic length scale, and μ is the fluid viscosity. In the case of the embryonic heart, U and L can be defined as the peak velocity and the heart lumen diameter respectively [8]. The Reynolds number is the ratio of inertial and viscous forces [8]. Reynolds numbers above ~1000-2000 are dominated by inertia, while Reynolds numbers below one are dominated by viscous forces. The Womersley number is defined as

$$Wo = L\sqrt{\frac{\omega\rho}{\mu}}$$

where ω is the frequency (in this case pulse rate) [8]. The Womersley number gives an indication of the stability of the flow profile; a low Womersley number below one indicates that the flow profile will be nearly parabolic throughout the cycle. Higher values lead to increasing profile irregularities due to the effects from the previous cycle. In the embryonic zebrafish heart, the Reynolds and Womersley numbers remain well below one. This indicates that the flow is dominated by viscous forces with negligible cyclic effects on the parabolic nature of the flow profile [8].

The viscosity of a fluid plays a tremendous role in how it behaves; consider the difference between water and toothpaste. Viscosity is a measure of a fluid's internal attractive forces, which on a macro-scale can be considered its resistance to flow. Thus lower viscosity fluids flow more easily. When a fluid's viscosity remains constant under varying amounts of shear, it is considered a Newtonian fluid. Water, oils, and air are all Newtonian fluids. Most fluid models and simplified equations assume that a fluid is Newtonian. Calculation of fluid dynamics is drastically more complicated when a fluid does not behave in a Newtonian manner. Blood is technically a non-Newtonian fluid but the degree to which it varies from a Newtonian fluid is based strongly upon hematocrit, fibrinogen levels, and the shear rate (Figure 2.8) [49]. Hematocrit is the percentage of blood made up of red blood cells. In the embryo, hematocrit is around 10-15%. This is very low compared to the 35-50% seen in an adult [8]. The genes responsible for the creation of fibrinogen are expressed in the liver by the time blood flow begins [50]. Few

if any studies have measured the fibrinogen concentration within the embryonic zebrafish throughout early development, but it is doubtful that fibrinogen is present at levels exceeding those of an adult. A more important point than the actual fibrinogen concentration is that fibrinogen's non-Newtonian effects are due to temporarily binding blood cells together to form aggregates. With such a low hematocrit, fibrinogen has less opportunity to bind cells together. Shear rate is the rate of deformation of a fluid flow under a given amount of shear (the velocity of a fluid at a given height divided by the height). As shown in Figure 2.8, microcirculation flows are within the range of shear rates where non-Newtonian properties may exist. The embryonic heart falls in this category. However, when considering all three major variables, non-Newtonian effects may be small or even negligible.

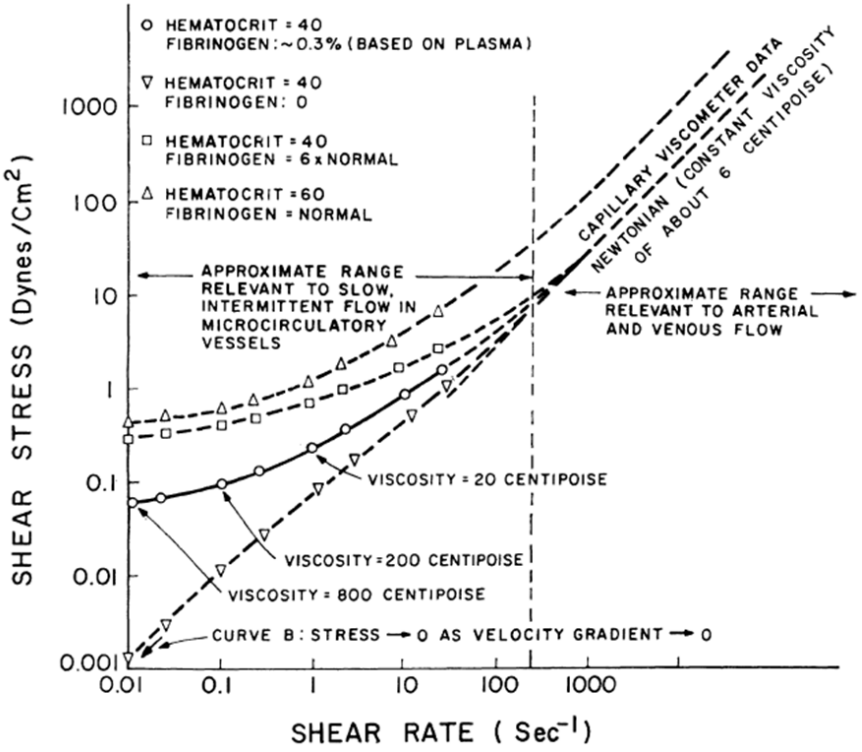

Figure 2.8 Plot of Shear Stress vs. Shear Rate for Blood
Newtonian fluids have constant viscosity and create a straight line and intersect the origin. Depending on the conditions, blood may vary notably from a Newtonian fluid. Figure from Replogle et al., 1967 [49]

2.7 Cellular Response to Mechanical Stress

The heart pumps blood long before it completes development. This exposes the endocardium to cyclical shear stress from blood flowing tangentially to the heart wall as well as cyclical changes in circumferential stress and pressure as the heart contracts and expands. These stresses are sensed by cells [51] and are believed to play a major role in development [8].

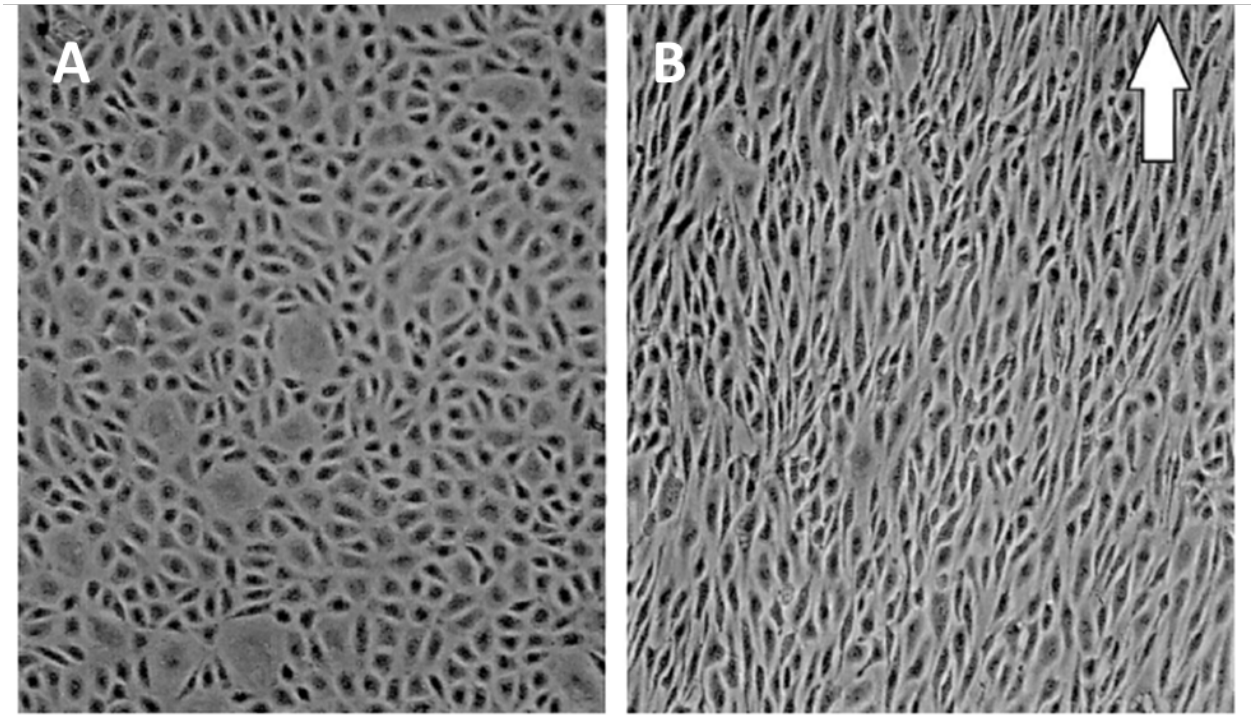

Figure 2.9 Endothelial Cell Alignment with Flow In Vitro
Cultured endothelial cells in static conditions (A) have a near-random arrangement. Under a steady flow at 10 dyn/cm^2 (B), cells become elongated and orient themselves in the flow direction (white arrow). Figure taken from Topper and Gimbrone, 1999 [52].

Endothelial cells are highly responsive to shear stress [47, 53-57]. When *in vitro* endothelial cells are exposed to uniform shear stress in the range of 5-10 dynes/cm^2, they become elongated and align themselves in the direction of the flow [54] (Figure

2.9). This involves a substantial change in the cytoskeletal arrangement [52, 55]. Cells respond not only to the magnitude of the shear stress applied but also to the flow pattern; non-reversing sinusoidal, reversing sinusoidal, and oscillatory flows have been shown to each result in a different cellular phenotype in vascular endothelial cells [55]. Additionally, turbulent flow results in significantly different phenotypes than laminar flows, even in cases when the turbulent flow remains at a lower shear stress [53]. Cells in high-shear regions of the developing chicken heart have also been shown to align with flow. Flow alterations at the inflow tract result not only in changes in endocardial cell alignment, but also in abnormal heart morphology [14]. This confirms that the traits witnessed in *in vitro* studies translate to the developing heart.

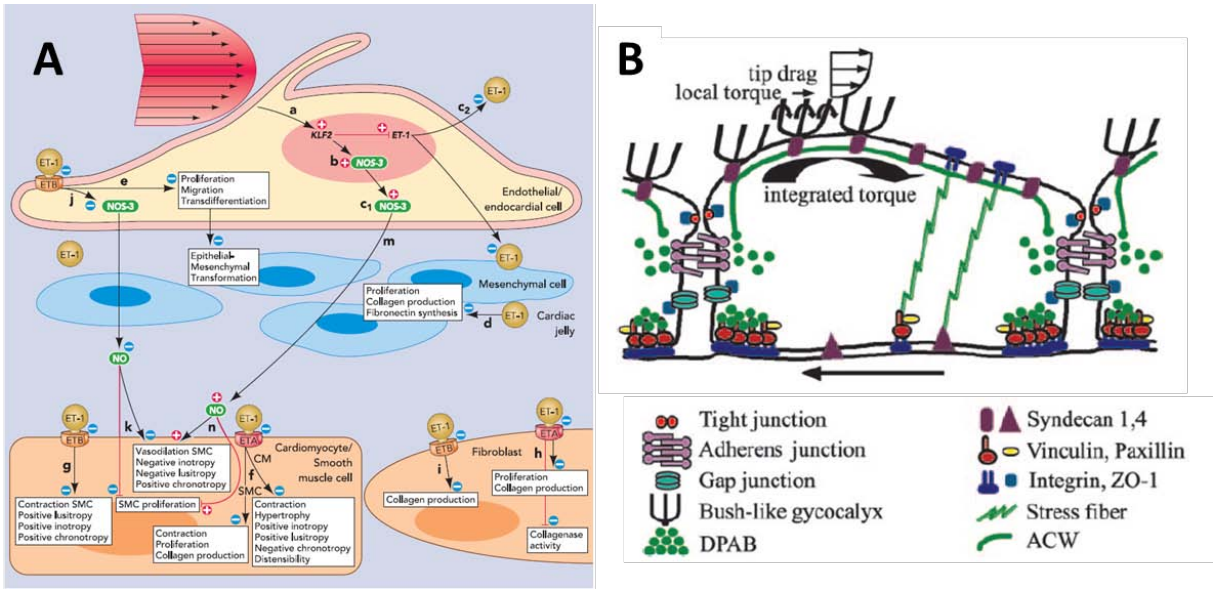

Figure 2.10 Cellular Response to Shear Stress
Signaling cascades can result from shear stress acting on ciliated endothelial cell (A). Figure taken from Groenendijk et al., 2007 [13]. Cells can also sense shear through deformation of the glycocalyx (B). Figure adapted from Thi et al., 2004 [58].

Several mechanisms exist which give cells the ability to sense the mechanics of their surroundings [52, 58]. Some endothelial cells have cilia which bend under shear stress

and alter calcium channel activity which may influence the cytoskeletal arrangement [13] (Figure 2.10A). Aside from cilia, the primary structure suspected of sensing shear stress is the glycocalyx, a framework of proteins that are attached to the external surface of endothelial cells [8]. As blood flows across the cell, shear stress deforms the glycocalyx and can initiate cell signaling cascades [58] (Figure 2.10B). Mechanical stretch on endothelial cells can physically alter the configuration of ion channels, ion pumps, cell junctions, and various surface receptors (Figure 2.11). These changes can lead to signaling cascades which can activate an array of kinases which proceed to alter gene expression and ultimately cell function [59]. Although the details are beyond the scope of this research, this is the essence of the idea of epigenetics and is the likely force behind many congenital heart defects.

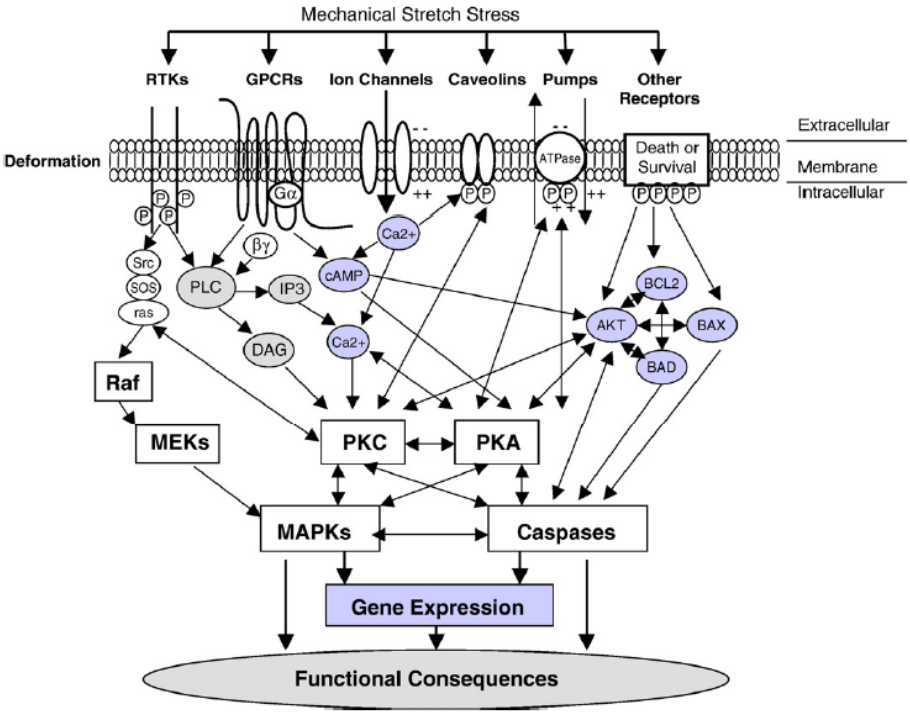

Figure 2.11 Signaling Cascades Resulting from Mechanical Stretch on Cell
Mechanical stretch can activate a variety of cell surface proteins which are involved in signaling. This can lead to changes in gene expression and cell function. Figure taken from Li and Xu, 2007 [59].

2.8 Effect of Blood Flow on Heart Development

After considering the previous points regarding mechanical stress within the developing heart and the ability for endothelial cells to both sense and respond to such stresses, it should not be surprising that abnormal blood flow during development can result in severe morphological defects. Much research has been devoted to examining the effects of altered blood flow on heart development, mostly using the embryonic chick and zebrafish models.

Several investigators performed experiments by ligating different branches of chick vitelline veins. The vitelline veins are the final veins in the circulation before blood is returned to the heart. Ligating (closing off) these veins causes changes in cardiac blood flow patterns without affecting overall blood volume. It also decreases cardiac loading because blood is slower to fill the heart [60]. This procedure has been shown to result in an array of heart defects including ventricular septum defects, valve abnormalities, impaired cardiac looping, and great vessel malformations (Figure 2.12) [15, 61, 62]. Ligation of each of the three major branches of the vitelline veins resulted in similar heart defects [15].

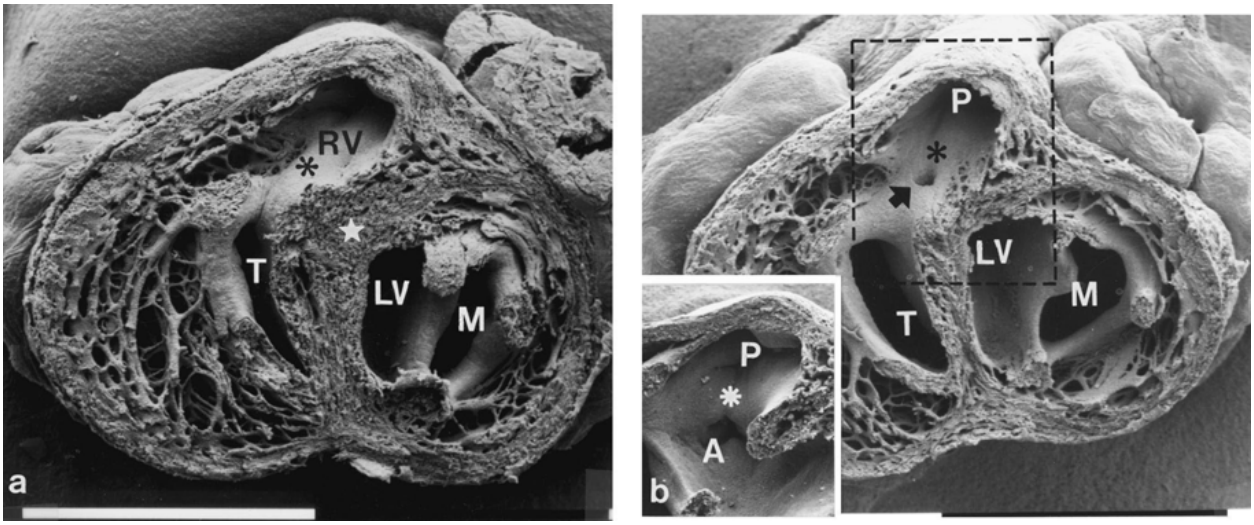

Figure 2.12 Septum Defect Resulting from Vitelline Vein Ligation
Part (a) shows a normal chick heart under scanning electron microscopy after cutting it transversely. Part (b) shows the heart of a chick after vitelline vein ligation. The asterisk marks the location of a ventricular septal defect. Abbreviations: A = aorta, LV = left ventricular outflow tract, M = mitral valve, P = pulmonary artery, RV = right ventricular outflow tract, T = tricuspid valve. Bar = 1 mm. Figure taken from Hogers et al., 1999 [15].

Left atrial ligation (LAL) is another common technique used to disrupt normal blood flow in the chick embryo. LAL is performed by tying a suture around the developing atrium such that flow is partially occluded. As in vitelline vein ligation, the heart fills more slowly and cardiac preload is decreased [63]. A complementary procedure—conotruncal banding (CTB)—can be performed to produce the opposite effect. The conotruncus lies just downstream of the ventricle at the outflow tract of the chick heart. Partial occlusion via banding results in increased cardiac loading since the heart must force blood through a smaller opening. Increased loading via CTB can cause premature development of the cardiac conduction system in the chick [63], while decreased cardiac loading via LAL can delay the development of the cardiac conduction system. Interestingly, a similar result was found in the myocardial architecture of the heart; CTB

resulted in early maturation of the myofiber angle in the left ventricle, while LAL resulted in significantly delayed myofiber angle maturation [64].

Altered loading has also been shown to result in changes in the mechanical properties of the heart tissue; after LAL, chick myocardium becomes stiffer as a result of increased microtubule density [60]. Lastly, direct external forces on the heart have been shown to play a role in development. The splanchnopleure is a membrane that pushes against the heart in the developing chick. Removal of the splanchnopleure results in delayed cardiac looping [65-68] although hearts appear to return to their normal configuration after a time.

Like the chick embryonic heart, the zebrafish embryonic heart is highly responsive to changes in blood flow and cardiac loading. Hove et al. studied the effect of altered loading and shear stress on heart development by performing a series of tests on zebrafish embryos [69]: 50μm glass beads were inserted at various positions in and around the heart. Beads placed at the sinus venosus (i.e. the atrial inlet) or at the back of the ventricle obstructed blood flow into or out of the heart respectively. This resulted in significant increases in regurgitation as well as an estimated ten-fold reduction in shear stress within the heart. Hearts developed severe defects in the form of abnormal chamber formation, abnormal cardiac looping, and fusion of walls at the inflow and outflow tracts. Although researchers have directly altered blood flow in the zebrafish embryo, there is no standard procedure for doing so. A more commonly performed technique is to alter heart rate by changing the temperature of the embryo or to

decrease heart function by adding moderate to large doses of tricaine (a common fish anesthetic) [70].

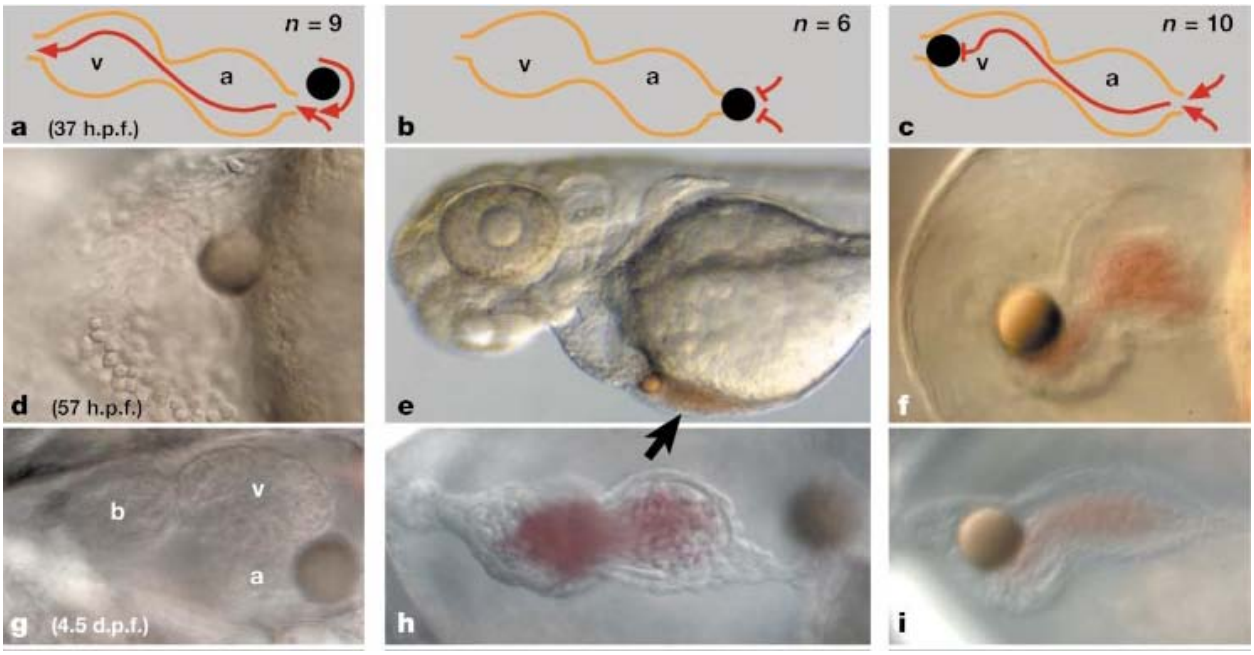

Figure 2.13 Obstruction of Flow in Zebrafish Heart
Hove et al. obstructed flow in the developing zebrafish heart by surgically implanting a bead at various locations. Parts (a), (d), and (g) are a control group in which the bead was placed near the atrial inlet without obstructing flow. Parts (b), (e), and (h) show the effect of a bead obstructing the atrial inlet. Parts (c), (f), and (i) show the effect of a bead obstructing the ventricular outlet. Both latter groups resulted in severe morphological defects. Figure taken from Hove et al., 2003 [69].

These studies provide definitive evidence that mechanics have a very real effect on heart development. Exactly which mechanical influence(s) has the greatest impact is difficult to determine; nearly all treatments presented above have the ability to change both blood flow pattern through the heart as well as loading on the heart. Computational studies are being utilized to examine these variables, and it appears that morphological changes in the developing heart are preceded by changes in hemodynamics [71]. Even with some questions unanswered, it is clear that the heart requires normal blood flow to develop properly.

2.9 Gene Expression and Mechanical Force

The research in this dissertation does not examine gene expression directly, but given how crucial gene expression is to development, it is an important concept to consider while observing the effects of manipulated blood flow. This section will provide only a glancing look at the impact of mechanical force on gene expression.

Shear stress likely impacts many genes, but three in particular have been singled out as particularly impactful: endothelin-1 (ET-1), endothelial nitric oxide synthase (NOS-3), and lung Kruppel-like factor-2 (KLF-2). Groenendijk et al. examined these genes by first observing expression throughout normal heart development [72]. KLF-2 was strongly correlated to regions of high shear stress. NOS-3 expression was weakly correlated to these same high-shear regions, and ET-1 expression seemed weakly correlated to regions of low shear stress. In all three genes, expression became more highly correlated to shear stress as the heart developed. This relationship would be expected since shear stress magnitudes should increase as the heart becomes stronger.

KLF-2, NOS-3, and ET-1 were examined again after vitelline vein ligation [73], and expression of each gene changed in response to the treatment. Expression patterns in treatment groups were consistent with increases in shear stress—an effect that seems unintuitive given that venous ligation should be decreasing cardiac loading and presumably decreasing shear stress. This is likely explained by localized changes in blood flow patterns that created isolated regions of higher shear stress. CFD modeling

of the chick heart confirmed that areas where KLF-2 was not expressed were coincident with areas of very low shear stress [73].

The importance of the expression of these genes is revealed in studies on knockdown mice. Knockdown of KLF-2 was often embryo-lethal and resulted in catastrophic thinning of the heart outflow tract and other important vessels [13]. Knockdown of ET-1 in mice resulted in similar malformations to vitelline vein ligation in the chick. Finally, knockdown of NOS-3 resulted in hypertension along with increased incidence of heart failure and septal defects [13].

KLF-2, NOS-3, and ET-1 are just a few examples of genes that play a role in mechanical response; it is likely that many genes are involved in the response to shear stress and mechanical strain within the developing heart. One other example is GATA-binding protein 4 (GATA-4), which has been linked to both mechanical loading and cardiac remodeling [74]. This area of research is still under investigation and we still have much to learn about gene expression in response to mechanical stress.

2.10 Imaging Modalities

Given the exceedingly small size of the embryonic heart, standard medical imaging techniques such as ultrasound, magnetic resonance imaging (MRI), and computed tomography (CT) do not have the spatial resolution necessary for useful biomechanical measurements. In order to observe embryonic hearts, it is necessary to utilize

microscopy. This section will briefly cover some advantages and disadvantages of some of the more common options.

Bright field imaging is perhaps the most basic of all the imaging options, but has outstanding spatial and temporal resolutions that far exceed most other options. Spatial resolution is essentially limited by the magnification on the microscope and the pixel density of the camera sensor. Temporal resolution depends on the camera's frame rate and lighting intensity, but can easily reach thousands of frames per second. Since blood cells can be seen clearly through the transparent heart walls, blood flow patterns can be directly observed. One of the biggest limitations of bright field imaging is that it requires a transparent sample. This makes it very well suited for the zebrafish heart and nearly useless on the chick heart. Another limitation of bright field imaging is its generally thick focal plane. This makes it less suited for reconstructing 3D images of the sample.

Laser scanning microscopy is a highly-limited imaging modality which also has notable strengths in particular situations. It essentially works by rapidly imaging a single line (i.e. scan) in space and then splicing the acquired lines together such that the same spatial data is plotted over time. This is the same concept as an m-mode image in ultrasound and results in a spatiotemporal plot (also called a kymograph). As motion (such as blood cell movement) occurs along the line, it appears as a streak whose angle corresponds to the cell's velocity. Scans can be taken at over 2000 Hz, allowing for the measurement of blood velocities well beyond that typically seen in the embryonic zebrafish heart [70]. Scans can also be taken perpendicularly in order to measure

lumen diameter. This method has been applied to the zebrafish aorta to make accurate measurements of blood velocity, flow profiles, vessel diameter, and flow rates [70]. The severe limitation of this technique is that only a single line of spatial information is taken at a time. It is thus difficult to make measurements involving the overall heart morphology. It is also limited to optically transparent specimens.

Confocal microscopy, by comparison, has nearly the opposite set of strengths and weaknesses. Confocal microscopy works by exciting and viewing fluorophores within a specimen. It therefore requires fluorescent labeling or bioluminescence to work. It is somewhat limited to optically transparent specimens, but can see through minor obstructions that would cause problems with bright field imaging. It is therefore sufficient for viewing the zebrafish embryonic heart [37]. Confocal microscopy allows for very precise focal planes, so 3D images can be created from combining images at different focal planes. As useful as the observation of 3D heart structure can be, this method is not well-suited to measuring blood flow characteristics other than flow direction. In addition, it requires sophisticated algorithms to sync up cardiac phase data into a coherent image [37]. Even then, spatial and temporal resolution is fairly low compared to other methods.

Optical coherence tomography (OCT) is conceptually similar to ultrasound, except that light is used rather than sound. Laser light is transmitted into the sample, and an image is reconstructed based on the light which is reflected back. OCT is quite limited in the depth it can penetrate (on the millimeter scale), but it is very well-suited for imaging the

embryonic chick heart. OCT has recently become very popular for making measurements on the chick cardiovascular system [16, 17, 75-79]. 2D images can be acquired in the vicinity of 300 frames per second (fps) [79]. 3D images can be reconstructed by sampling 2D images on multiple focal planes. OCT can also be used to measure peak blood velocities simultaneously with image capture, much like in Doppler ultrasound [17]. This is useful for basic observation of blood velocity but is sensitive to the exact angle of the laser and is prone to interference from heart wall motion. Overall, OCT provides an excellent means for observing heart structure and heart wall motion. Newer OCT-based techniques are being developed which can use the embryo's blood cells as tracer particles to perform micro particle image velocimetry (OCTμPIV) [75, 76].

2.11 Measuring Embryonic Heart Function

Recent publications describe an extensive methodology for measuring heart function in the embryonic chick [16, 80]. OCT imaging was used to take 2D image slices along the outflow tract which were used to create 3D images at each stage of the cardiac cycle. These were analyzed to obtain values for blood velocity, cross sectional shape of the outflow tract, change in outflow tract radius over time, and heart wall strain rate. A CFD model of the outflow tract was also created in order to get a more accurate estimation of blood flow patterns and velocity. Methodologies like this will undoubtedly broaden our understanding of the forces associated with heart development.

Such a methodology does not currently exist for the zebrafish model. To date, the methods used for describing zebrafish embryonic heart function have been inconsistent, making it difficult to compare results across different studies and developmental time points. Blood velocity has previously been calculated by tracking individual blood cells as they move through the heart [41, 46]. This method works well in the earliest stages of circulation, when blood cell concentration is relatively low. As blood cell concentration rises, it becomes increasingly difficult to track individual cells throughout the heart. Particle image velocimetry has also been applied to the zebrafish heart [69, 81], but this too has complications (e.g. sub-optimal seeding density, interference from surrounding tissue, and partially obscured blood cells at the orifices) which can lead to questionable results.

Spatiotemporal (ST) plots do not rely on the direct tracking of cells and have been used extensively for the measurement of blood velocity in vessels [70, 82-88]. Details of this method will be described in Chapter 4. Briefly, an ST plot is created by plotting a single line in space (i.e. “reference line”) over a sequence of frames in time. This is the same concept as M-mode images in ultrasound and laser scanning microscopy. When this reference line is oriented parallel to the flow of blood, blood cell movement is captured in the resulting ST plot as streaks whose angle represents the blood velocity. Automated methods have been established to determine the streak angle using mathematical transforms [82, 89]. This greatly reduces analysis time while removing a source of human error. ST plots are an excellent tool for quickly and accurately calculating blood velocities.

PIV is one of the more promising methods used for measuring flow in the zebrafish. PIV is used extensively throughout experimental fluid mechanics and is extremely useful for describing flow patterns. PIV works by imaging a flow which has been seeded with particles. Typically this is done by shining a laser sheet through the fluid in order to illuminate the particles within a single plane. High speed images are recorded from a camera looking orthogonally to the illuminated plane. Next, computer software is used to divide the images into a grid. The pattern of particles within each grid sector is compared between successive frames and a cross correlation algorithm is used to calculate the displacement of particles within the sector. This is done across the entire grid and across the image sequence. From this, a time-resolved grid of flow velocity is created and is typically shown as a velocity vector field. The velocity at any point in the flow field can be calculated by interpolation. Further analysis can be performed to calculate other parameters such as fluid shear stress and vorticity. PIV reveals a great deal about the nature of a flow and is difficult to beat as an experimental tool.

As if to demand the use of PIV, the embryonic zebrafish heart is transparent, and blood cells essentially act as natural tracer particles. At the start of this project, PIV had been used only once (to my knowledge) in the zebrafish heart [69]. The measurements made were rough, however, and were used to simply show the large-scale flow patterns of blood flowing between the heart chambers (Figure 2.14). This left ample room for further application of PIV to glean more detailed information from intracardiac flows. Very recently, PIV has been used to take a closer look at flow through the zebrafish heart [81, 90, 91]. Jamison et al. have developed a sophisticated algorithm for removing

much of the background noise that previously caused serious problems with PIV results in zebrafish (Figure 2.15). Lee et al. have used CFD in combination with PIV to estimate wall shear stress and pressure within the embryonic heart. PIV is not necessarily the best option for analyzing embryonic blood flow because blood cells are not ideal tracer particles; ideally they should be smaller, more densely seeded, and should flow closer to the wall [92]. Also, PIV alone does not describe the actual function of the heart (e.g. flow rate, stroke volume, etc.). Still, with the improvements being made in image processing and analysis, PIV will likely prove to be a tool of major importance in the near future.

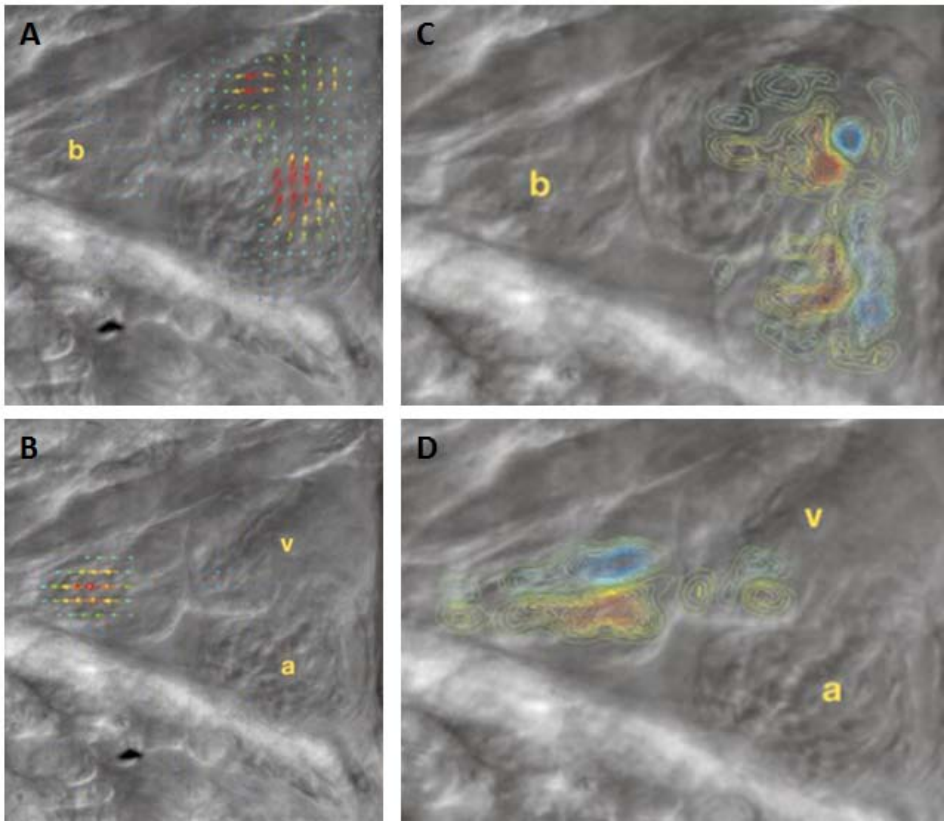

Figure 2.14 PIV Results from Hove et al.
PIV results from a zebrafish at 4.5 days post-fertilization (dpf). Velocity vector fields are shown during ventricular diastole (A) and ventricular systole (B). Vorticity is shown during ventricular diastole (C) and ventricular systole (D). (C) and (D) show pronounced vortices which form within each chambers. Abbreviations: a = atrium, v = ventricle, b = bulbus. Figure adapted from Hove et al., 2003 [69].

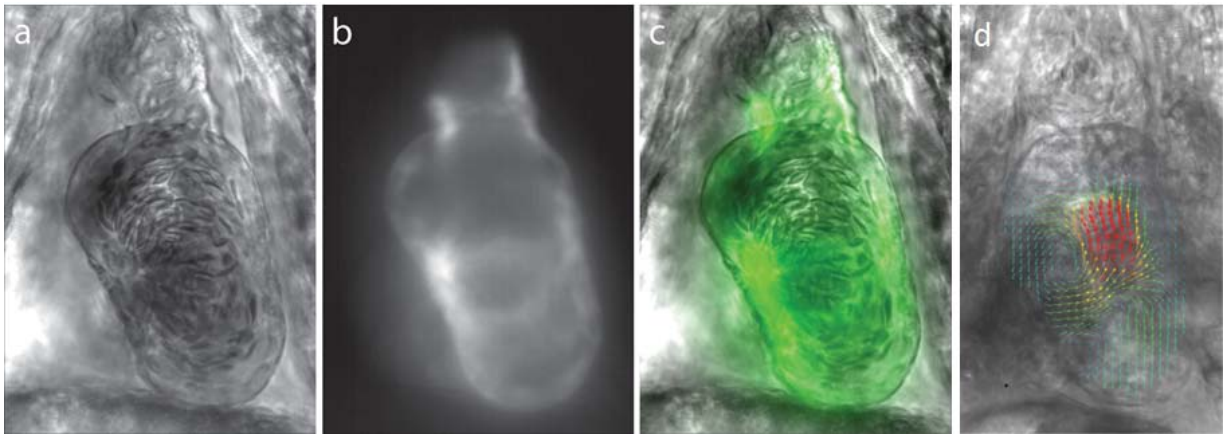

Figure 2.15 PIV Results from Jamison et al.
Image processing and PIV results from a zebrafish at 6 dpf. Bright field images (a) are synchronized with fluorescent images (b) are combined to create a dynamic mask of the heart (c). The mask helps eliminate background noise in the PIV which would otherwise cause inaccuracies in the results. The resulting PIV velocity vector field is shown in (d). Figure adapted from Jamison et al., 2012 [81].

2.12 Chapter Summary

From this review, it can be seen that the developing heart is exposed to a variety of mechanical stresses which are sensed by endocardial cells. This can trigger signaling cascades which affect the expression of genes critical to heart development. Much evidence supports the theory that epigenetics play an important role in heart development, but there is still much to be learned. A variety of imaging options and analyses can be used to quantify results from epigenetics studies. There are several standard models for altered mechanical stress in the chick, but no standard model has been developed for the zebrafish embryo. Nor is there a standard methodology for analyzing zebrafish heart function. There has been very little attention paid to exactly when in development the heart is susceptible to mechanical influences. This project aimed to fill some of these gaps and the results will hopefully bring us closer to understanding the causes of congenital heart defects.

CHAPTER 3: METHODS

3.1 Chapter Introduction

Here, the methods that are common to all experiments will be presented. This includes methods related to zebrafish handling and imaging. Aim-specific methods are included in each aim's respective chapter.

3.2 Zebrafish Breeding and Egg Handling

Colorado State University currently houses a zebrafish (*Danio rerio*) facility containing thousands of zebrafish, including a variety of transgenic and mutant varieties for use in cardiovascular development research. Fish were raised in accordance with Westerfield [93]. All research was performed on embryonic zebrafish within one week of fertilization. Unless otherwise noted, all fish used were wild-type zebrafish. Although these fish are referred to as "wild-type", they have been inbred for many generations. This greatly reduces the genetic variability between fish and ensures that random anatomic and physiologic variability is kept to a minimum. To obtain fertilized eggs, adult zebrafish were placed overnight in a container with a sieve bottom for separating eggs. Fertilized eggs were collected in the morning and placed in E3 embryo water (buffered water mixed specifically for the purpose of raising fish embryos). These were viewed immediately under a stereomicroscope and the time since fertilization was determined based on Kimmel's development stages [94]. Embryos were then placed directly in an

incubator at approximately 28°C. All time points beyond this point were based on the actual elapsed time added to the initial age of the embryo upon incubation. At the time point of interest, embryos were removed from the incubator and were dechorionated using tweezers.

3.3 Zebrafish Imaging

The exact image preparation protocol depended both on when the experiment took place and on the developmental phase of the embryo. The latest and most successful of the protocols will be described here. These protocols were used for all experiments in Aim 3 and for the benchmarking portion of Aim 2. Alternative and unsuccessful protocols are described in the next section. A solution of 1.5% low gelling temperature agarose (Sigma-Aldrich, Type VII-A A0701) was prepared by melting the agarose powder in embryo water via microwave oven. The solution was heated in 15-second increments and stirred thoroughly between heating periods. Once completely dissolved, the solution was placed in a small beaker within a water bath held at 37°C. 37°C was a particularly convenient temperature for preparation because it allowed exactly enough time to position the embryo before gelling occurred. Note that the agarose melts at approximately 60°C and gels at approximately 26°C. Agarose solution was transferred to a small petri dish lid using a pipette. The solution gels in approximately 2 minutes after removing it from the water bath. After walking the dish to the adjacent microscope room, a dechorionated embryo was transferred to the agarose solution. Close examination of many embryos confirmed that the gel temperature was warm enough to

increase heart rate, but not warm enough to stop the heart or otherwise damage the embryo. Dental picks were used to position the embryo into the desired orientation. To get a direct view of the developing atrium between 36 and 72 hpf, this view was obtained by positioning the tail downward into the gel while rotating the embryo backward slightly to expose the anterior-ventral view. The gel surrounding the embryo was carefully scraped with the dental pick in order to maintain the given position until the gel set. Once set, embryos were unable to move out of position. Embryo water was then added to the top of the gel to keep it hydrated. This protocol was chosen because it is relatively quick and simple and most importantly does not require the use of anesthetics which are known to affect heart function.

Embryos were imaged using a high speed camera (Photron FastCam SA3) affixed to a stereomicroscope (Olympus SZX12 with affixed AL-20X lens attachment) as shown in Figure 3.1. Images were acquired at 1500 frames per second at maximum magnification (approximately 225X). This resulted in digital images with a spatial resolution of 1310 pixels per millimeter. In order to capture images at this magnification, it was necessary to use a 150W fiber optic microscope illuminator (Schott, Ace) at near-maximum power. The camera was controlled with Photron FastCam Viewer software. For experiments in Aims 2 and 3, no less than 6 full cardiac cycles were captured per imaging sequence.

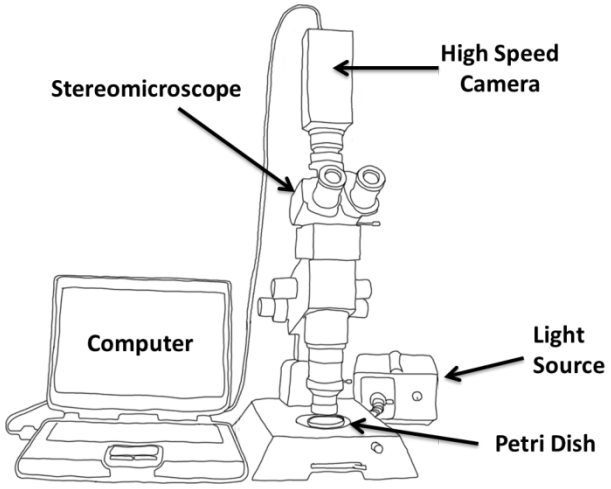

Figure 3.1 Schematic of Equipment
All imaging was performed using a high speed camera attached to a stereomicroscope.

After imaging, embryos were removed from the gel by carefully cutting the gel with a dental pick such that the cut ran up to and along the embryo's midline. The gel was then pulled to one side with the pick and, when necessary, the embryo was flushed out of the gel by gently squirting it with embryo water. Embryo recovery rate was in the realm of 90-95% and could be increased with increasing prudence.

3.4 Alternate Zebrafish Preparation Protocols

Alternative methods for imaging zebrafish have been presented in past articles, and many of these were tested before arriving at the methods described above. Several other research groups who work with zebrafish also use low melting agarose gel, but this is usually done in combination with tricaine (a fish anesthetic also known as MS222 and MESAB) [69, 81, 95]. At low doses, tricaine mainly affects skeletal muscle and prevents embryos from twitching. However, tricaine is known to act on the heart as well, and in higher doses it can dramatically reduce heart function [96] or even stop the heart

[97]. I found that the addition of tricaine is not necessary for immobilization of embryos within gel.

Other groups have simply anesthetized zebrafish with tricaine and then positioned the fish in agarose wells or channels [37, 41, 48, 98]. This theoretically requires higher doses of tricaine in order to completely immobilize embryos, making this a questionable method for use in studies investigating heart function. In addition, this method makes it significantly more difficult to position the fish at certain orientations, as the embryo tends to settle at angles which may not be ideal.

Petzold et al. presented a concept for mounting and imaging zebrafish which seemed to have strong potential for rapid positioning of embryos [99]. Their method is centered on the idea of matching refractive indices of the containing chamber and the fluid. Specifically, they proposed the use of fluorinated ethylene propylene (FEP) tubing to be used with embryo water. Zebrafish embryos can easily be sucked into this tubing which can then be submerged in water. Since FEP tubing has virtually the same refractive index as water, there is virtually no optical distortion when viewing the zebrafish (Figure 3.2). The tubing can then be rotated to position the fish as desired.

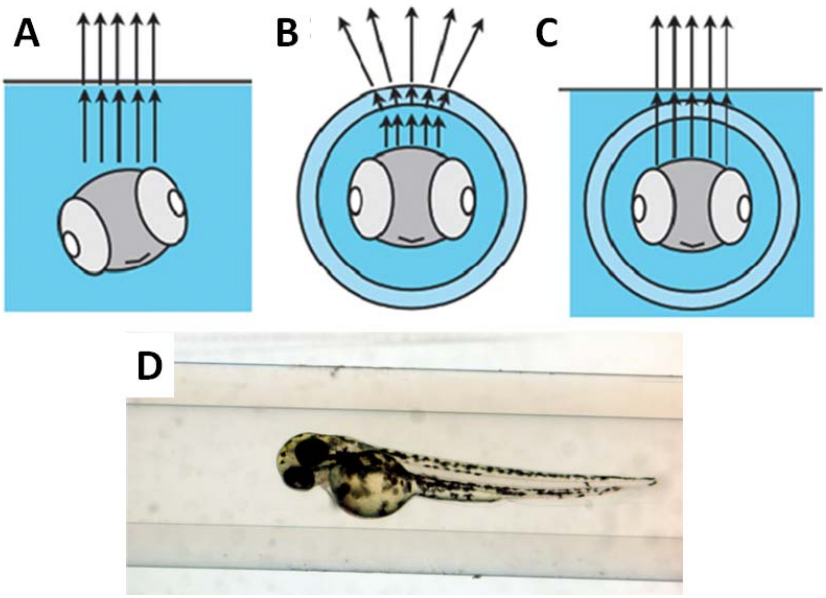

Figure 3.2 FEP Tubing for Distortion-free Zebrafish Imaging
When a zebrafish embryo is viewed directly through water (A), there is no distortion since light passes through only the flat surface of the water. When the embryo is within tubing which does not match the refractive index of its surroundings, the image is distorted as light bends through the curvature of the tubing (B). If the refractive index of the tubing and fluid are matched (i.e. FEP tubing in water) (C), then there is no distortion. Tubing allows for more controlled positioning of the embryo into an orientation ideal for viewing. Parts (A-C) are adapted from Petzold et al., 2010 [99]. Part D is my own image which was taken during the testing of this method.

The group also suggested that various liquids such as methylcellulose, sucrose, and low gelling agarose could be used with different types of tubing. Most suggestions were attempted with little success. The methods allowed for the viewing of the embryo with negligible distortion, but it was difficult to position the embryo effectively for viewing the heart; the ideal angle for viewing the heart requires the embryo to be steeply positioned so as to expose the anterior/ventral angle. At such a steep angle, the embryo naturally slides down the tubing and out of position. This could be overcome by using low gelling agarose within the tube so as to immobilize the fish, but it is exceedingly difficult to then remove the fish from the tubing without damaging it. This method could be highly effective for achieving certain viewing angles but it is not very useful for the measurements sought in this study.

CHAPTER 4: AIM 1

4.1 Chapter Introduction

The overarching goal of this research was to investigate the effect of altered mechanical loading on heart development using the zebrafish embryo. To do this, it was important to use quantitative measurements which were able to provide a big-picture description of the heart's ability to pump blood. Although several techniques have been used to quantify various aspects of heart function and blood flow, none can be considered a gold standard and many were severely limited by either the imaging technology used [37, 70] or by the assumptions that were made [95]. Aim 1 was to develop a methodology for quantifying heart function in the zebrafish embryo. This methodology was developed for use with the high-speed bright field images acquired from the protocols described in section 3.3.

4.2 Failed Approach 1: Particle Image Velocimetry

Multiple approaches were pursued before arriving at the final method used for Specific Aims 2 and 3. These alternate approaches led to varying degrees of success. The first, and perhaps most obvious, approach was to use particle image velocimetry (PIV). At a glance, it seems that PIV should be a nearly perfect option for flow analysis in the embryonic heart; PIV is outstanding for visualizing large scale flow patterns as well as quantifying velocity and vorticity within a flow. In addition, blood cells can act as natural tracer particles. However, a few issues drastically complicate the use of PIV. The first

and most problematic of the issues is the motion of the endocardium relative to the blood cells. Cells of the endocardium are approximately the same size as blood cells, and in bright field lighting, can look nearly identical. The heart walls come together during contraction, and the endocardium is frequently pulled in opposition to the flow of blood. From an automated analysis perspective, the endocardium is extremely difficult to differentiate from blood cells and leads to direct error in velocity calculation. The algorithms of commercial PIV software are made to recognize flow patterns and interpolate and connect various parts of the flow. When the algorithm sees a forward burst of flow through the atrial inlet in combination with the retrograde motion of the endocardium itself, it naturally recognizes it as a vortex. The incorporation of wall motion into the overall blood flow pattern occurs across the entire heart and is very difficult to prevent.

This problem was experienced when applying PIV analysis to images of the zebrafish heart and the results contained a menagerie of false vortices which extended beyond the heart boundary. In an attempt to mitigate this effect, I programmed a manual spline-based mask-drawing algorithm in Matlab. With this, a series of spline nodes could be arranged along the heart wall boundary which followed the wall throughout the image sequence. These splines were used to define a mask which blocked out the portions of the image which lied beyond the interior of the heart. Although this helped eliminate some of the tissue-induced false flow patterns, Figure 4.1 demonstrates that this was not nearly enough to eliminate the problem in general. The masking of the heart boundary was perhaps a hopeless endeavor from the start because the boundary

between the bright field image and the black background mask is easily detected by the PIV software (in this case DaVis) and is incorporated into the calculation. Theoretically, the mask boundary can be considered a zero-velocity boundary and this effect can be largely eliminated, but the DaVis software did not (at that time) have the capability to incorporate a dynamic mask into its calculations.

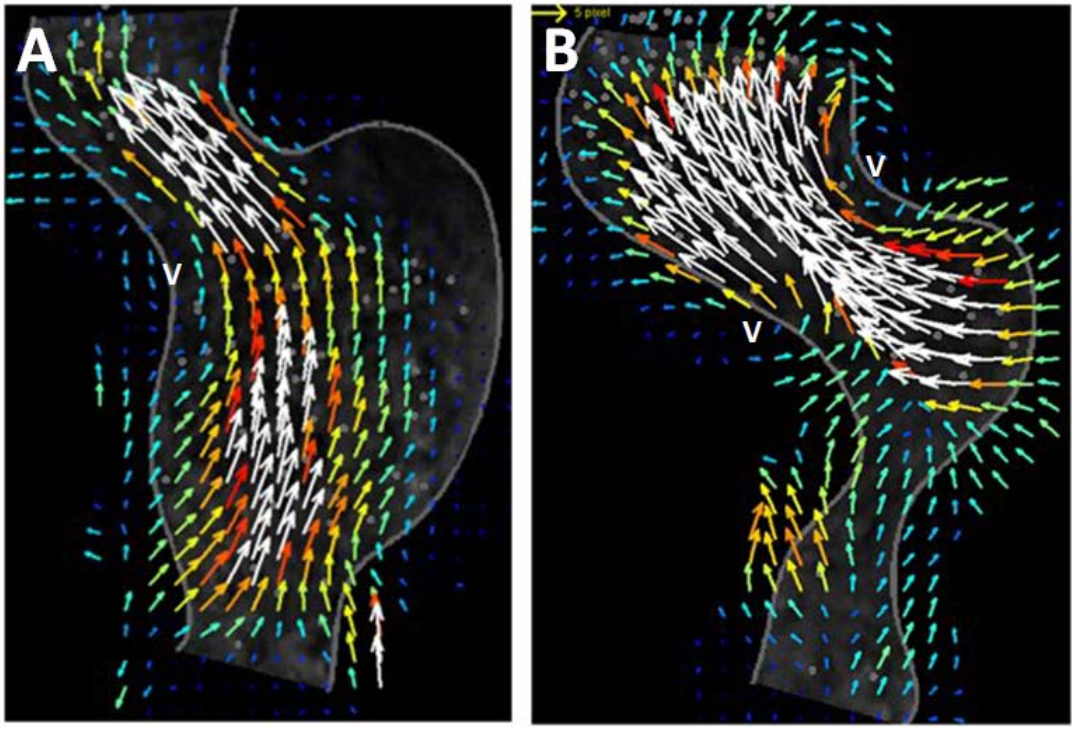

Figure 4.1 PIV Results
Results of PIV analysis of the heart at 48 hpf are shown during early atrial systole (A) and late atrial systole (B). Many relatively large magnitude vectors can be seen well beyond the heart boundary and there was also a tendency for the software to calculate false vortices (symbol v) in the flow which extended beyond the heart wall boundary. These are some of the more accurate results which were obtained after masking the background and adding cell-tracked foreground dots.

In a final attempt to increase the accuracy of the calculations, I programmed manual cell-tracking Matlab functions in which cells were tracked semi-automatically throughout the cardiac cycle via mouse click. Cells were tracked at varying frame increments and the position between tracked points was interpolated for increased accuracy and

decreased analysis time. Cell locations were then plotted as circles in a high-contrast image-overlay which was easy for the PIV software to detect. Even this was not enough to overcome the general error of the technique.

There is a simple way to avoid these problems entirely: use a transgenic zebrafish line with fluorescent blood cells and image the heart under fluorescence. Under these conditions, the entire background is completely black and the only emitted light comes from the fluorescing blood cells. Since the heart wall does not fluoresce, there is no worry about misidentifying wall motion as blood cell motion. As convenient as this option could be, the available high-speed camera (Photron FastCam SA3) did not have a sensitive enough sensor to detect fluorescing blood cells at frame rates adequate for blood velocity calculations. Even at low frame rates, the fluorescence signal was at a similar magnitude as the background noise.

A much more complicated option for addressing the same problem is to remove background patterns that repeat identically over several cardiac cycles. This can be done by synching images across cardiac cycles and subtracting out any pixels that remain consistent. Since the heart repeats more or less the exact same motion on every cycle, its motion would be eliminated. Although blood would naturally flow in the same pattern on each cycle, the individual blood cell positions would change cycle-to-cycle and would not be eliminated. Over the course of many cycles, this method should be quite effective at eliminating all background signals, including heart wall motion. This method is highly sensitive to camera vibration, as it is critical that pixels align properly

frame to frame. As described in the literature review, another group has since begun a similar endeavor to remove background noise with image processing in order to use PIV for blood flow analysis in the zebrafish heart [81].

4.3 Failed Approach 2: Manual Cell Tracking

My next approach was to focus on individually tracked cells through the heart. This technique could be considered primitive compared to more advanced techniques, but it has been used in at least one very high impact article [41] and works fairly well for calculating the velocity of individual cells; velocity is calculated by simply dividing the spatial displacement of a cell by the time span between frames. This was one of the primary analyses used in my first publication [46], in which I described the changing pumping mechanics of the embryonic zebrafish heart throughout early development.

Although useful, this method has a long list of problems and limitations. One of the major problems is that this method is quite prone to human error and bias. As blood cell concentration increases, it becomes more and more difficult to track individual cells as they move in and out of the focal plane and become obscured by surrounding cells. It can be quite difficult to figure out where a cell moved from frame to frame when cell velocities are high, and it is nearly impossible to eliminate human bias. Unlike PIV, which produces a grid of velocity values and interpolates to find the velocity at any point of interest, cell tracking provides velocity information only at the location of a cell. Interpreting velocities at particular areas of interest can become very complicated and

error-prone. One approach to countering this problem is to define a region of interest (Figure 4.2) and to calculate the velocity based on the average of points within the region. This, however, does not take the flow profile into account and can easily lead to a large underestimation of actual blood cell velocity. Finally, the method is incredibly time consuming and does not lend itself for use in large data sets. After programming many functions which attempted to mitigate some of these issues, it became quite clear that a different method would be necessary.

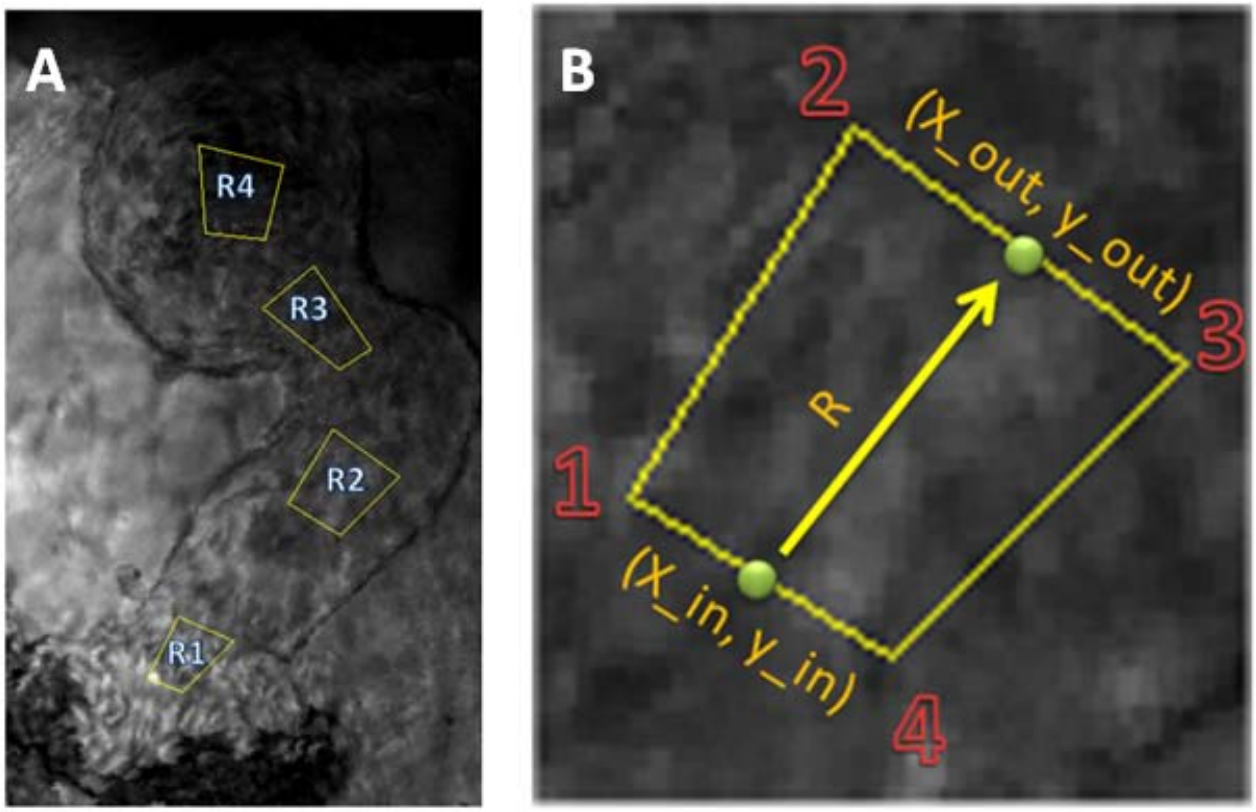

Figure 4.2 Regions used for Calculating Blood Velocity at Key Points
Several ideas were pursued in analyzing the velocities calculated from individually tracked cells. One idea was to define specific regions of interest in the heart (A) in which velocities would be averaged to create a velocity vector, R, for each region (B). This idea was ultimately rejected, as it cannot account for the changing lumen diameter and flow profile.

4.4 Overview of the Final Methodology Used for Calculating Heart Function

After the previous methodological failures, a much more robust method was developed based on a combination of techniques used in previous studies. The methodology can be broken into five distinct parts: image acquisition, image processing, blood flow analysis, measurement of heart lumen diameter, and estimation of derived parameters (Figure 4.3).

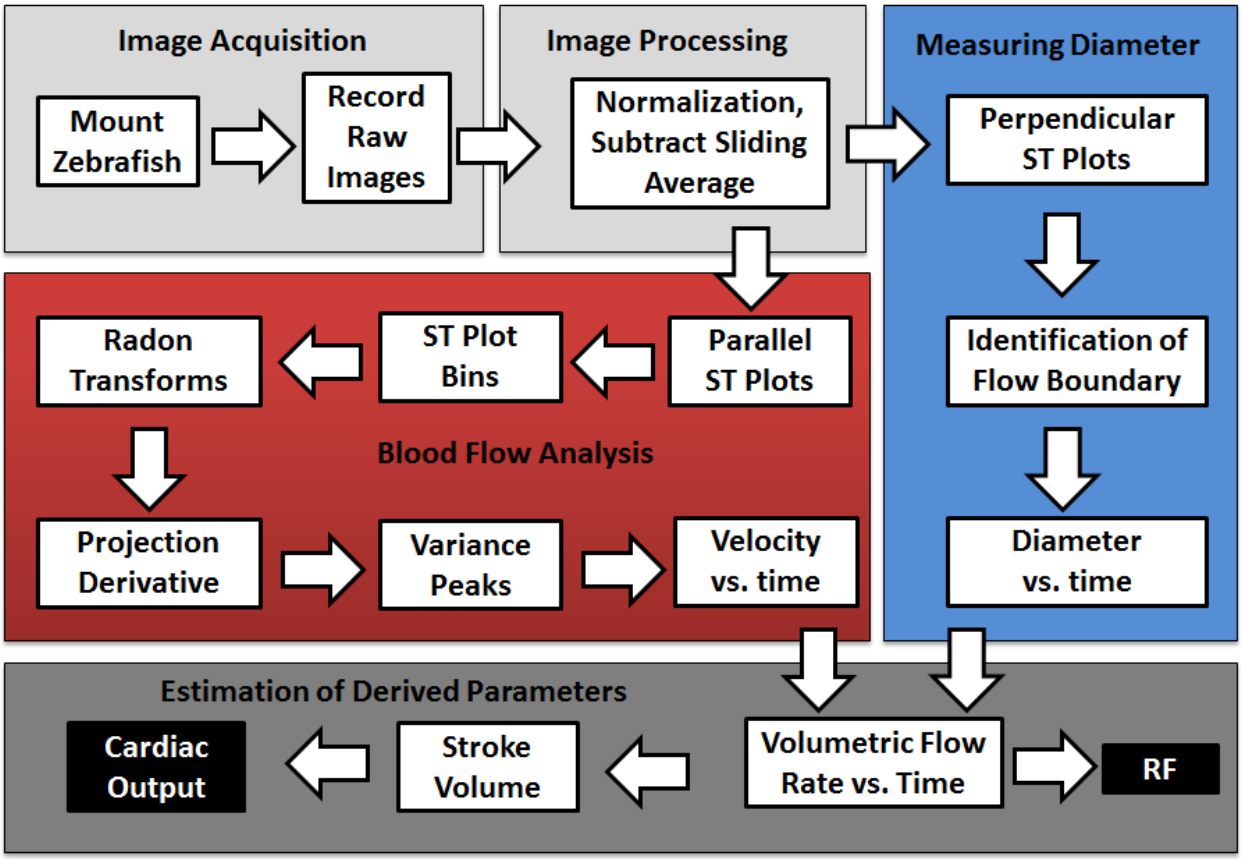

Figure 4.3 Flow Chart of Methodology
The flow chart above outlines the process used for quantifying embryonic heart function in the zebrafish.

In brief, high-speed image sequences of the heart are recorded. The images are normalized and heart wall and blood cell motion are isolated using difference images. Processed image sequences are analyzed using parallel and perpendicular reference lines to create spatiotemporal (ST) plots. Blood velocity is automatically calculated by applying Radon transforms and statistical techniques to parallel ST plots, while wall diameter is estimated from perpendicular ST plots. Flow rate is estimated by multiplying blood velocity by the cross-sectional area of the atrial inlet. Cumulative blood volume and retrograde flow fraction (RFF) are estimated by integrating the flow rate vs. time. Lastly, cardiac output can be estimated by multiplying the heart rate by the estimated stroke volume. This process estimates several important quantitative parameters that describe blood flow and overall heart function.

4.5 Image Intensity Normalization

All image processing and data analysis was performed using an in-house Matlab interface. The goal of the image processing steps was to reduce background noise and isolate movement within the image sequence. Since frame-to-frame lighting variation can potentially create artifacts in the later steps of the analysis, image intensity was first normalized. This was done by selecting an area of the image sequence that remained static for all frames. The intensity of each image was then multiplied by a factor such that the average intensity of the selected area matched the overall average intensity for the selected area across the entire image sequence.

4.6 Isolation of Movement within Image Sequences

Processing was used to isolate movement between frames, which dramatically strengthened the signal to noise ratio in subsequent ST plots. Difference images have been used in previous studies to isolate movement within image sequences [88, 100]. A similar approach was used here, whereby the sliding average pixel intensity was subtracted from each frame as follows:

$$I'_n = I_n - \frac{1}{W}\sum_{m=n-W}^{m=n-1} I_m$$

where I_n is the pixel intensity of the image at frame *n*, and W is the width of the averaging span (in frames). By subtracting the sliding average, all portions of the image that remained static throughout the averaging span were removed; the resulting image sequence, I', contains only the moving blood cells and heart wall. Span width was varied between 2 and 6 frames. Figure 4.4 compares the raw data to the processed data.

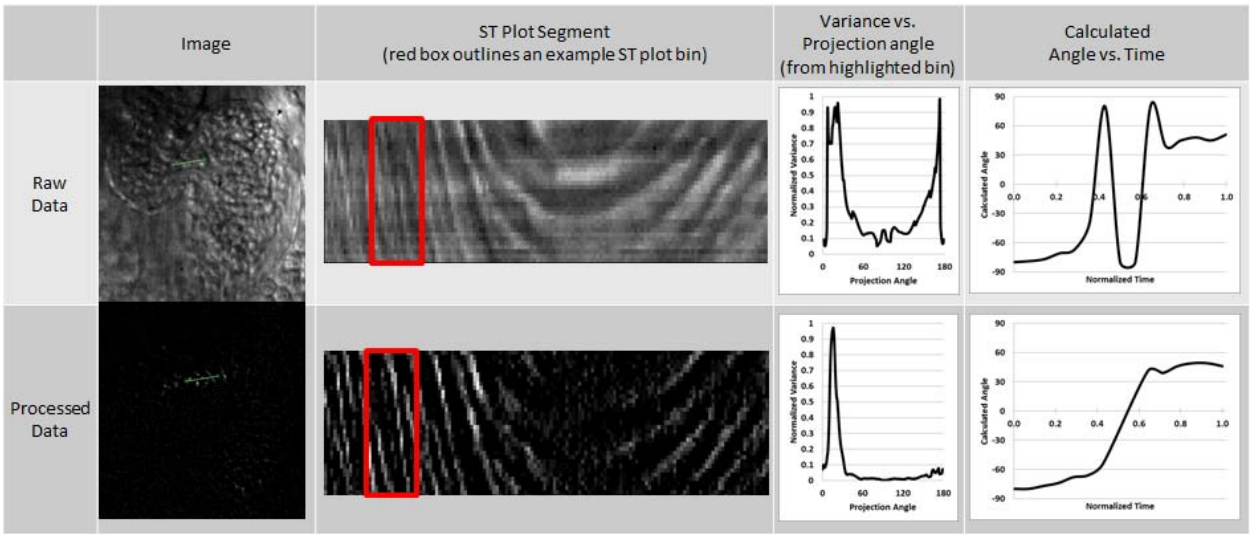

Figure 4.4 Image Processing
A comparison is made between the unprocessed data (top row) and the processed data (bottom row). The image processing subtracts static portions of the image, creating a black background. Moving portions of the image are easily seen as gray/white pixels. The upper ST plot segment reveals notable background artifacts, including horizontal and vertical streaks, which are removed in the processed ST plot. Unprocessed variance plots from Radon transforms reveal two prominent peaks. The peak near 180 degrees is created by background artifacts. The contributions from these artifacts also broaden and obscure the true peak, which is unmistakable in the processed variance plot. At slower blood velocities, background artifacts tend to dominate the calculations on unprocessed images (seen as oscillation in the middle of the plot). These oscillations are entirely removed in processed data.

4.7 Creation of Spatiotemporal Plots

Spatiotemporal (ST) plots can be used to determine the velocity in a predetermined direction, and are an essential part of the methodology. ST plots are created by plotting the same line in space (referred to here as a 'reference line') over a period of time (Figure 4.5). Blood velocity can be measured by orienting the reference line parallel to the direction of flow. As blood cells move along the reference line, they create a pattern of streaks in the resulting ST plot. As the name suggests, the ST plot is a plot of space versus time. Thus the velocity can be determined by calculating the slope of the streaks: the change in space over the change in time (dy/dt in Figure 4.5). Because velocity is determined along a reference line, ST plots are particularly well-suited to 1D flows, like

those in a blood vessel. Flow patterns can be somewhat complex inside the heart, but at the constrictions (such as the atrial inlet) blood is ejected in a nearly 1D fashion.

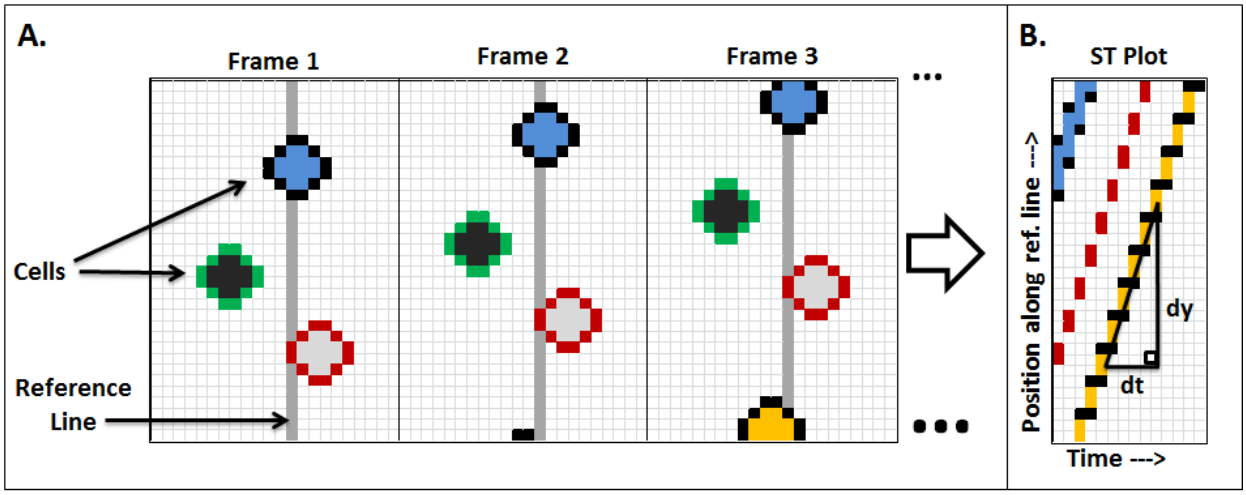

Figure 4.5 Creation of Spatiotemporal Plots
Part (A) shows a series of three consecutive frames with mock cells moving in the vertical direction. The vertical gray column marks the pixels that lie along an arbitrary reference line. The pixels along this line are extracted from each frame and plotted side by side to create the ST plot in (B). As cells move along the reference line, their changing positions are seen as an angled streak in the ST plot. The vertical axis of the ST plot represents position along the reference line, while the horizontal axis represents time. The velocity of the cells along the reference line can be determined by calculating the slope (dy/dt) of the streaks in the ST plot.

ST plots were used to calculate blood velocity at the atrial inlet. In order to simplify the analysis and save computing time a single reference line was used to measure the velocity of the inlet. This reference line was oriented in the direction of blood flow and placed as close as possible to the center of the atrial inlet. In order to ensure that it remained centered, Matlab functions were programmed which allowed the reference line to be set in position at any desired frame (i.e. a key frame). After centering the reference line at key frames throughout the first cardiac cycle, the functions were used to interpolate its position at intermediate frames. The reference line motion was repeated for each successive cardiac cycle since beat-to-beat wall motion was nearly

identical in the vast majority of samples. ST plots were then created based on the dynamic position of the reference line. Because the reference line followed the same motion as the heart, it essentially remained stationary with respect to the atrial inlet and resulted in a negligible amount of motion-artifacts.

4.8 Advantages and Limitations of ST Plots

A major advantage of using ST plots is that it eliminates the need to track individual cells. The streak pattern is simply a result of movement along the reference line. Whether that movement is from sharply defined cell boundaries or a blurry cluster of cells, it will still result in angled streaks corresponding to velocity. A distinct advantage of ST plots over PIV is the fact that velocities can be determined along a precise line in space; all data in an ST plot can be extracted from a single reference line in the exact area of interest while PIV uses 2D cross-correlation to determine displacement in a small 2D area. ST plots can produce far more accurate results in places where blood is traveling through a very thin channel between moving wall boundaries (as is the case during portions of the cardiac cycle). This same aspect is also extremely limiting because velocity is defined only along a given reference line, and the calculated velocity is only the component of velocity along the reference line. These two limitations can be addressed by using multiple reference lines and either auto-orienting the lines to the flow or by calculating movement between reference lines at different angles to calculate the true flow direction. These limitations can be avoided entirely by only applying the technique in an area of 1D flow such as a blood vessel (or in this case, the heart inlet).

4.9 Location of ST Plot Measurements

The use of ST plots for blood flow measurement can be applied at the inlet, AVJ or the ventricular outlet; indeed any location where blood flow can be seen and cross-sectional area can be estimated are potential locations for this analysis. The ventricular outlet is only visible at very limited points in development (~55 +/- ~5 hpf) when using bright field microscopy. The AVJ is a more accessible location. However, the motion of the AVJ is much more pronounced than the atrial inlet, which is essentially anchored in the same location throughout the cardiac cycle. As the heart contracts, the AVJ can move as much as ~30 microns which complicates processing. Dynamic reference lines can be applied to follow this movement, but other problems persist; blood velocities through the AVJ are much greater than at the inlet and flow width is significantly more difficult to determine. These factors increase the error within the analysis. Flow rate into the atrium must equal the flow rate out of the flow rate for each cycle, so the values obtained at the AVJ can be compared to the inlet to help validate results. An additional consideration is the fact that it is far easier to image one orifice rather than two simultaneously. This forces the researcher to choose which orifice to image. Since the goal of the research was to measure general heart function and not necessarily to compare the flows between orifices, analysis was performed almost exclusively on the atrial inlet.

Useful information can be gained by analyzing the AVJ. Indeed the AVJ is a critical region of the heart since it is the location of the future AV valve. Shear stress and regurgitant flow within the AVJ are expected to play an important role in the

development of the valve [48], so measurements of flow rates and blood velocity are of interest. Although not as accurate due to the reasons described above, an analysis of the flow through the AVJ may be a worthwhile endeavor.

4.10 Determination of the Profile Coefficient

Since reference lines were centered between the inlet walls, they were measuring the highest velocities in the flow. The flow rate calculations in later steps require that the average velocity for the entire lumen area be used, so it was necessary to calculate the relationship between the central (maximum) velocity and the mean velocity. To do this, a series of parallel reference lines were positioned across the entire width of the atrial inlet (Figure 4.6 A and B). Velocity values were calculated from each corresponding ST plot to create a flow profile (Figure 4.6C). Since some reference lines lay outside of the flow boundary, and because legitimate zero-value velocities were irrelevant to the calculation, all zero-value velocities were discarded in the analysis. For each profile, the flow width was estimated by considering the span of reference lines with non-zero velocity values. This flow width was used to estimate the cross-sectional area of the atrial inlet. Next, the peak velocity was compared to the calculated mean velocity through the atrial inlet. I found that the mean velocity of blood within the observable blood flow is approximately 0.74 times the peak blood velocity. I used this coefficient, which here is referred to as the ‘profile coefficient’, to calculate the mean velocity in all analyses that followed.

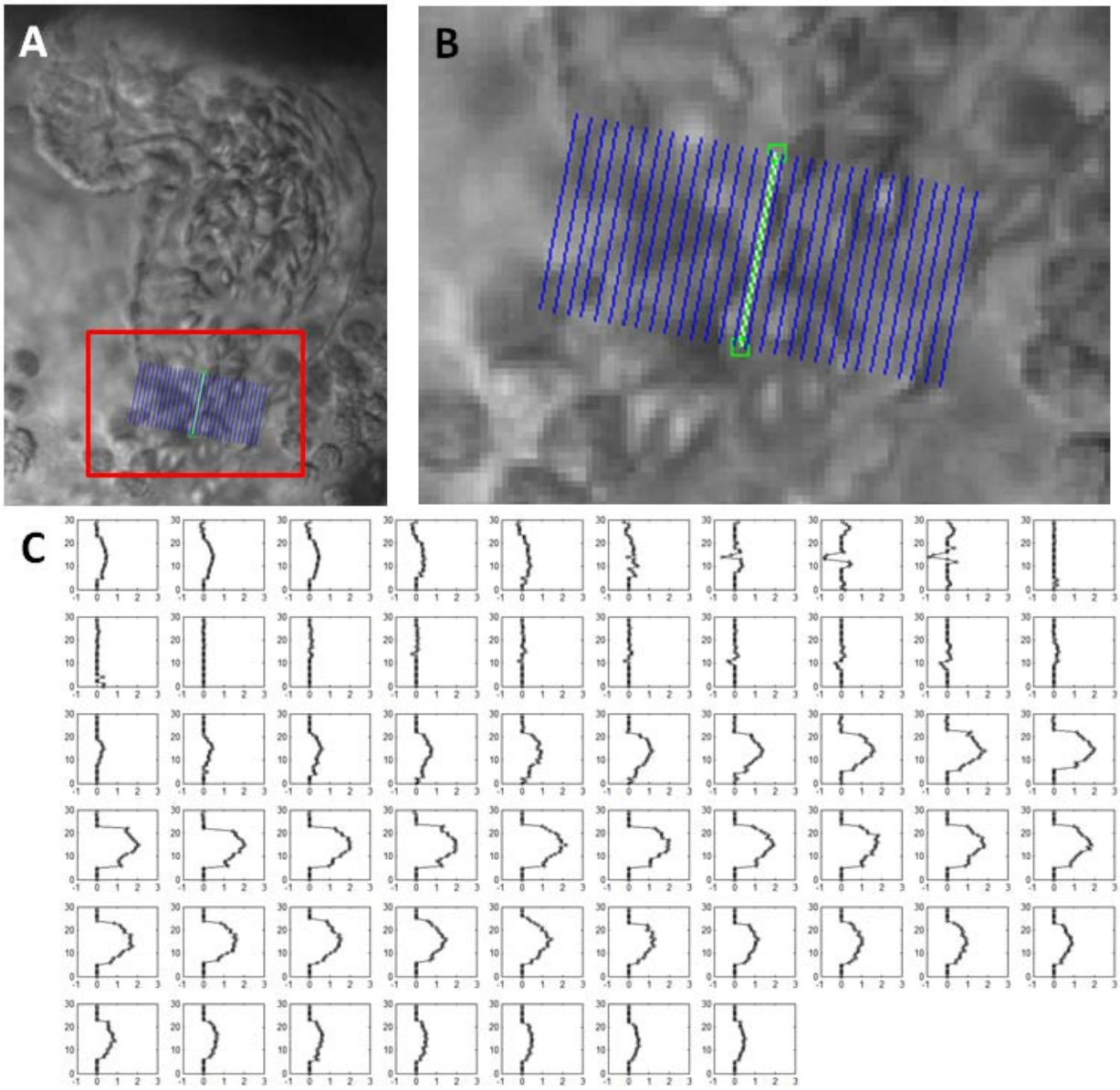

Figure 4.6 Flow Profile Analysis at the Atrial Inlet
Several parallel references lines were created to span the atrial inlet (A). A magnified version is shown in (B). Velocity was calculated from each reference line in order to create flow profiles across the entire cardiac cycle (C). The cycle in (C) starts at the beginning of atrial systole. Blood flows forward through the inlet as the atrial inlet walls contract, followed by a brief period of retrograde flow (row 1). There is a pause in flow as the atrial inlet walls remain contracted and blood is pushed out of the atrium (row 2). Once the inlet relaxes again at the start of atrial diastole, blood rushes into the atrium (row 3 through 6). Resulting profiles were used to calculate a coefficient used to determine mean velocity from peak velocity. Zero-value velocities within the profile were discarded from the calculations.

There are three important considerations that arise from this topic. One is that blood is technically non-Newtonian and that the flow profile is not necessarily in the form of a parabola as a Hagen-Poisseuille flow would predict. The second is that blood tends to flow closer to the center of vessels[70] and away from the wall. The last is that very low blood velocities cannot be detected using the analysis presented here because low values of velocity result in signal that is indistinguishable from background noise. The latter two points are a limitation of the methodology. Plasma surely flows across the entire width of the lumen, yet blood cells frequently flow more centrally such that they do not actually touch the wall. In the diameter tracking portion of the analysis, the diameter of the visible flow is tracked rather than the actual wall-to-wall lumen diameter. This creates an error in the calculations, but this error should be relatively small; blood flow follows the “no slip condition” which says that velocity at the wall is theoretically zero and increases as it reaches its peak at the center. Although the near-wall flow is unaccounted for in the calculations, it is at a much lower velocity and is likely very small compared to the fast, central flow. The fact that only the measurable, more central portion of the flow is used helps explain why the profile coefficient ended up being 0.74 instead of the theoretical 0.5.

A closer look at the variability of this coefficient could be insightful. The variability between fish was not examined. The variability across a single cardiac cycle was only examined superficially. As can be seen by the profiles in Figure 4.6, the shape of the profile is dependent on the velocity of the blood. At very low velocities, the profile appears parabolic in nature. This would result in a profile coefficient near the theoretical

0.5. However, as the velocity increases, the profile more closely resembles a plug flow, where the average velocity and peak velocity are much closer in magnitude. This would result in a profile coefficient nearer to 1. As described, the calculated average profile coefficient across the entire cycle was used for all velocities. Surely, more accuracy could be gained by applying a dynamic profile coefficient based upon the maximum velocity and a larger empirical dataset.

4.11 Determination of ST Plot Streak Angle using Radon Transforms

Blood velocity was found by determining the ST plot streak angle. This can be done in a precise, automated fashion through the use of Radon transforms (RTs), as shown in Figure 4.7. The concept of extracting the line orientation from Radon transforms has been described previously [82, 89], and has been shown to be faster and more accurate than alternative methods. In summary, a RT creates a new image by transforming the input image (i.e. an ST plot) into a domain spanned by image projections as a function of angle (Figure 4.7 C and D). The RT of the i^{th} ST plot bin image, $B_i(x,t)$, generates a new image $R_i(r,\theta)$:

$$R_i(r,\theta) = \frac{1}{LT}\int_0^L dx \int_0^T dt\, B_i(x,t)\delta(r - x\cos\theta - t\sin\theta)$$

where L is the length (in pixels) of the reference line (i.e. the height of the ST plot bin image), T is the number of frames in the bin (i.e. the width of the ST plot bin), r is the distance along the transformed spatial dimension of the RT image, and B_i is the i^{th} ST

plot bin. The RT was computed using the built-in 'radon' function of the Image Processing Toolbox in Matlab.

When the projection angle is perpendicular to the streak orientation, the resulting RT projection will contain peaks that correspond to each streak in the input image (Figure 4.7C). The orientation of the streaks in the original ST plot image can therefore be determined by finding the projection angle with the most prominent peaks and troughs. A particularly effective approach is to calculate the variance of the derivative of the RT for each projection angle. For a given projection angle, the derivative of the RT projection is approximated by

$$\frac{\partial R_i}{\partial r}(r,\theta) = \frac{[R_i(r+\Delta r,\theta) - R_i(r,\theta)]}{\Delta r}$$

where Δr is the spatial distance between adjacent values in the RT (always equal to 1px). The average of the derivative is thus

$$\frac{\partial \bar{R}_i(\theta)}{\partial r} = \frac{1}{L}\int_0^L \frac{\partial R_i(r,\theta)}{\partial r}dr = \frac{R_i(L,\theta) - R_i(0,\theta)}{L}$$

Finally, the variance is calculated for $\frac{\partial R_i}{\partial r}(r,\theta)$ for each θ:

$$\sigma^2_{\frac{\partial R_i}{\partial r}}(\theta) = \frac{1}{L}\int_0^L \left(\frac{\partial R_i}{\partial r}(r,\theta) - \frac{\partial \bar{R}_i(\theta)}{\partial r}\right)^2 dr$$

θ_{max} is defined here as the projection angle which results in the maximum variance in the above equation. This projection angle is perpendicular to the streak orientation in the ST plot image (Figure 4.7C). Thus θ_{max} is converted to a velocity (px/fr), U by

$$U = \tan(\theta_{max} - 90°)$$

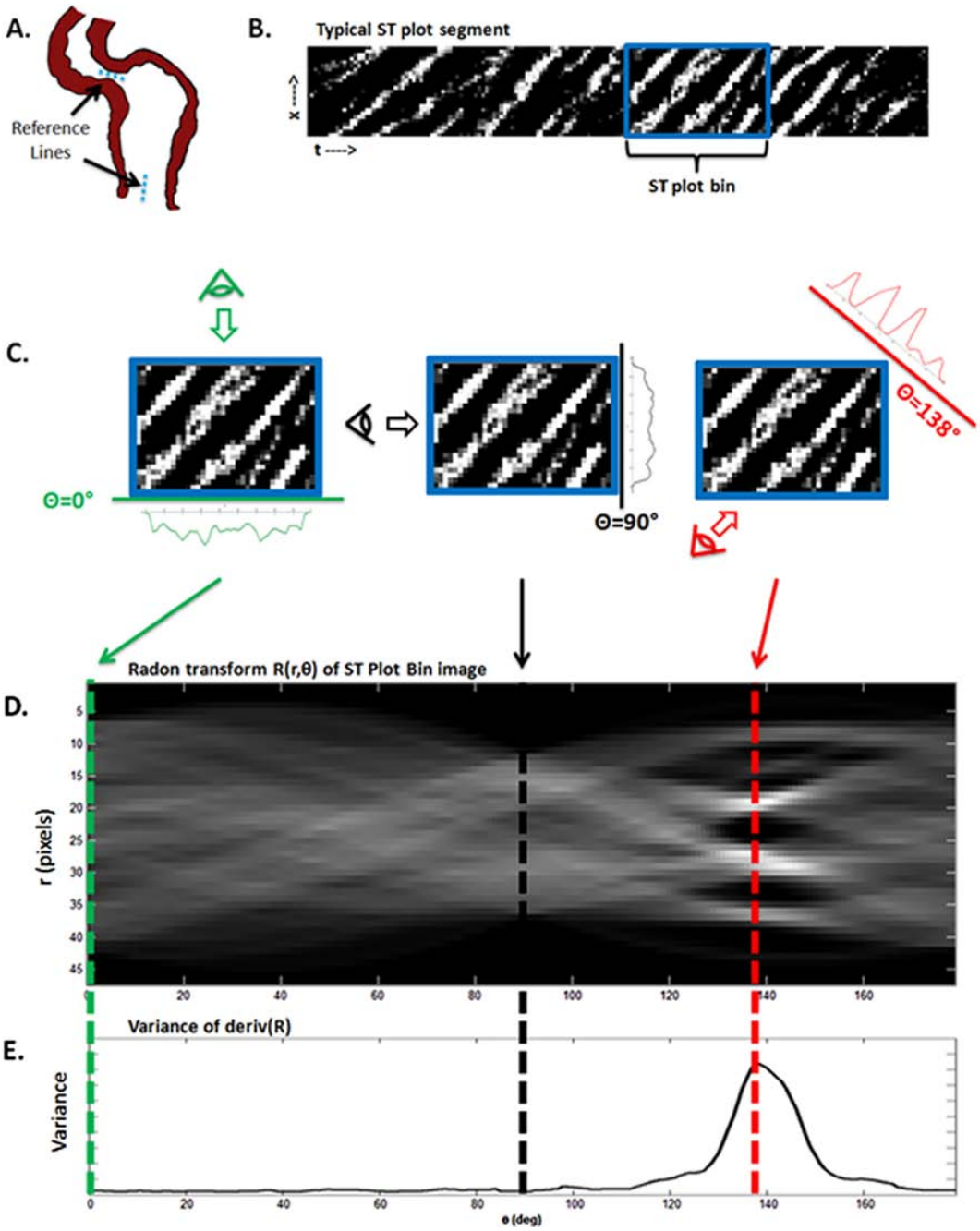

Figure 4.7 ST Plot Analysis with Radon Transforms

Part (A) shows a cartoon of an embryonic heart. ST plot reference lines are placed as shown at the atrial inlet and AVJ. A sample section of a typical ST plot is shown in (B). The ST plot must be analyzed in smaller sections, called bins. One such bin is outlined in (B). Part (C) shows the Radon transform analysis at 0°, 90°, and 138°. The projection of this bin is summed along each of these projection angles to produce a corresponding plot (C, colored plots). When the projection angle matches the streak angle (138° in this case), the resulting plot contains prominent peaks (red plot in C). A complete Radon transform contains an analysis of the ST plot bin from every angle, where Radon transform values are represented by intensity, as seen in (D). Part (E) shows a plot of the Radon transform variance for each angle. The projection angle with the highest variance is perpendicular to the streak angle in the ST plot. The velocity (pixels/frame) is then tan(Peak_variance_angle–90°).

4.12 Signal to Noise of Velocity

The process for determining velocity results in a calculated angle based upon the highest variance. After image processing, the noise associated with camera vibration, the camera sensor, and deep circulating blood cells is all that remains in the static areas of the image sequence. The signal to noise ratio was determined by comparing the noise amplitude within static areas of the sequence to the signal from blood movement. The signal to noise ratio ranged between 9 and 50dB. In order to eliminate noise-based data points, a variance threshold was set for each data set. Data points that resulted in variance amplitudes below this threshold were removed.

4.13 Measurement of Cardiac Lumen Diameter

The cross sectional area of the heart inlet must be estimated before the blood flow rate can be calculated. Data was acquired as two dimensional images on a single focal plane which necessitates the use of assumptions. In this case, the assumption is that the atrial orifice is approximately circular in profile. Thus the cross sectional area can be estimated by measuring the diameter from the images. However, this is not as straight forward as it may appear; the profile coefficient was determined based on the speed of blood cells across the width of the atrium, yet blood cells tend to flow more toward the center of vessels and not completely up against the wall. To be consistent, the visible flow width (i.e. the span of the flow which is occupied by blood cells) was used rather than the span from one endocardial wall to another. There is another important reason

that this technique was used: if the focal plane is slightly off-center at the inlet, the inlet walls may appear to be closer together than they actually are. Yet out of plane blood cells can still be detected—even when their boundaries are beyond the apparent inlet wall boundary. All things considered, I believe that the visible flow width is a more accurate measurement of diameter than the apparent wall-to-wall inlet width.

To actually make the diameter measurement, ST plots were used. In this case, the reference line was oriented perpendicular to the flow rather than parallel. As the heart wall contracts and expands, blood is funneled across the reference line, and cells are visible as circles or ovals in the resulting ST plot (Figure 4.8). Matlab was used in order to set boundary points along the flow boundary in the ST plot. The number of points could be chosen as necessary to accurately define the boundary. Once points were set, intermediate boundary locations could be interpolated. Functions were created to overlay the tracked boundary points on top of the animated image sequence, which was quite useful in ensuring that the flow boundary was tracked accurately.

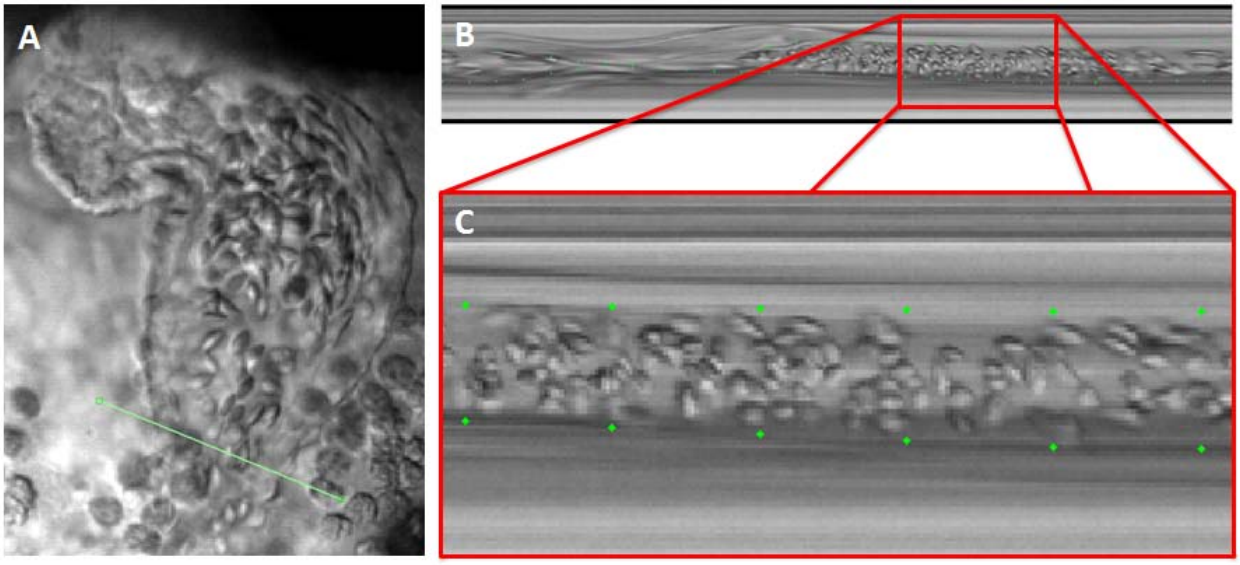

Figure 4.8 Perpendicular ST Plots for Diameter Measurement
To measure diameter, reference lines are placed across the atrial inlet perpendicular to the blood flow (A). ST plots are created (B) in which the flow boundary is tracked by placement of boundary nodes (shown in green) (C).

4.14 Estimation of Derived Parameters

Volume-based parameters cannot be measured directly from 2D image sequences and were instead estimated based upon the measured velocity and diameter. As mentioned, the analysis developed here assumes a circular cross-sectional area for the atrial inlet. This assumption has been previously utilized in other zebrafish studies [69, 95]. The instantaneous flow rate through each orifice was estimated by multiplying the flow velocity by the cross-sectional area of the opening,

$$Q(t) = U(t)\pi\frac{d(t)^2}{4}$$

where U(t) is the average blood velocity and *d*(t) is the lumen diameter. The differential volume, ΔV, is calculated by multiplying the instantaneous flow rate by the temporal length of the bin, Δt:

$$\Delta V = Q(t)\Delta t$$

Accumulated volume is calculated by summing the differential volumes:

$$V_{ac}(t) = \sum_{i=0}^{i=t} \Delta V(i) = \int_{o}^{t} Q(\tau) d\tau$$

Stroke volume (SV) was estimated by taking the accumulated volume across one complete cardiac cycle; the final volume at the end of the cycle reflects the amount of blood pumped per stroke. It should be noted that this corresponds to the *forward stroke volume* used in clinical practice. The standard stroke volume values used in clinical practice are measured by subtracting the end systolic volume from the end diastolic volume and do not account for whether flow is in the forward or reverse direction. In the case of the embryonic heart, it is more effective to measure the forward stroke volume since all measurements are made at a single orifice. Cardiac output (CO) was estimated by multiplying the stroke volume by the heart rate (HR):

$$CO = HR \times SV$$

The regurgitant fraction (RF) is defined as the ratio of retrograde flow to the total flow through an orifice.

$$RF = \frac{V^-}{V^+}$$

where V^+ and V^- are volume flowing in the positive and negative directions, respectively. RF can be defined in other ways, such as:

$$RF = \frac{V^-}{V^+ + V^-}$$

Where this may make sense in a clinical setting with an adult heart, the first definition makes more intuitive sense when applied at a single orifice in the embryonic heart. RF

can be thought of as the amount of forward-pumped blood in each cycle which eventually flows backward across the orifice. Thus if the orifice/valve was entirely ineffective, and all of the blood which was pumped through it flowed back into the heart on each cycle, then RF would equal one.

4.15 Automated Calculation of Heart Rate

Calculation of heart rate was also performed using ST plots in a method which has, to my knowledge, not been previously used. A reference line was placed at the outer edge of a wall boundary, and an ST plot was created which spanned the entire image sequence (Figure 4.9). This ST plot was divided into bins of equal size. Each successive bin was then subtracted from the previous bin. The total value from all subtracted bins was then added to achieve a single value which describes bin-to-bin variability. This process was then repeated for bins of the next incremental length. When the bin length matches the cycle length, the final variability value will be very near zero. Thus the bin length with the smallest variability value was used to define cycle length.

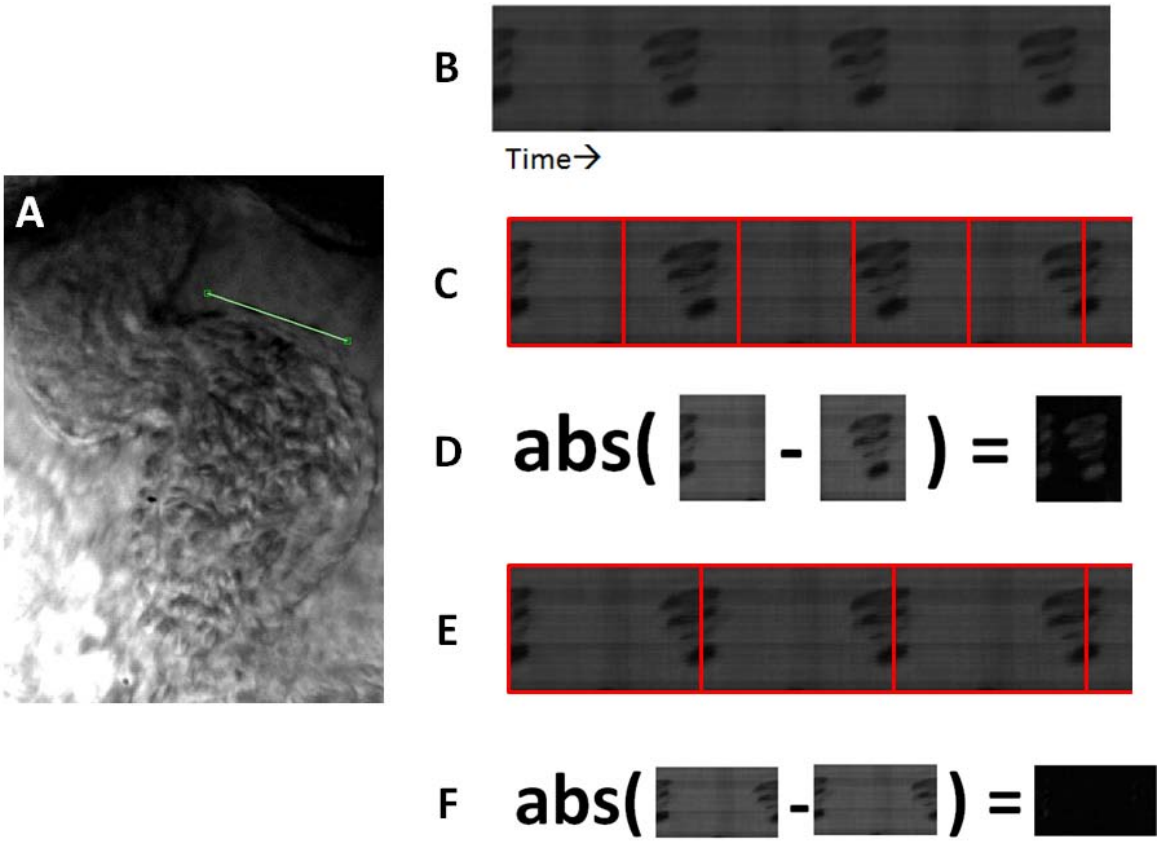

Figure 4.9 Automated Heart Rate Determination
Heart rate was determined automatically using ST plots. Reference lines were placed near the extreme wall boundary of the heart (A). This resulted in an ST plot with a repeating pattern associated with the cyclical wall movement (B). The ST plot was divided into bins of increasing length (C and E). Successive bins at each length were then subtracted (D and F). When bin size matches cycle length (F), the resulting value is near zero (entirely black). Otherwise, the result is a positive value which increases as cycles become decreasingly synchronized. Note that only two bins are subtracted here in order to save space—the algorithm actually subtracts all bins when performing the calculation.

4.16 Test Experiment Setup

This methodology was published in the Journal of Biomechanical Engineering [101]. In the publication, a simple test experiment was performed to demonstrate the ability of the methodology to detect changes in heart function. A 55 hpf zebrafish embryo was used in three test cases: 1) normal heart function; 2) heart function after cooling the embryo and slowing the heart rate; and 3) heart function after adding a high dose of anesthetic

(tricaine). Heart rate was allowed to recover between cases 2 and 3. Table 1 summarizes the results for each experimental case.

Table 1. Results from Methods Demo Experiment

	Normal	Cooled	Anesthetized	Units
HR	105	64	78	bpm
SV	0.29	0.24	0.05	nL
CO	30.7	15.4	3.6	nL/min
RF at Inlet	0.04	0.02	0.43	-
RF at AVJ	0.14	0.25	0.48	-

In this demo experiment, analysis was applied at both the atrial inlet and the atrioventricular canal (also called the AV canal, AVC, atrioventricular junction, or AVJ). The AV canal was not evaluated in later experiments because it is more difficult to analyze and yields less reliable results. Additionally, since fluid volume is ultimately conserved, the flow rates into and out of the atrium must be identical. However, analysis of the AV canal does yield useful information in that the AV canal has its own value for regurgitant fraction.

4.17 Test Experiment Results

After cooling, the heart rate decreased by 39%, from 105 beats per minute (bpm) to 64 bpm. The anesthetic decreased the heart rate 26%, to 78 bpm. Stroke volume decreased slightly in the cooled case, and decreased drastically in the anesthetized

case. Cardiac output was reduced by 47% in the cooled case and 89% in the anesthetized case. RFs were very similar between normal and cooled, but were much higher in the anesthetized case. In all three cases, the RF was higher at the AVJ than at the atrial inlet.

Velocity and diameter plots are shown in Figure 4.10. The derived flow rate and volume plots for each of the experimental cases are shown in Figure 4.11. Heart rate varied between each of the three cases and time was normalized such that a single cardiac cycle spanned from 0 to 1. This normalized time will be referred to as (NT). The beginning of the cardiac cycle was defined as the moment when the endocardial wall at the inlet began to contract at the start of atrial systole.

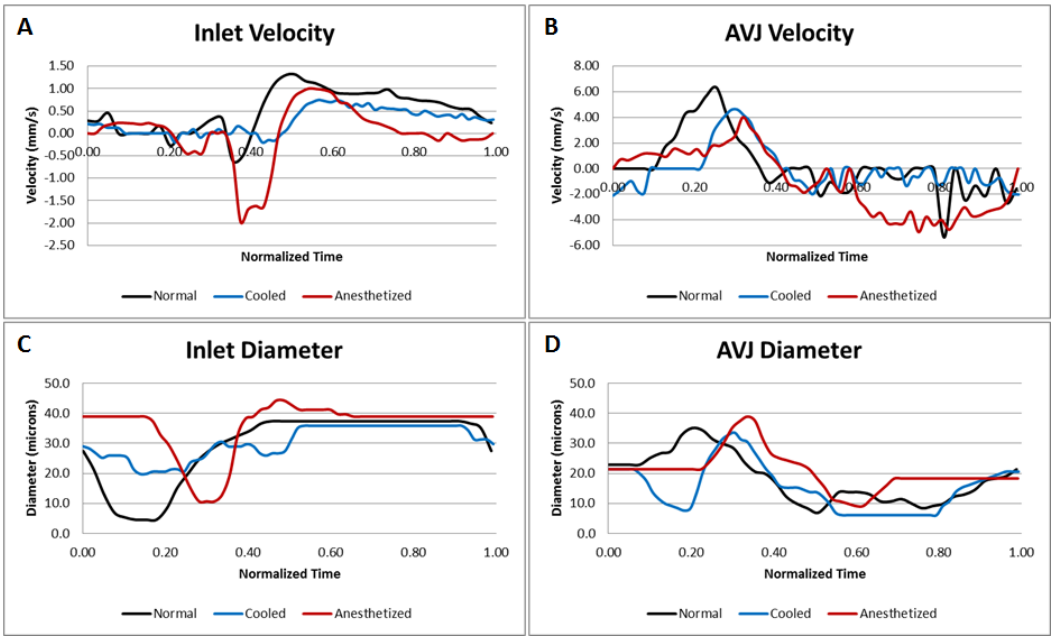

Figure 4.10 Results of Demo Experiment (Velocity and Diameter)
Plots (A) and (B) show the blood velocity while (C) and (D) show the orifice diameter. These values were used to calculate the flow rate and accumulated volume

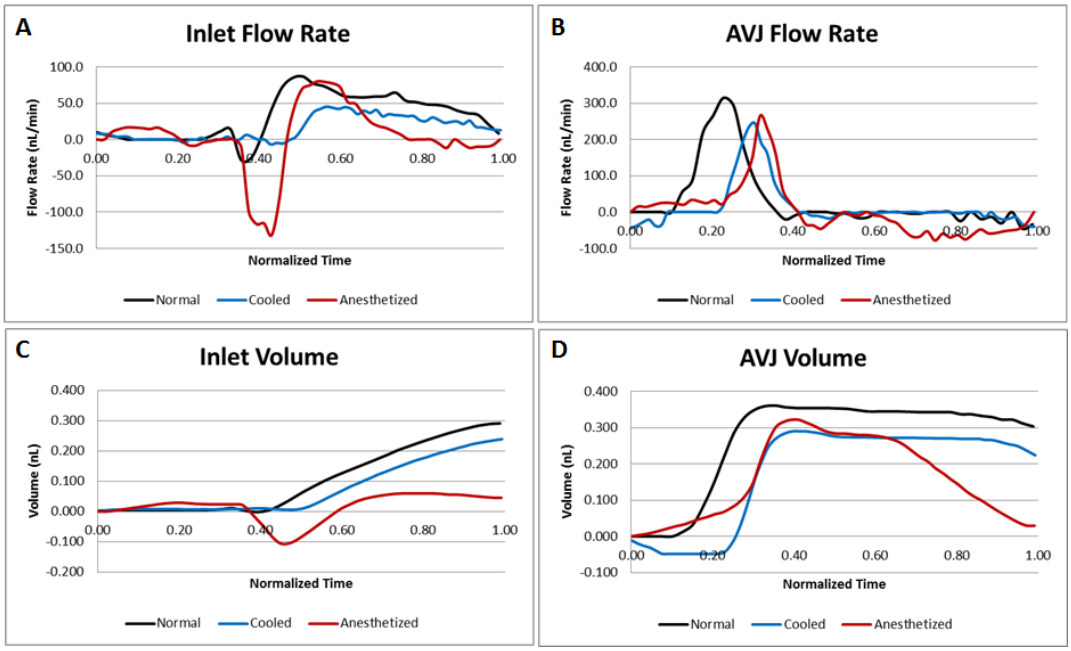

Figure 4.11. Results of Demo Experiment (Flow Rate and Accumulated Volume)
Plots (A) and (B) show the flow rate while (C) and (D) show the accumulated volume through each of the orifices. The similarity in function can easily be seen between normal and cooled cases, whereas the anesthetized case has a dramatic increase in retrograde flow which results in a drastically lower stroke volume.

The plots in all three cases have similar overall trends. For most of atrial systole (0 to ~0.4NT in the normal case, Figure 4.11A) there is very little blood flow through the inlet. There is a brief period of retrograde flow prior to atrial diastole (~0.4 to 1NT in the normal case) which is immediately followed by a large forward flow as atrial diastole begins (Figure 4.11A). Flow rate quickly reaches a peak and then steadily decreases throughout the remainder of the cardiac cycle. At the AVJ, forward systolic flow begins within 0.1NT. The flow rate quickly reaches a maximum and then quickly drops to zero by 0.4NT (Figure 4.11B). For the remainder of the cardiac cycle, regurgitant flow occurs through the AVJ.

The normal and cooled cases' flow rate and volume plots differ mainly in that the cooled case experiences lower flow rate magnitudes and requires a shorter fraction of the cycle to expel blood through the AVJ (Figure 4.11B). The anesthetized case is different in several respects. The regurgitant flow, which occurs prior to atrial diastole at the inlet, begins earlier than in the other cases (0.2NT vs. 0.34Nt in the normal case; Figure 4.11A) and has a much greater peak value (~109nL/min vs. ~29nL/min in the normal case). Atrial diastole lasts a much shorter amount of time (~0.23NT vs. ~0.50NT in the normal case). At the AVJ, the anesthetized heart also has a drastically increased retrograde flow volume compared to the normal case (Figure 4.11 B and D). The combination of large regurgitant volume and shorter duration of anterograde flow results in a much smaller stroke volume.

4.18 Test Experiment Discussion

This experiment provided a simple and effective means of showing the methodology's capability to distinguish the difference in heart function in various cases. The function of a heart which is slowed by cooling should not change substantially. On the other hand, a heart which is slowed by an anesthetic acting directly to decrease the ability for cardiomyocytes to contract should be seriously compromised. Not only did the results agree entirely with what was expected from each case, but they also provided some useful insight into what caused the decreased function—in this case a large increase in retrograde fraction in the anesthetized case. What follows is a brief overview of the hemodynamics observed in the experiment.

At the beginning of atrial systole, a contraction wave originates upstream of the inlet and forces blood forward through the AVJ. In the normal and cooled cases, the endocardial walls relax and expand at the inlet at ~0.25NT, which allows retrograde flow through the inlet until the end of systole at ~0.4NT. Tricaine appears to change the timing of the contraction wave, which is a critical factor in determining the amount of regurgitant flow that will occur. This relaxation occurs at ~0.21NT in the anesthetized case, well before the end of atrial systole (Figure 4.11A). Because the atrium is under high pressure during systole, this allows a markedly increased amount of regurgitant flow through the inlet. A very similar trend happens at the AVJ; although ventricular function is not analyzed in this work, the ventricle begins contracting very soon after the completion of atrial systole. The AVJ normally remains contracted throughout ventricular systole and reduces regurgitant flow. In the anesthetized case however, the AVJ walls do not contract as fully, allowing substantially more retrograde flow (average AVJ diameter is ~16 microns vs. ~12 microns in the normal case, data not shown). This supports the idea that the developing, pre-leaflet conformation of the AVJ plays an active role in the prevention of backflow. The results indicate that high doses of tricaine cause severe regurgitation in the atrium due to a combination of weaker contractions and altered contraction timing. The results also indicate that heart function is not significantly affected by the slower heart rate associated with reduced environmental temperature; flow rates were reduced but occurred over the much longer cardiac cycles, resulting in comparable stroke volumes.

Both the inlet and AVJ reach their respective maximum diameter and maximum anterograde blood velocity simultaneously (Figure 4.10 A and B). They likewise reach their respective minimum diameter and maximum retrograde blood velocity simultaneously. The maximum inlet blood velocities (~1.4mm/s) are significantly slower than those at the AVJ (~6.3mm/s). These velocity magnitudes are comparable to previous studies [69]. Despite the lower inlet velocities, the inlet diameter is significantly larger and, following the laws of conservation, ultimately the same amount of blood flows through both orifices. Based on these estimates, the Reynolds number is ~0.04 and the Womerseley number is ~0.02, indicating that the flow is highly viscous with no unsteady effects.

The results presented here are based on a single zebrafish embryo and are meant to act as a simple demonstration of the methodology. Given this very small sample size, conclusive statements cannot be made about how the embryonic heart works. However, it was demonstrated that several important parameters describing cardiac function can be estimated from a single high-speed image sequence. The resulting plots can provide insightful information on how the heart functions.

4.19 Advantages of Calculations based on Flow Rate

Multiple studies have estimated stroke volume and ejection fraction by comparing the end systolic volume (ESV) to the end diastolic volume (EDV) [69, 102]. ESV and EDV can be estimated by approximating the chamber as a prolate spheroid or by tracing the chamber perimeter and integrating about the central axis. In theory, the difference

between the end systolic and diastolic volumes should directly yield the stroke volume. Although this is true for hearts that contract in a single, constricting motion (as seen in a mature heart), it is not true for developmental stages that precede valve development. Circulation begins between 26 and 30 hpf. At this stage, the heart is in a primitive tube formation, and contraction waves propagate from inlet to outlet. Because blood is pushed ahead of each acute wave, the instantaneous heart volume provides little indication of the stroke volume; a single wave can theoretically push the entire blood volume from the tube without constricting more than a fraction of the tube at any given instant. In this case, a stroke volume based upon ESV and EDV would be greatly underestimated. As the heart begins to loop and form chambers, the distinct contraction waves slowly give way to more subtle and independent chamber contractions. In order to accurately estimate the stroke volume and cardiac output in these early stages of development, it is necessary to consider the actual blood volume entering and exiting a control volume. This technique has been previously applied by considering a control volume along the dorsal aorta, downstream of the heart [70, 95]. The volume flux can be calculated by simply multiplying the blood velocity by the cross-sectional area of the aorta. The limitation of considering a control volume at the aorta is that some parameters of heart functionality (valve efficiency, heart wall kinematics and gross cardiac morphology) cannot be measured directly. Here, the same principles are applied, but the atrium is used as a control volume.

4.20 Introduction to Methodology Validation and Modifications

There are many aspects of the methodology which can be optimized to improve the accuracy of the results. I have addressed what I believe to be the key areas which may lead to error. What follows are the results of several validations and optimizations that were performed on the methodology.

4.21 Effect of Bin Size

ST plots capture changing velocity over time, which is seen as a change in streak angle across the ST plots. In order to calculate the velocity at particular points in time, it is necessary to extract localized sections (bins) of the ST plot for analysis. The bin width can be an important factor in the accuracy of the velocity calculation. Bins must be small enough to capture the instantaneous velocity at the given point in time, while also remaining large enough to determine the slope of lines in the ST plot. To find an appropriate bin size, an ST plot section with changing velocity was selected (Figure 4.12).

The central portion of the ST plot was measured manually as a benchmark and the slope was calculated. Next, bins of varying widths, each centered about the same frame, were analyzed computationally. The resulting variance plots were compared for accuracy and precision. A relatively wide range of bin values (~15-30 frames) produced similarly accurate results. These yielded prominent variance peaks which coincided with manual measurements. Larger bins became increasingly less accurate, as the local

velocity streaks eventually became overpowered by the surrounding velocity streaks. Although a smaller bin size guarantees that only the local velocity is considered in calculations, it also decreases the amount of data in each bin. As bin widths decreased, variance plots became increasingly less precise and less accurate. With fewer pixels to integrate, the Radon transform became influenced by minor streak variations and background noise. The resulting variance was reduced, and a greater range of projection angles was able to yield similar results. The true line orientation was consequently difficult to determine. In this case a moderate bin size near 21 appears to be ideal.

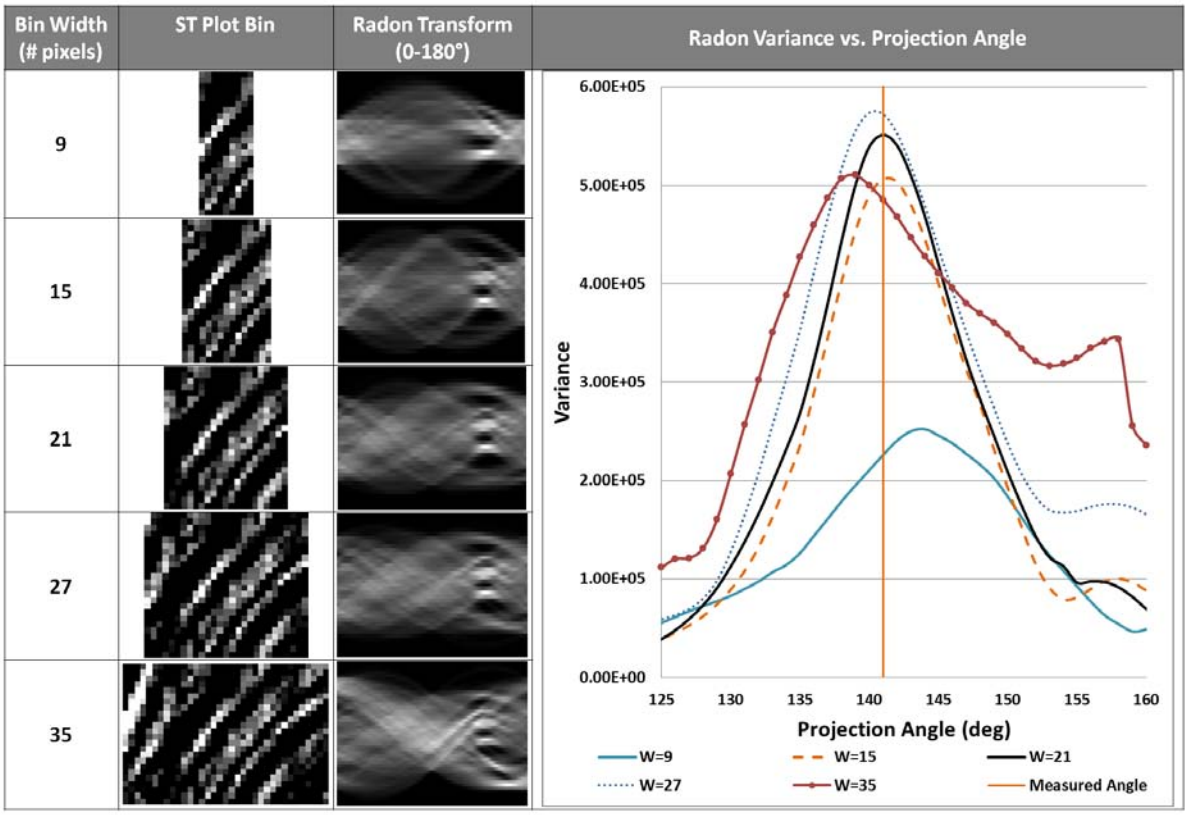

Figure 4.12 Bin Size Optimization
Bin size was optimized based on an ST plot segment with changing velocity. The local ST plot streak angle was manually measured as a baseline. Bin size was varied and results were compared to the baseline. Results are shown (from left to right) of the ST plot bin, the resulting Radon transform, and the variance of the derivative of the intensity of the Radon transform. 'W' is the width of the the averaging span (in frames).

4.22 Effect of Averaging Span

As described previously (Figure 4.4), blood cell movement is isolated by subtracting an averaged image from each frame. This image is created by averaging the intensities across multiple frames, and the width of this averaging span can affect the accuracy of the blood velocity calculations. Increasing the span width allows more movement to be detected, since a wider averaging span captures the movement between a larger number frames. However, a wider averaging span can also result in the overlap of adjacent cell signals. An optimal span width yields independent, well-defined ST plot streaks that are associated with features on the moving cells. To find the optimum averaging span, results were compared from a range of spans at two velocities (Figure 4.13). At low to moderate velocities, as seen through the majority of the cardiac cycle, cells move only a small amount between frames. In this case, a wider span captures more motion and strengthens the signal; the resulting variance peaks become higher and stay accurate as the span width increases. At peak velocities (as seen during regurgitation through the AVJ), cells move several pixels per frame, which is fully captured with a single-frame averaging span. As the averaging span increases, movement from adjacent cells can be averaged together. This reduces the signal from individual cells and can result in significant error. This error is quite significant in the six-frame averaging span at high velocities. The cardiac cycle was broken into velocity-based segments and each segment was analyzed with an appropriate averaging span.

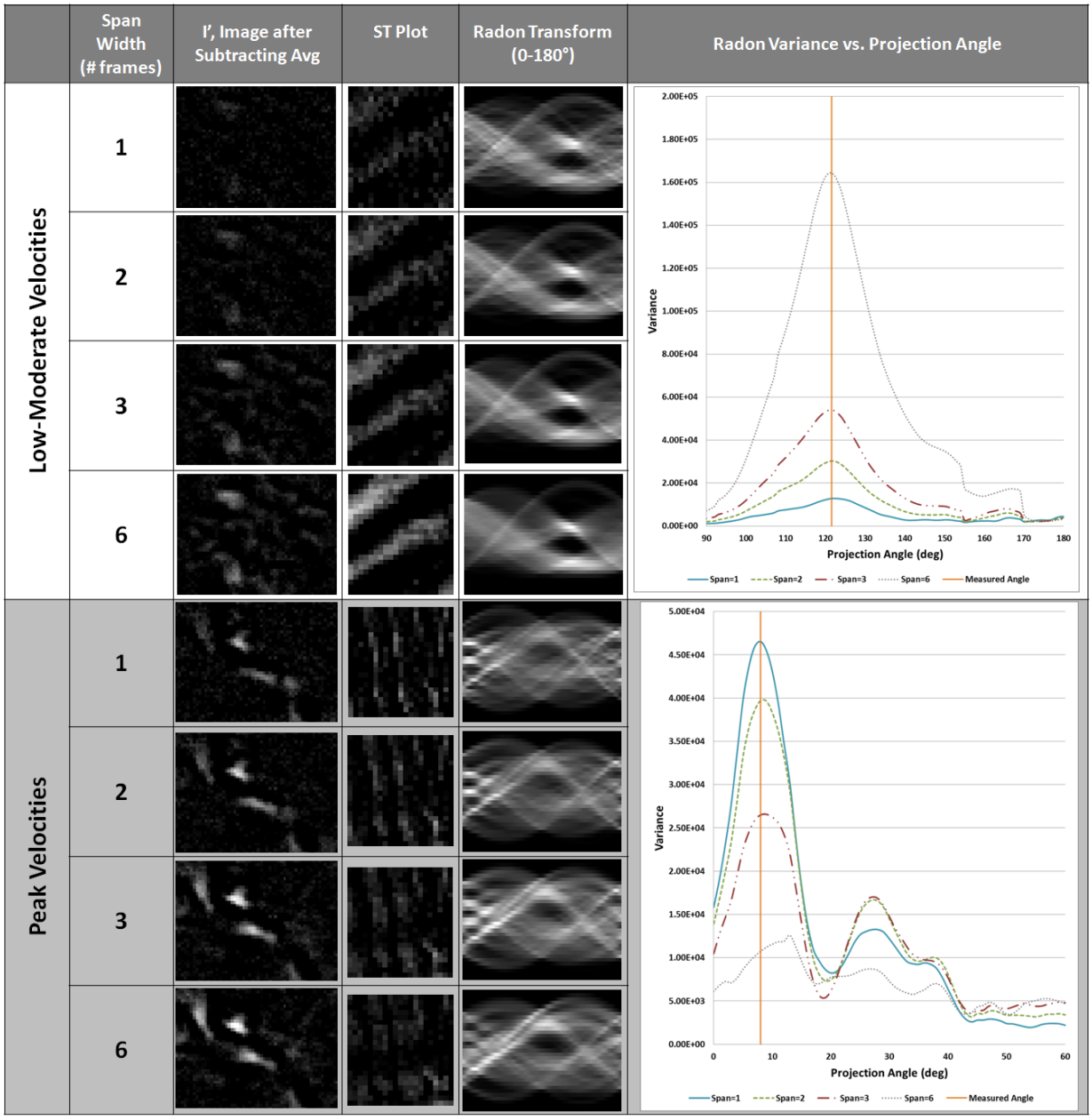

Figure 4.13 Averaging Span Optimization
Span size was optimized at low-moderate velocities (top) and peak velocities (bottom). Span size was varied and results were shown of (from left to right) the processed image, the resulting ST plot, the resulting Radon transform, and the variance of the derivative of the intensity of the Radon transform.

4.23 Reference Line Orientation Error

Because the blood velocity calculation relies on the movement of blood cells along the reference line, there will be an underestimation of blood velocity in the event that the reference line is not perfectly parallel to the blood flow. Figure 4.14 shows the velocity error associated with reference line orientation error. The plot shows that even when reference lines are misaligned from flow by 20° there is only a 6% error in velocity calculation. Realistically, reference line angle error should not be more than 10° (velocity error less than 2%) if an honest effort is made to keep it accurate.

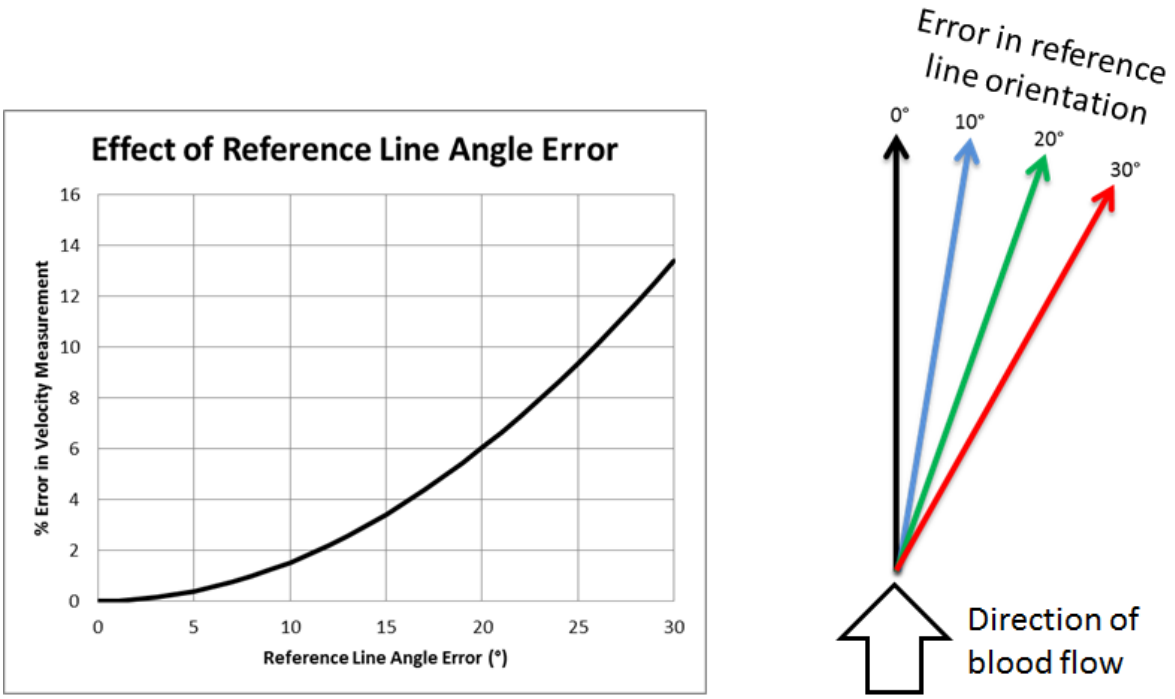

Figure 4.14 Reference Line Orientation Error
The above plot shows the error in velocity calculation associated with error in reference line orientation. The diagram on the right shows various reference line orientations with respect to a vertical blood flow direction. It should easily be possible to manually position a reference line within 10° of the true flow direction. At a 10° reference line orientation error, the velocity error is less than 2%. Even at 20°, the velocity error remains well under 10%.

4.24 Streak Angle Determination Error

Another source of error is in the extraction of streak angle from the ST plot. If the streak angle is miscalculated by an increment (e.g. 1° or 0.5°) then the calculated velocity will be off. The amount of error associated with incremental streak angle miscalculation is dependent upon the angle of the streak; the difference in velocity between 45° and 46° is much smaller than the difference in velocity between 88° and 89° because the associated velocity goes to infinity at a streak angle of 90°. As shown in Figure 4.15, a 1° miscalculation of streak angle results in an error of under 10% when the streak angle remains below 80°. Beyond 80° the error quickly climbs—20% error is reached at 84°. Note that the error percentage also skyrockets when the streak angle goes below 10°. This latter case does not actually matter because the velocity value is falling to zero; although error percentage may technically rise when comparing a low decimal to a decimal approaching zero, both values for velocity will ultimately be very close to zero. The maximum streak angle can be controlled by increasing the frame rate.

In terms of decreasing error in velocity calculation, a higher frame rate is always better. Given the limits of hard drive space, however, the ideal frame rate is one capable of keeping the blood velocity streak angle below approximately 80° while also retaining enough digital memory to record the desired number of cardiac cycles. A minimum of 6 cardiac cycles per sample was chosen, and this allowed for a frame rate of 1500 frames per second. At this frame rate, blood velocities can be measured as fast as 12.6 mm/s. Atrial inlet velocities only surpassed 7 mm/s in two instances, with a maximum of 11

mm/s. 1500 frames per second is therefore significantly faster than necessary in most cases and remains adequate in even the most extreme cases.

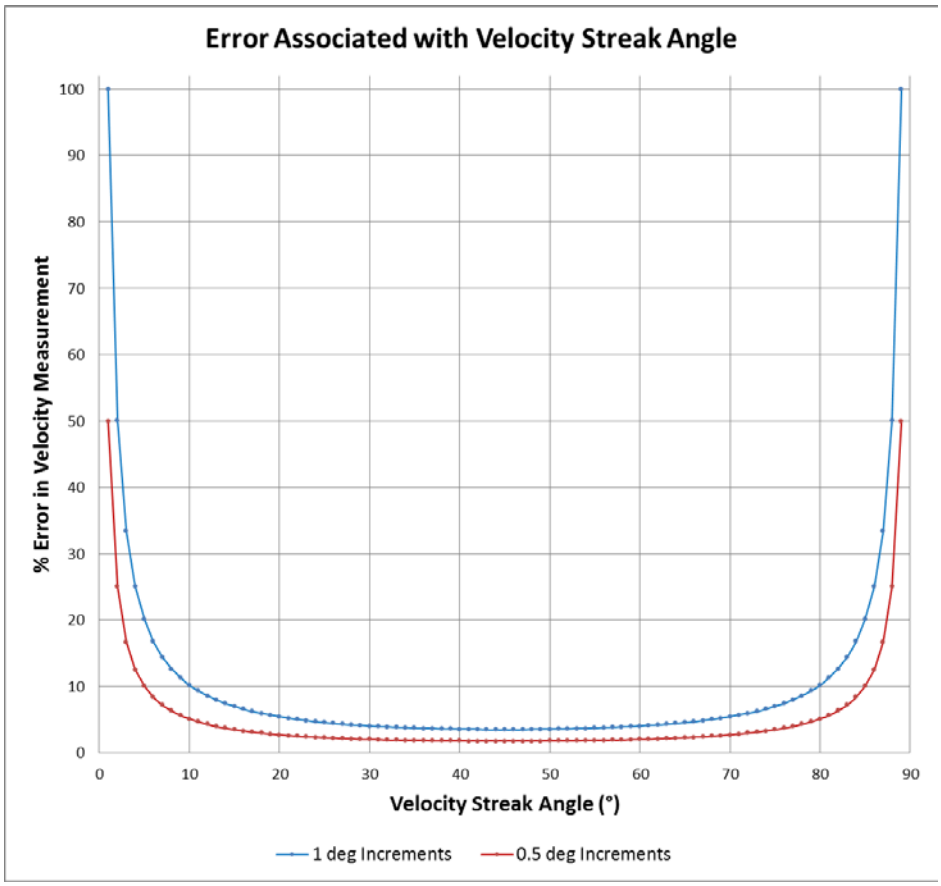

Figure 4.15 Streak Angle Error
The above plot shows the percentage of error in velocity calculation for varying values of ST plot streak angles. Velocity can be most accurately determined at streak angles of 45°. Error is dramatically increased at very shallow angles (less than 5°) and very steep angles (greater than 85°). ST plot streak angle is directly related to blood velocity and imaging frame rate. Error can be directly reduced by using smaller increments in the Radon transform analysis.

Another way to reduce streak angle error is to reduce the increment in which the angle is analyzed. The default settings for Radon transform creation in Matlab is a 1° angle increment. This increment can be decreased to create a finer resolution of possible angle values. In other words, cutting the angle increment in half can potentially cut the

error in half. This can only be of limited efficacy, however, because eventually a slightly altered Radon angle will remain within the exact same pixels of the analyzed bin. This can only be overcome by increasing the spatial resolution of the camera. Given the resolutions obtained at ~225X maximum magnification of the Olympus SZX12 stereomicroscope and the Photron FastCam SA3, it is unlikely that any significant gains in accuracy can be obtained below a 0.5° Radon increment.

4.25 Validation of Radon Streak Angle Measurement

Several validations were performed at various steps in the analysis process to ensure accuracy of the analysis. The first necessary validation was to ensure that streak angles were being accurately determined. Previous publications have extracted the streak angle by simply taking the variance of the raw Radon image [82]. The theory behind this technique is that the streak pattern will show up as a series of horizontal bands at the location in the Radon transform corresponding to the streak angle (Figure 4.16D at red dotted line). The alternating light and dark bands in this section creates a relatively high variance compared to non-matching angles where the Radon integration is more or less a constant intensity. This technique is very effective when there are many fine streaks in an image, and it worked well in some of the raw zebrafish data. However, there were many cases in which the calculated Radon angle was completely off (Figure 4.17A-C). It is obvious that the variance peak is highly biased to particular portions of the Radon transform—particularly at 0°, 90°, and 180°. At these angles, it is very common for the Radon transform image to transition abruptly from almost entirely black to almost entirely white. Since the variance is a measure of the distance of each data point from

the average, these black and white sections create an enormous variance—the average of the black and white sections is gray, so nearly all data points are as far from the average as possible.

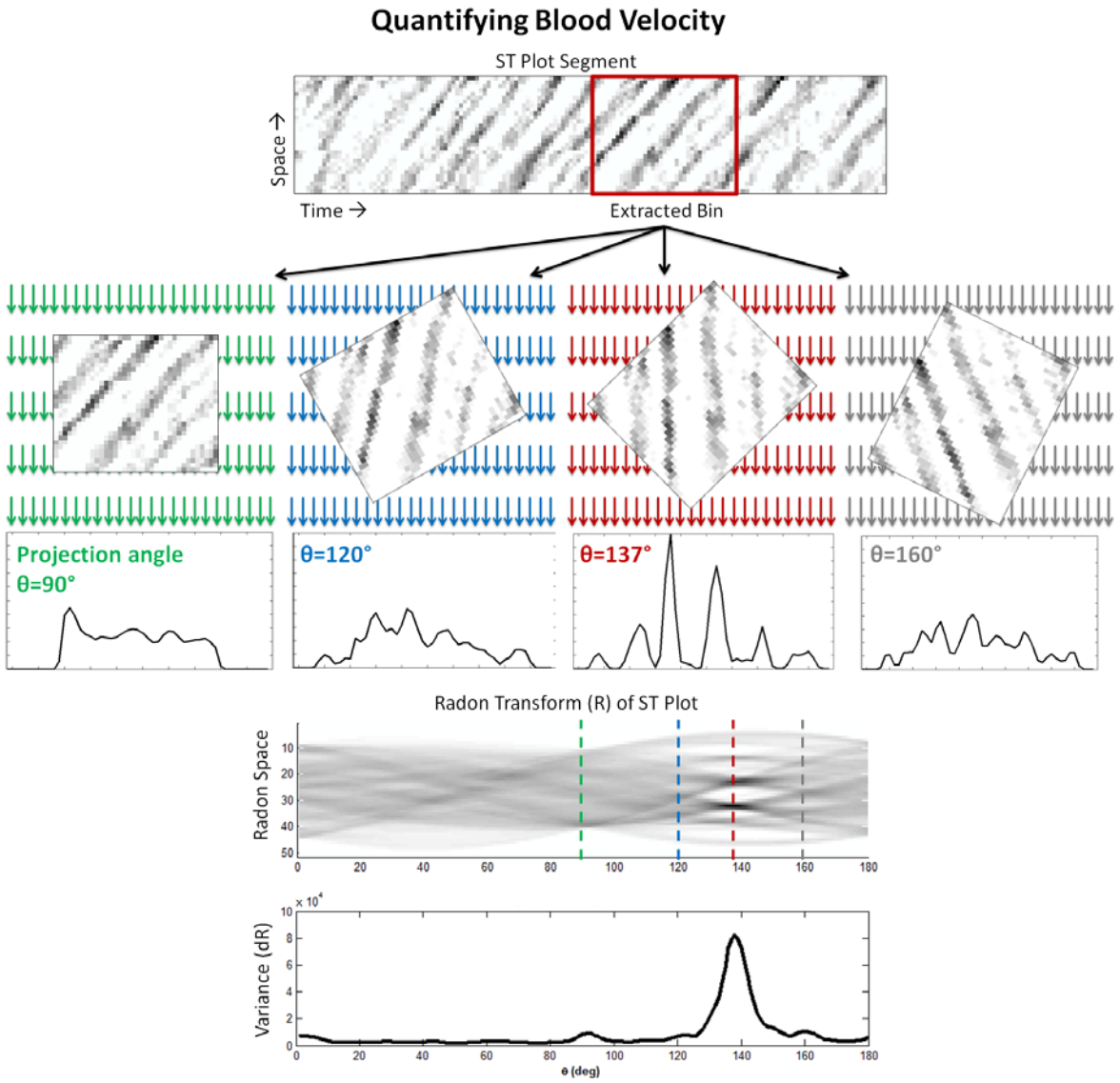

Figure 4.16 Creation of Radon Transforms (another example)
As an alternative to Figure 4.7, this figure again shows how a Radon transform is created. (A) shows an example ST plot with an outlined bin of interest. The Radon transform is created by combining the projection intensities across all angles. (B) shows four different angles with the resulting intensity values of their projections. Intense peaks are present when the projection angle matches the streak angle. In this case, the projection is the sum of the dark pixels along each vertical column. The final Radon transform is shown in (C), where each vertical dotted line corresponds to the four angles tested in (B). (D) shows the variance of the derivative of each column of the Radon transform in (C).

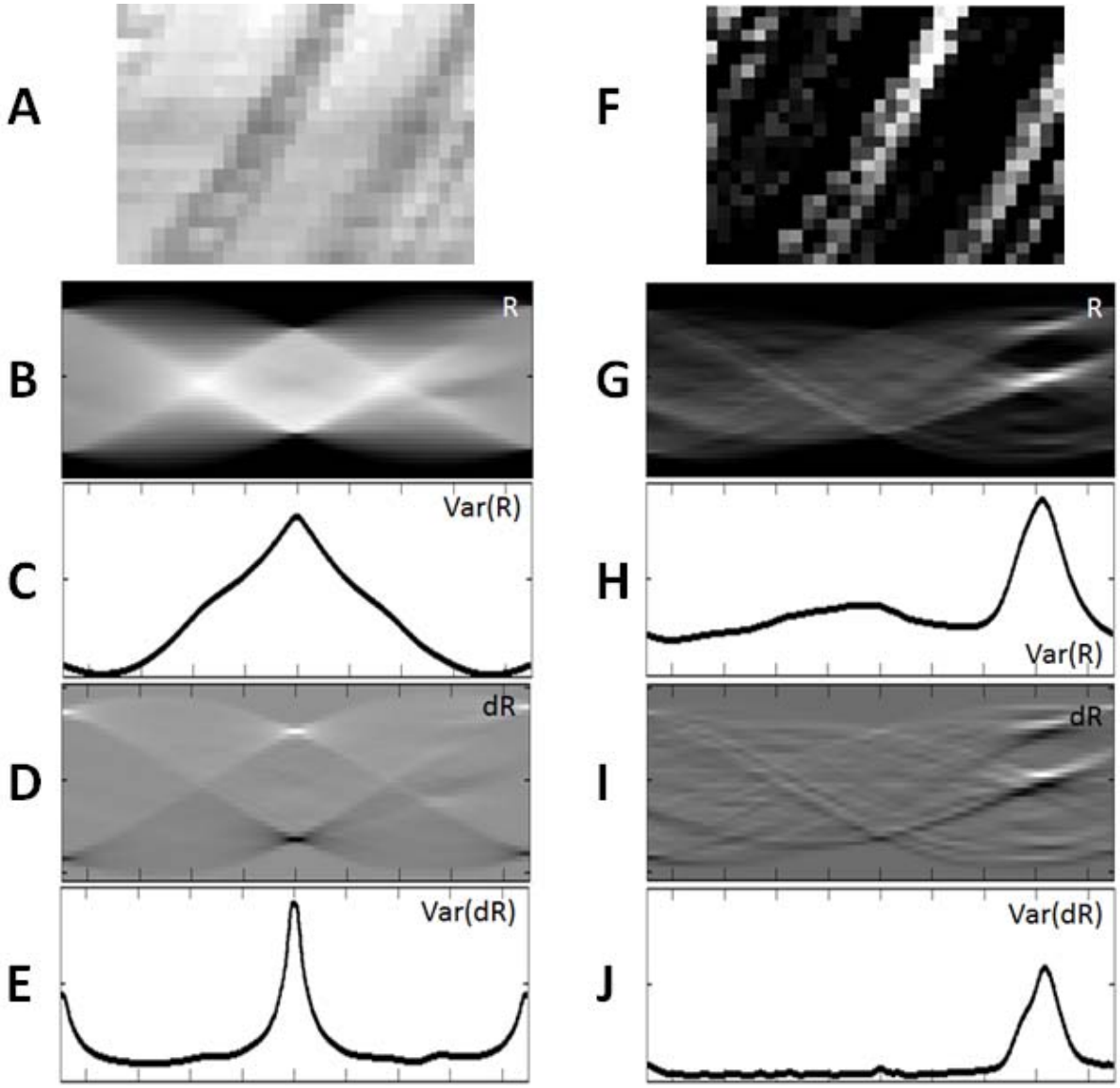

Figure 4.17 Radon Analysis Comparisons
(A) is a typical ST plot extracted from the raw image sequence. (B) is the resulting Radon transform in which streak angle banding is barely noticeable. (C) is the result from taking the variance of the Radon transform. There is a major peak at 90° (the x-axis center) with no peak associated with the actual streak angle. (D) is the derivative of the Radon transform. (E) is the result of taking the variance of the derivative of the Radon transform. There is a very prominent peak at 90°, moderate peaks at 0° and 180°, and a very small peak associated with the steak angle. (F) is the ST plot that results after subtracting the sliding average from each image. Streaks are significantly more prominent and there is significantly less background noise. (G) through (J) correspond to the same plots as (B) through (E). The variance plot in (H) of the Radon transform correctly identifies the streak angle. The variance plot in (J) of the derivative of the Radon transform also identifies the correct streak angle, but does so with better precision; incorrect angles generally have a much lower value than those from the raw Radon transform. This can make the difference between a correct and incorrect angle evaluation in less ideal situations.

To overcome this problem, two steps were taken. First and most importantly, the sliding average of pixel intensity was subtracted from each image as described above. This eliminates background artifacts that create false streaks in the ST plot and drastically improves results (Figure 4.17 F-H). In the majority of cases, this is all that is necessary to accurately determine the streak angle. However, I devised a second step which can increase the angle precision and occasionally prevents critical errors. The method involves taking the variance *of the spatial derivative* of the Radon transform. Thus the *change* in Radon transform intensity is evaluated rather than the intensity itself. This greatly reduces the background variance effects, as is apparent in comparing Figure 4.17 H and J. This method puts more emphasis on detecting the horizontal banding associated with the streak angle; streak angle banding creates several peaks and troughs in the derivative of the Radon transform and results in a high variance for the streak angle. At the previously problematic 0°, 90°, and 180° angles, the derivative results in a single peak (where black transitions to white) and a single trough (where white transitions back to black). This results in a relatively low value for variance.

4.26 Synthetic Datasets for Validation

In order to perform extensive validations on every aspect of the analysis process, I created several sets of synthetic data. This involved creating a Matlab program which created image sequences roughly mimicking those of actual data. Ellipses representing blood cells were drawn on a background image. Each ellipse could be set to a semi-random shape and size within a set range. Velocity of the ellipses could be chosen as either a constant or as a function of space and time. It was therefore possible to create

a wide variety of scenarios which could be validated based on theoretical values. The most extensive of these scenarios is shown in Figure 4.18.

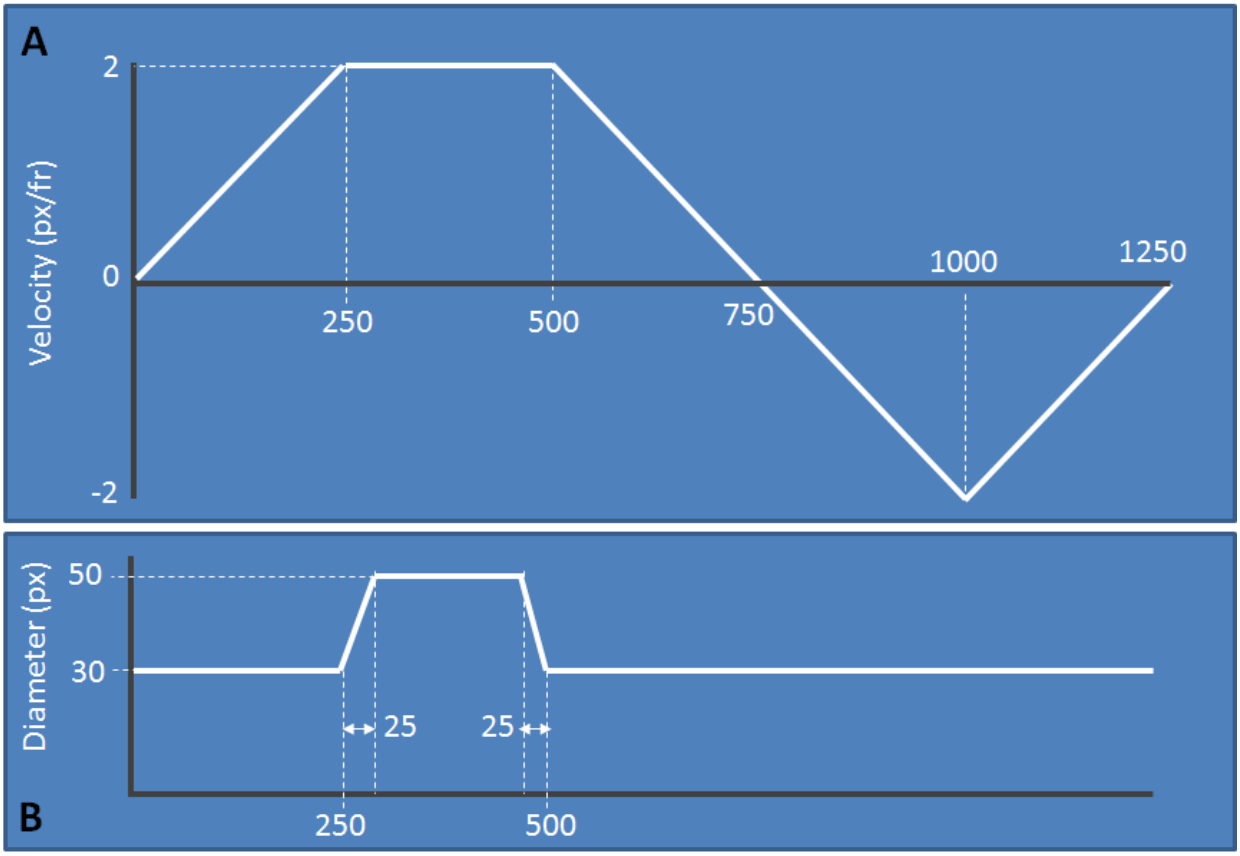

Figure 4.18 Synthetic Data Specification
A synthetic data set was created in which mock blood cells traveled at velocities following the function shown in (A). The diameter of flow was set to that shown in (B).

Velocity ranged from -2 to 2 pixels per frame and values for diameter were set to range from 30 to 50 pixels. Several cycles were created in which each cycle had a random and continuous distribution of ellipses. The resulting ST plot is shown in Figure 4.19B. This plot was analyzed using the same automated Radon analysis which would later be applied to all real data sets, and resulted in the plots shown in Figure 4.20. The resulting value of stroke volume (which is the end point of the analysis) was accurate to greater than 99%. This was an important validation which showed that the algorithms

responsible for creating ST plots, creating Radon transforms, interpreting Radon transforms, calculating velocities, converting diameters, linking diameter and velocity, calculating flow rate, and integrating flow rate to get stroke volume were all working exactly as desired.

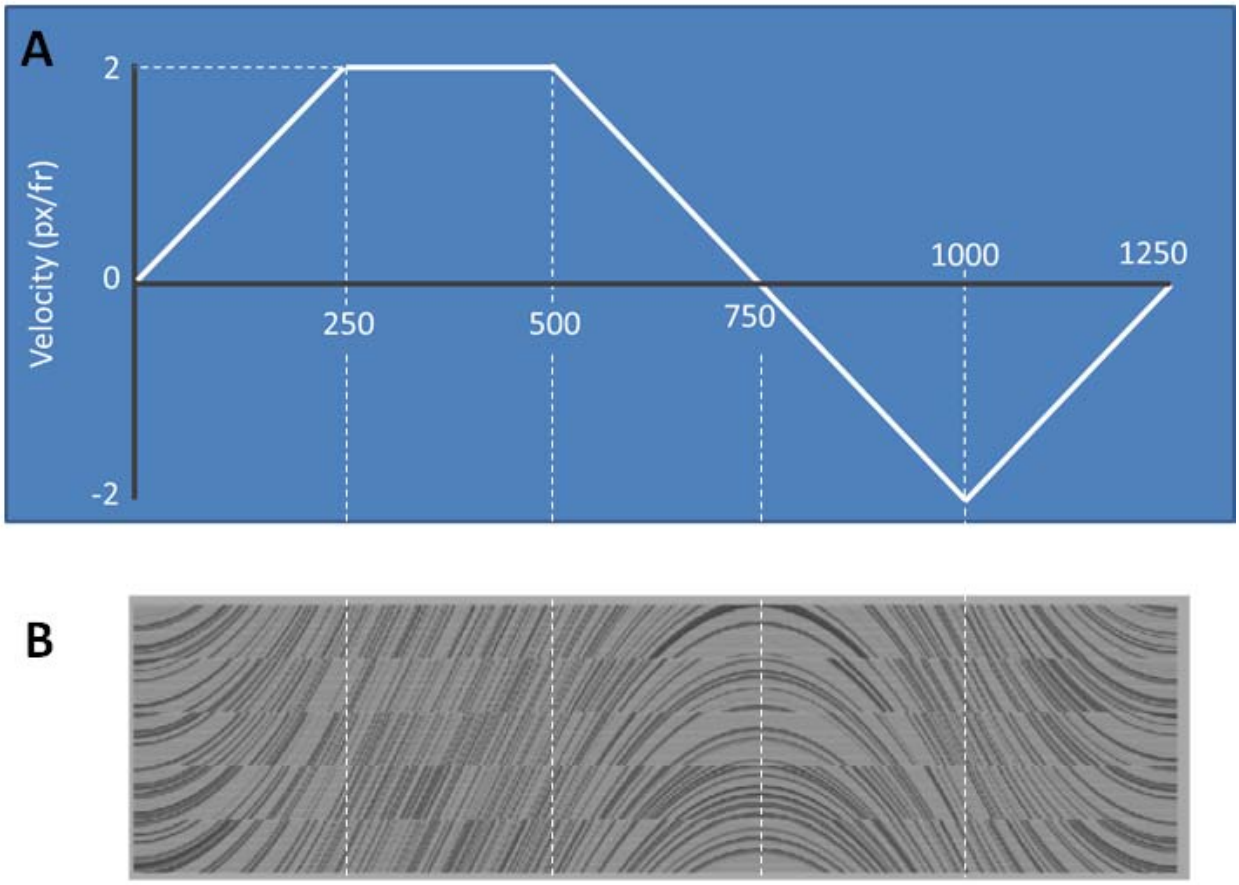

Figure 4.19 Synthetic Data and Corresponding ST Plot
Velocity specification for the synthetic data is shown in (A) and the resulting ST plot is (B). The ST plot shown is actually a stack of five different cycles. The ST plot matches the data exactly as expected.

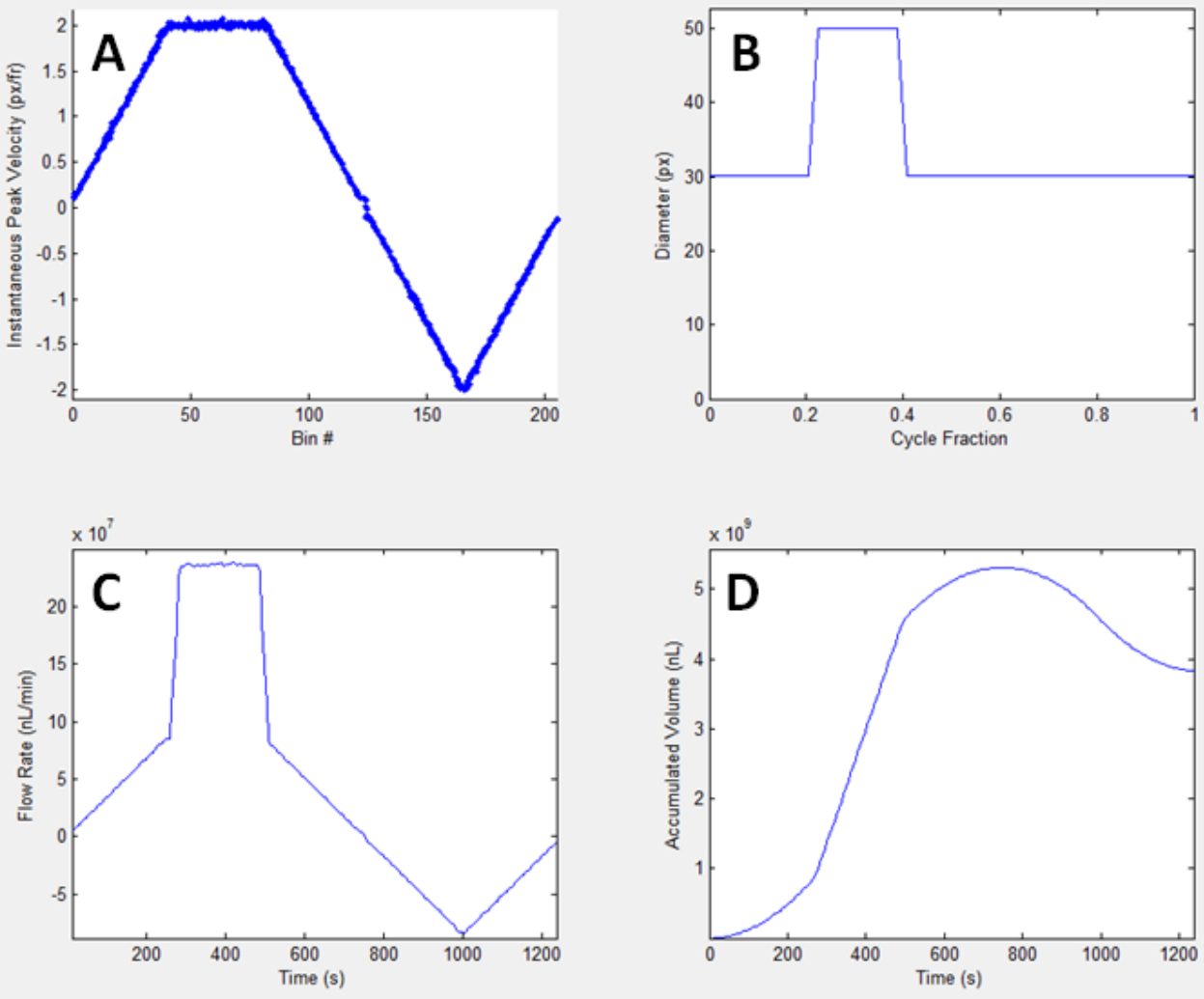

Figure 4.20 Analysis Plots Associated with Synthetic Data
Plots of velocity (A), diameter (B), flow rate (C), and accumulated volume (D) are shown above. The automated analysis matched theoretical values to within 1% accuracy.

4.27 Imaging Limitations

Some of the most significant limitations of the presented methods involve the zebrafish imaging because bright field microscopy requires an unobstructed view of the heart. The ventricular outlet lies deep within its surrounding tissue and is positioned behind the embryo's head throughout most of early development. This makes it very difficult to

obtain an unobstructed view of the ventricular outlet. Given this limitation, the zebrafish was viewed from a ventral angle, which provides an excellent view of the atrium and lower ventricle. Even as the chambers loop and grow, the entire atrium can be seen within the same focal plane. Ventricular function cannot always be evaluated from this angle, but cardiac function can be described as a whole since the circulatory system is a closed loop. In fact, some studies have described heart function by observing blood flow through large vessels like the dorsal aorta [70, 95] without even observing the heart itself. A ventral view permits the quantification of gross heart function while also providing the opportunity to perform an in-depth analysis of atrial function.

Another major limitation is the forced estimation of the cross sectional shape of the atrial inlet. Although a circular cross section makes logical sense, this may not be entirely accurate and may lead to a significant amount of error in the flow rate values obtained from the calculations. Since equivalent calculations were performed across all samples, the relative comparison of heart functionality between sets of embryos should prove insightful despite any error associated with these assumptions.

The limitations presented above can be avoided with the use of more advanced imaging techniques which take into account the 3D morphology of the heart. This methodology was centered on the use of a high speed camera affixed to a stereomicroscope, but the core concepts can be translated to virtually any imaging technology. In fact, the use of other modalities such as 3D + time confocal imaging could be used to validate some of the underlying assumptions, such as the circular cross section of the atrial inlet, and

could lead to an even more accurate analysis. Given high enough frame rates or clever enough image processing techniques, alternate imaging modalities may even become preferable.

4.28 Chapter Summary

In this chapter, an extensive methodology was developed for quantifying heart function in the zebrafish embryo from 2D high speed images of the heart. At the time of publication, this was among the most extensive and quantitatively descriptive methodologies used on the zebrafish embryonic heart. The end points of the methodology are stroke volume, cardiac output, and regurgitant fraction. These parameters provide a very good sense of how the embryonic heart functions. One can take a closer look at the velocity, diameter, and flow rate data used to reach these end points in order to gain even more insight into how the heart functions. The core idea behind this analysis (i.e. calculating parameters from flow rates) is fundamentally sound and some of the major limitations (e.g. assuming a circular cross section) can be overcome with advancing technology. The validations in this chapter confirmed that the method is quite effective and accurate. This methodology provided the framework necessary for comparing heart function in Aims 2 and 3 and will likely be useful for future studies as well.

CHAPTER 5: AIM 2

5.1 Chapter Introduction

Aim 2 was to benchmark normal heart function in the embryonic zebrafish. This was done in two ways. First, the developing heart was closely observed at 30, 36, and 48 hpf, and mostly qualitative techniques were used to describe the transitioning pumping mechanics that occur between the tube and looped stages of heart development. Next, the methodology developed in Aim 1 was used to quantify heart function at 48 and 55 hpf.

5.2 Pumping Mechanics Introduction

As described in Chapter 2, the heart tube begins to circulate blood while still in a primitive tube conformation—long before it completes development. The pumping mechanics at this stage is therefore not representative of the mechanics of a fully developed heart, which is well understood to be based upon positive displacement concepts precisely regulated by valves. The heart tube undergoes a looping process that ultimately divides it into separate chambers with heart valves. At this stage the pumping mechanics are more representative of the fully developed heart. The pumping mechanics must transition continuously between that of a valveless linear tubular pump to a more complex chambered positive displacement pump with valves. Considering the amount of research devoted to the pumping mechanics at the briefly existent tube stage

[39, 41-45, 103], there has been very little research done to describe the mechanics throughout the looping process [37, 104]. Three key time points were chosen for analysis of pumping mechanics: 30 hpf (tube stage), 36 hpf (early-mid looping), and 48 hpf (late looping).

5.3 Creation of Blood Velocity Vector Fields

Blood flow pattern was translated into a semi-quantitative vector field using the manual cell tracking approach described in Section 4.3. Wall boundaries were also tracked using manually placed splines. An example is shown in Figure 5.1. This method proved inadequate for serious quantification of flow but was useful as an aid for observing transitional pumping mechanics.

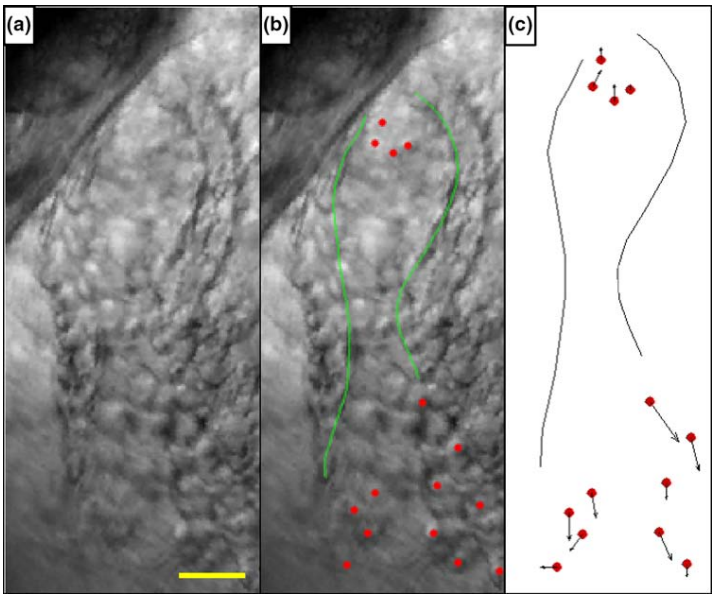

Figure 5.1 Blood Cell and Wall Tracking
Blood cells and endocardial walls from raw video (a) were manually tracked from frame to frame (b). Blood velocity vectors (c) were calculated by multiplying the distance traveled per frame by the frame rate. Scale bar indicates 25 um.

5.4 Contraction Wave Tracking

Perhaps the most useful and novel technique used in this analysis was the application of ST plots to describe contraction wave propagation through the heart (Figure 5.2). ST plots were created as described in Section 4.13. Each ST plot can reveal much about the wall and blood flow dynamics that occur at the location of its respective reference line. The caption for Figure 5.2 provides an example of the information that can be extracted. To gain information about wave dynamics, multiple reference lines were spaced evenly along the length of the heart. As the contraction waves reached each reference line, they showed up at different points in the corresponding ST plots (Figure 5.3). The relative speed of the contraction wave was determined by comparing the timing of the minimum wall diameter in each ST plot (Figure 5.4).

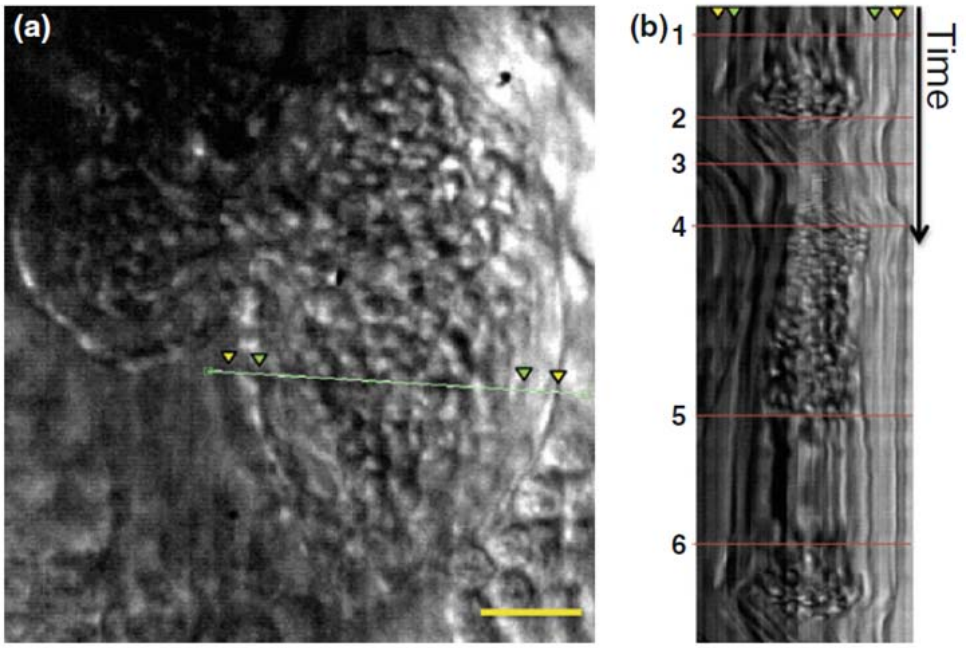

Figure 5.2 Describing Wall Mechanics with ST Plots
Spatiotemporal (ST) plots (b) are created from reference lines placed across the width of the heart as shown by the green line in (a). Yellow scale bar indicates 25 µm. As the heart wall boundary moves along the reference line, it can be seen as a solid vertical streak down the plot. Yellow and green triangles in (a) mark the exterior and interior heart wall boundaries respectively. Each boundary has its own corresponding streak pattern in (b). As blood cells cross the reference line, they appear as ellipses, whose vertical length corresponds roughly to the inverse of their speed. The red lines in (b) correspond to important events in the cardiac cycle: (1) Start of atrial systole; a new contraction wave starts at the atrial inlet inducing forward blood flow across the reference line. (2) The front of the contraction wave reaches the reference line. (3) The middle of the contraction wave crosses the reference line; some blood regurgitates through the constriction at high velocities while the majority of the blood flow continues to be pushed ahead of the contraction wave. (4) As the contraction wave moves past the reference line, more blood enters the heart marking the beginning of atrial diastole. (5) Blood cells slow to a stop as the atrium reaches its end diastolic volume. (6) The next cardiac cycle begins.

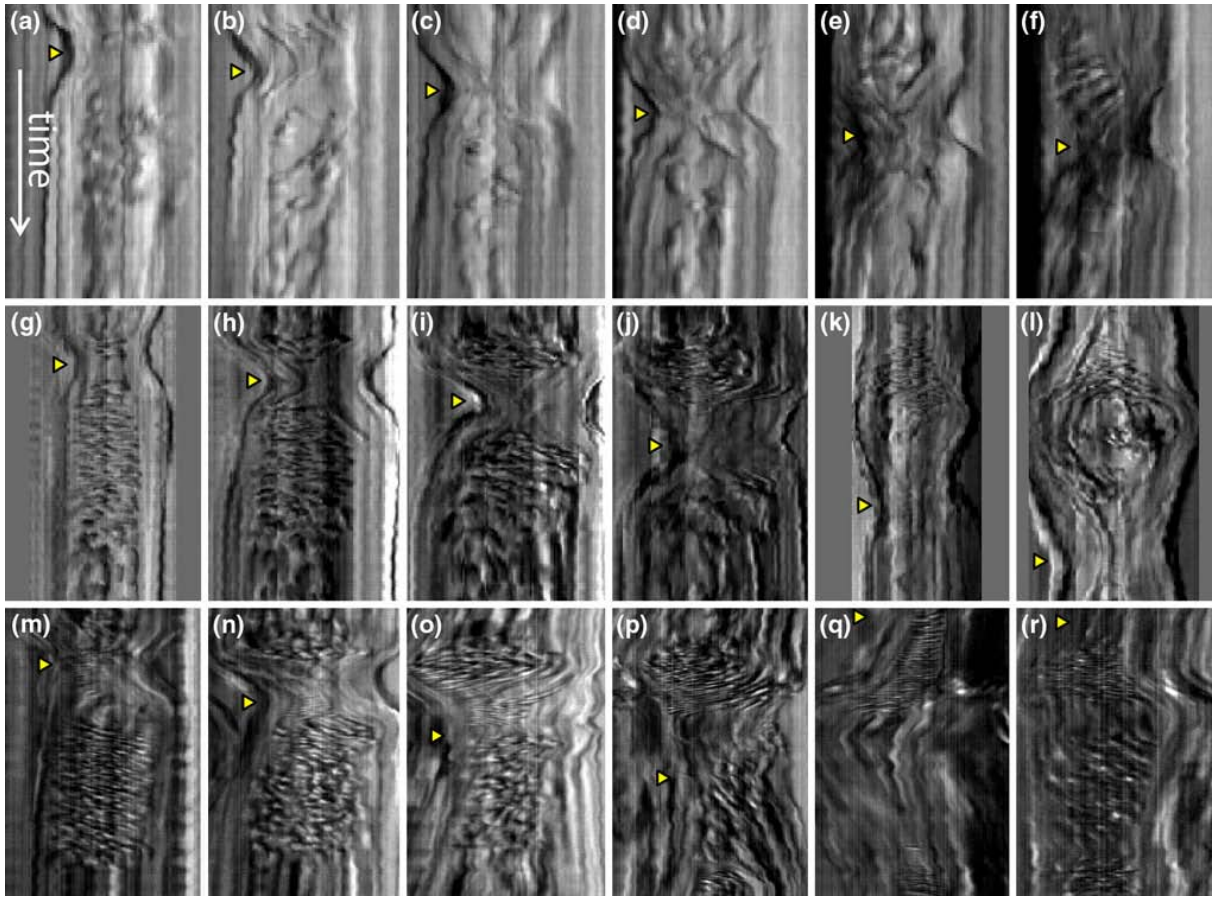

Figure 5.3 Wave Propagation through the Heart
Spatiotemporal plots were created at evenly-spaced slices throughout the length of the heart. (a)–(f), (g)–(l), and (m)–(r) correspond to tube (30 hpf), early looping (36 hpf), and late looping (48 hpf) stages respectively. The contraction wave can be seen as a narrowing in the width of the plot profile and is marked with yellow triangles. Note that the ventricular outlet cannot be observed from the imaging perspective shown; the slices at (k) and (q) are located near the atrioventricular junction. (l) and (r) are located near mid-ventricle.

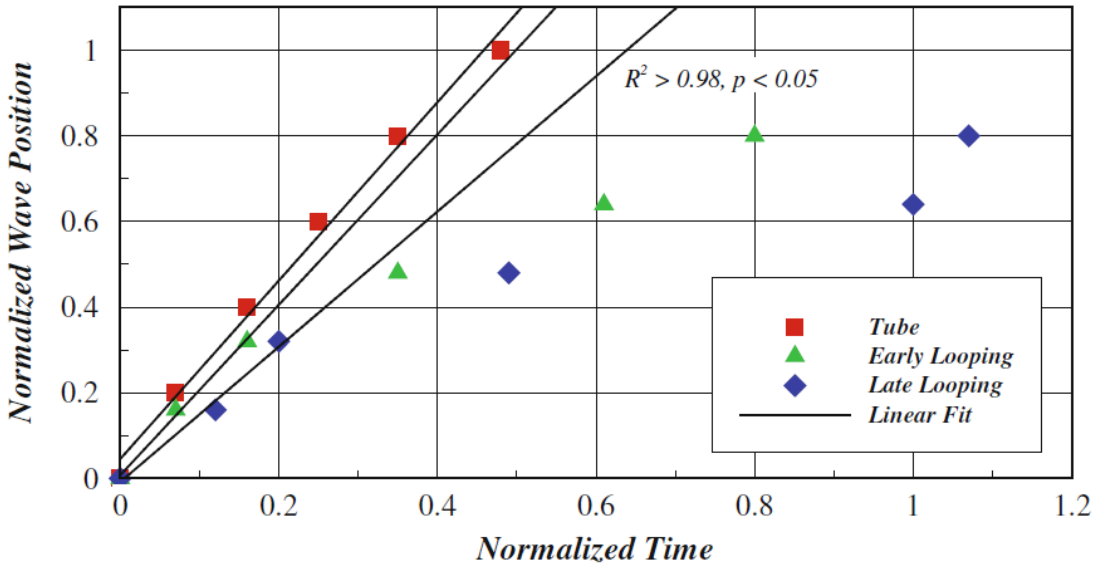

Figure 5.4 Contraction Wave Timing
Wave propagation was tracked through the heart at each time point by determining the length of time needed for the contraction wave to reach each of the evenly spaced ST plot scans through the heart. Time was normalized such that a time value of 1.00 corresponds to one complete cardiac cycle. Wave position was normalized such that the length of the heart spanned from a value of 0–1. The view of the ventricle is partially obstructed during early and late looping. Accordingly, measurements for these stages could only be taken for approximately 80% of the overall heart length. The atrioventricular junction is located approximately at normalized wave position 0.5 for early and late looping stages. Linear fits are superimposed. Only the wave positions in the atrium are included in the linear fit for Early and Late looping. The R^2 and p value refer to all three fits.

5.5 Heart Kinematics at 30 hpf

At 30hpf, the heart is in a simple tube conformation. As seen in Figure 5.3 A-F, acute contraction waves propagate through the entire length of the tube. Note that Figure 5.3A and Figure 5.3F correspond to ST plots taken at the tube inlet and outlet respectively. Given that each of the reference lines in A-F are spaced equidistantly, and the position of the wave on the time axis appears to be proportionate to the position of the reference line (see triangular markers placed at the wave peak in Figure 5.3), this suggests a nearly constant wave speed. Figure 5.4 shows a plot of the wave arrival time along the

normalized position of the reference line as a function of normalized time. The wave traverses the entire length of the heart tube in about 50% of the cardiac cycle. The variation was found to be nearly linear ($r^2 = 0.98$). The next wave occurs after a pause that lasts ~50% of the cycle.

5.6 Blood Flow at 30 hpf

At 30 hpf, blood is observed to be pushed ahead of the wave as it travels along the tube while blood cells flow through the inlet behind the wave (supplementary video SV1). A small amount of backflow occurs at the inlet while the walls are starting to contract at the beginning of the cardiac cycle. This backflow tends to cease entirely once the wave has fully contracted, and the regurgitated blood is quickly pulled back into the heart behind the wave. Figure 5.5 A-D depicts the blood flow patterns observed through the blood cell tracking scheme. The corresponding animation is shown in supplementary video SV4. Maximum blood velocities occur ahead of the wave at roughly double the speed of the contraction wave. Velocities in the retrograde direction and in backfilling are roughly equivalent.

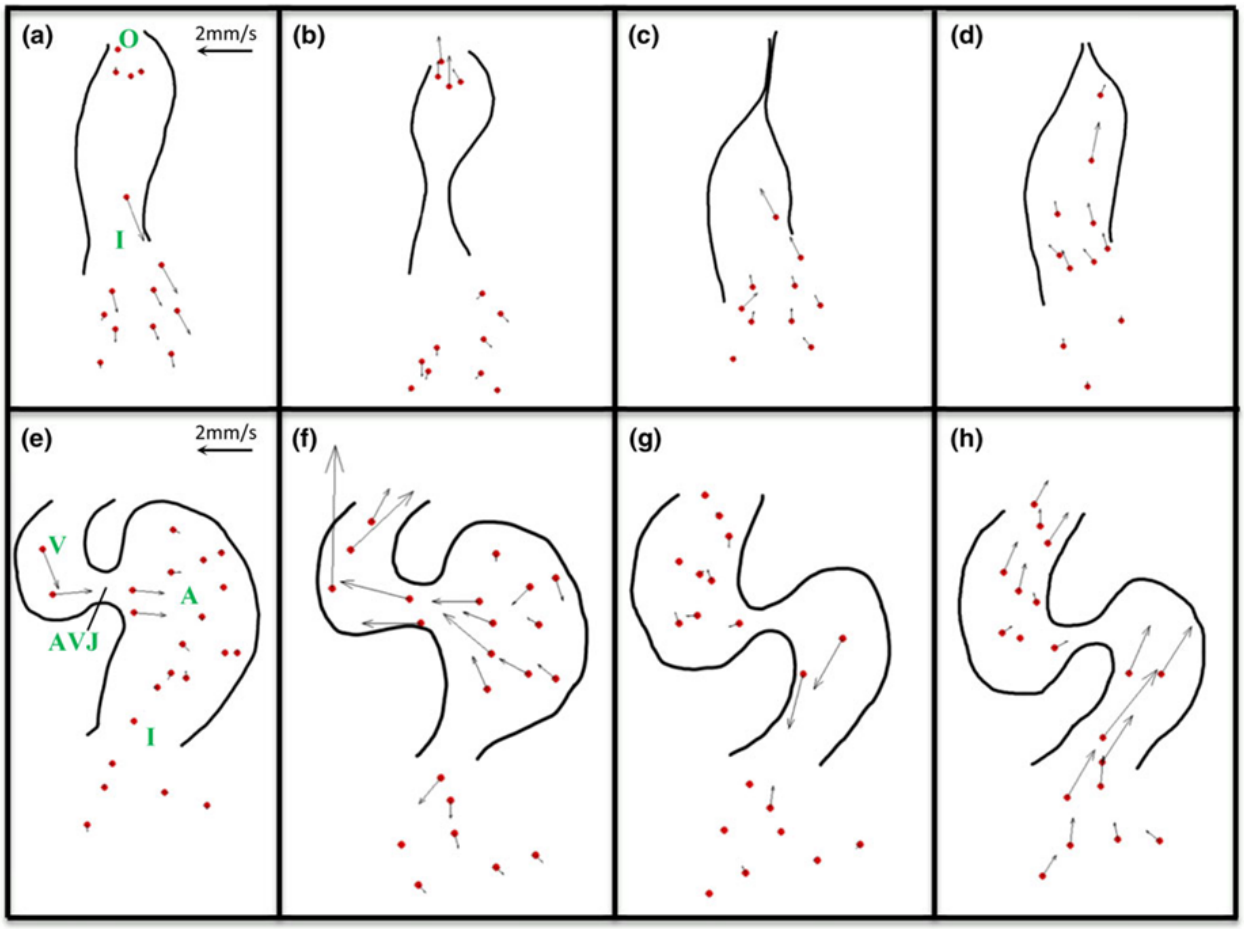

Figure 5.5 Relative Blood Velocity at 30 and 48 hpf
Relative blood velocity at 30 and 48 hpf. Representative blood cells were tracked throughout the heart at 30 hpf (a)–(d) and 48 hpf (e)–(h). Vector direction corresponds to blood flow direction and length corresponds to the relative magnitude of the blood velocity. Green labels mark key areas of interest: heart inlet (I), heart outlet (O), atrium (A), atrioventricular junction (AVJ), and ventricle (V).

5.7 Heart Kinematics at 36 hpf

By 36hpf, the heart tube begins to loop. This is seen as a bend and constriction at the AVJ, as well as an increase in the diameter throughout the newly-forming chambers. The starting kinematics appear to be very similar to that seen in the tube conformation—an acute contraction wave propagates through the atrium (supplementary video SV2). Although prominently constricted through most of the cycle,

the AVJ opens nearly as wide as the atrium and ventricle during mid-ventricular diastole. The contraction wave slows significantly as it reaches the AVJ (Figure 5.3 G-L and Figure 5.4), but continues on to the ventricle in one fluid motion. The total time for the wave to traverse the entire length of the heart is over 80% of the cardiac cycle. The ventricle appears to become more rigid throughout development and does not appear to fully contract at this stage. The next contraction wave begins at the atrial inlet only as the ventricle reaches the end of systole with the pause being much shorter than that observed during 30hpf.

5.8 Blood Flow at 36 hpf

As in the tube stage, retrograde flow continues to occur at the inlet prior to full contraction at 36 hpf. Blood is pushed through the heart ahead of the contraction wave while more blood simultaneously enters the atrium behind it. Blood is pushed from atrium to ventricle in one continuous motion. During ventricular systole, some blood is forced backward through the AVJ. Maximum blood velocities at this stage are seen ahead of the wave and in the retrograde flow at the AVJ.

5.9 Heart Kinematics at 48 hpf

By 48hpf, the chambers are very well defined and the AVJ remains notably constricted throughout the entire cycle. The atrium continues to contract in a wave-like motion from inlet to AVJ, but the upper atrium no longer constricts entirely at maximum contraction

(supplementary video SV3). The atrium appears to have more three dimensional structure than in previous stages. The ventricular contraction no longer resembles a wave, but instead appears to contract as a unit in a single motion. As seen in Figure 5.3 M-R, the contraction wave appears to travel roughly at the same speed while still between the inlet and the AVJ. However, there appears to be slower progression through the AVJ resulting in the wave reaching the outlet beyond one cardiac cycle time. Figure 5.4 confirms the nearly uniform wave speed and a significant slowdown of the wave through the AVJ.

5.10 Blood Flow at 48 hpf

As seen in both Figure 5.3 M-R and in the supplementary video SV3, the stronger constriction at the AVJ provides more resistance for blood flow between the atrium and ventricle at 48 hpf. It also increases the regurgitation velocity. Although most of the atrial blood volume is pushed into the ventricle on each cycle, a portion of the blood from the upper atrium is left behind as the AVJ constricts ahead of it. This separated portion is pushed backward toward the atrial inlet. This is further illustrated in the relative blood velocity fields shown in Figure 5.5 E-H and the corresponding supplementary video SV5.

5.11 Discussion of Transitional Pumping Mechanics

During this transitional period from 30 to 48 hpf, there is a significant change in morphology, mechanics, and blood flow. An especially important change is the apparent

adoption of valvular function at the AVJ, even before the formation of valve leaflets, and the transition to a displacement pump mode. Here, the cardiac biomechanics were investigated using the rather simple techniques of cell tracking and ST plots. This method works well for addressing gross cardiac mechanics. However, more advanced methods such as 4D imaging [17, 37] and sophisticated image processing techniques[105] paired with DPIV[69, 81] can be applied to gain a deeper understanding of this transitional period.

Figure 5.6 provides an overall summary of the main phases of the cardiac cycle during the three stages of the transition studied. Snapshots are shown at only three time points in the interest of brevity. Observations of intermediate developmental stages revealed a predictably continuous and progressive development from 30-36hpf and from 36-48hpf. As the heart tube loops toward an adult configuration, several trends appear to develop in a continuous fashion.

As the heart develops, it grows in size and the chambers “balloon” [36]. Unlike the chambers, the AVJ does not drastically increase in size. This creates a prominent constriction at the AVJ relative to the atrium and ventricle. This is evident in Figure 5.6 (A,F,K) and in the supplementary videos SV1-SV3. At 30hpf there is only a small conduit for blood flow which quickly expands into evident chambers before 36hpf. By 48hpf, the chambers appear much rounder and spend nearly the entire cardiac cycle in an ellipsoid shape. The AVJ elastically expands during mid-ventricular diastole at 36hpf (Figure 5.6H) but remains significantly more constricted at 48hpf (Figure 5.6M). By

definition, the ventricle is repositioned to the side of the atrium in the looping process (Figure 5.6 A,F,K).

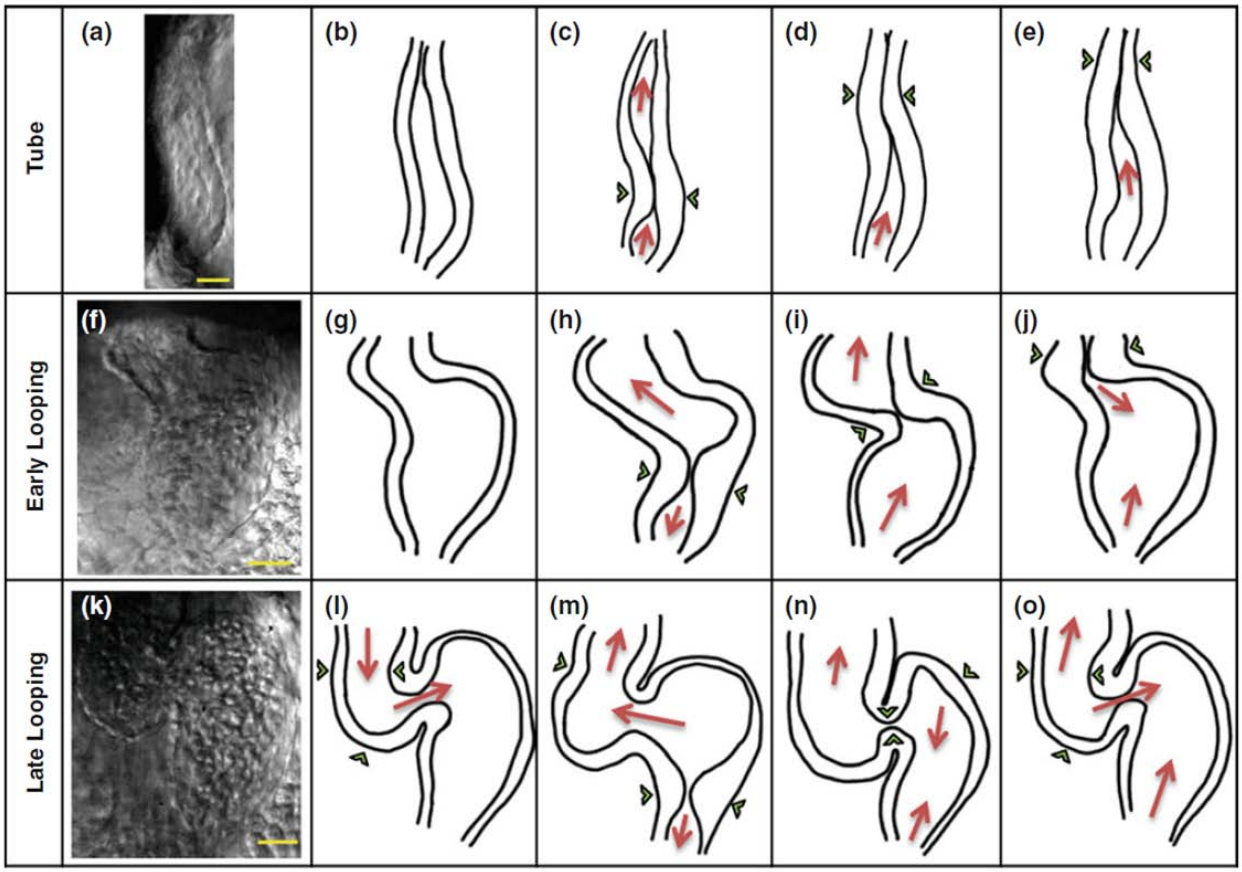

Figure 5.6 Changes in Cardiac Biomechanics
In the figure above, each row corresponds to a different point in embryonic heart development. (a), (f), and (k) show the raw image of each stage at the end of atrial diastole, just before the start of the next cardiac cycle. (b), (g), and (l) show a corresponding simplified cartoon of the heart. The following columns show the progression of the cardiac cycle. Red arrows indicate blood direction and relative velocity. Green markers indicate the points of greatest contraction along the heart wall. During the tube stage, contraction occurs via propagating waves that proceed from inlet to outlet. These propagating waves are still present in the early looping stage, but the widening chambers and AVJ constriction begin to change the blood dynamics. By the end of looping, contraction no longer resembles a propagating wave. Yellow scale bars indicate 25 μm.

The heart pumps more forcefully as it grows, and blood velocities increase. After the start of cardiac looping, maximum blood velocities occur in the retrograde direction, particularly at the AVJ which has a narrower cross-sectional area. The AVJ begins to

act as a nozzle as it becomes more constricted, accelerating blood as it passes through. By 36hpf, the velocity of the retrograde blood flow through the AVJ at the end of ventricular systole is significantly faster than velocities elsewhere in the heart (supplementary video SV2). This regurgitant flow velocity continues to increase through 48hpf (supplementary video SV3). As the atrium balloons, it develops a prominent bulge to the periphery of the main flow stream (Figure 5.6 H,M); upper right portion of atrium in the graphic). Blood from this area is the last to be expelled from the atrium. At 36hpf, the vast majority of this blood is ejected into the ventricle just behind the main flow. However, as the heart continues to loop and the AVJ becomes more constricted, an increasingly greater percentage of this volume remains in the atrium (Figure 5.6N, supplementary video SV3).

Based on the above observation of morphological and blood flow trends, several inferences regarding the transitioning pumping mechanics can be made throughout the early stages of heart development. As shown in Figure 5.4, the contraction wave proceeds through the heart tube at a relatively constant speed. As the heart begins to loop, however, the contraction wave slows substantially at the upper atrium and AVJ. By 48hpf, the ventricular wave delay is long enough that it no longer appears continuous with the atrial contraction. The ventricle stops entirely constricting during early looping, and it seems to contract more in a chamber-wide motion by 48hpf (supplementary video SV3). Long before the formation of functional leaflets, the ventricle begins pumping with adult-like mechanics. This may be due to an increase in afterload, but assessing the afterload is beyond the scope of this study. The atrium

shows a similar trend but continues to produce wave-like contractions even at 48hpf (supplementary video SV2 and SV3).

During the tube stage the contraction wave appears active because it is able to completely constrict the tube as it moves from inlet to outlet. Significant active waves suggest that the heart tube may function predominantly by peristalsis. However, Loumes et al. [44] showed that the passive waves of multi-layered impedance pumps are enhanced by a thick gelatinous layer, which is like the cardiac jelly seen within the walls of the embryonic heart tube. Unfortunately, the degree of wall activity or passivity cannot be determined using the methods presented here. Impedance pumps are strongly dependent on contraction frequency to generate flow. The long pause between the end of one traveling wave and the beginning of the next wave at 30hpf seems to speak against the idea of impedance pumping. On the other hand, in agreement with Forouhar et al. [41], peak blood velocities within the heart tube were significantly higher than that of the contraction wave, ruling out the possibility that it acts as a technical peristaltic pump. Without an advanced examination of the material properties and pressures within the heart tube, the exact pumping mechanisms are extremely difficult to determine. The heart eventually develops into a displacement pump in which a volume of blood is trapped and expelled with the use of one-way valves. Given the continuous nature of the evolution from tube to looped conformations, and from wave to unitary chamber contraction, we can conclude that multiple pumping mechanisms must exist simultaneously during this transition period. This is especially evident in the early

looping phase, where a traveling wave provides the impetus for forward blood flow while the AVJ acts as a rudimentary valve to limit regurgitation between the chambers.

After 36 hpf, a strong synchronization exists between the atrium and ventricle, even between separate cardiac cycles. In all stages, the ventricle contracts at near-optimal timing: just as the atrium finishes emptying. There were no observed cases in which the atrium and ventricle appeared out of sync. As mentioned previously, the AVJ strongly constricts immediately following ventricular diastole, and remains constricted until nearly the end of ventricular systole. This portion of the mechanics is what forces a valve function at the junction even in the absence of the valve through a periodic and synchronized resistance to flow. During this time, there is only a small amount of retrograde flow through AVJ, further demonstrating the effective valvular role adopted. Just prior to the end of ventricular systole, the AVJ relaxes, allowing a very brief period of unrestricted backflow from the ventricle (supplementary video SV3). This backflow is made nearly inconsequential by the fact that the next cardiac cycle immediately pushes the atrial blood volume back through the AVJ. This is clearly an active contraction-relaxation process due to the fact that so little retrograde flow is seen during the period of highest pressure differential between chambers. This synchronized timing between cardiac cycles and AVJ contraction allow the embryonic heart to pump quite efficiently despite a lack of valves.

5.12 Pumping Mechanics Summary

Here it was shown that the kinematics of the embryonic zebrafish heart progress in a continuous fashion, from a simple, propagating wave to a more complex two-chamber system with rudimentary “valves” and highly synchronized timing. Multiple trends exist in this process. Morphological trends include: (a) a ballooning of the chambers, (b) increasing constriction at the AVJ, and (c) repositioning of the ventricle toward the side of the atrium. Blood flow trends include: (a) higher blood velocities, (b) increased AVJ regurgitation, and (c) larger percentages of blood from the upper atrium are expelled backward toward the atrial inlet. Pumping mechanics trends include: (a) increasing contraction wave delay at the AVJ, (b) the AVJ begins acting as a rudimentary valve, (c) decreasing chamber constriction during maximum contraction, (d) and a transition in ventricular kinematics from a pronounced propagating wave to an independent, full-chamber contraction. With improved understanding of the changing kinematics and blood dynamics in the critical stages of heart development, we can better approach the topic of epigenetic forces and their role in cardiac defects.

5.13 Quantitatively Benchmarking Heart Function

Although the mainly qualitative methods used in the pumping mechanics study were able to provide some useful and interesting information, a quantitative approach provides a more thorough investigation of heart function. Here the methodology developed in Aim 1 was utilized to quantitatively benchmark heart function at 48 and 55 hpf. 48 hpf is one of the major time points observed in most developmental studies and

marks the approximate end of cardiac looping. 55 hpf has been observed in a few studies [4, 29, 48] and marks the approximate end of reliable unobstructed observations of the atrium using bright field microscopy. Several parameters were calculated including stroke volume, retrograde fraction, looping angle, and lumen diameter. These benchmarks were used in Aim 3 to compare with treatment groups.

5.14 Benchmark Measurement Methods

Zebrafish were raised, bred, and imaged at 48 and 55 hpf as described in Sections 3.2 and 3.3. Image sequences were analyzed using the methodology presented in Aim 1. Two additional parameters were created in order to describe the overall heart morphology: looping angle and lumen ratio. Looping angle has been described previously as the angle between the axis of the atrioventricular canal and the embryo's midline [4]. Here, an arguably superior variation is employed to measure the amount of cardiac looping. Looping angle is defined here as the inside angle between the axis of the atrioventricular canal and the axis of the atrium (Figure 5.7 A and B). This method prevents an array of theoretical miscalculations that could result from unexpected external influences on heart orientation (e.g. a normally looped heart that is abnormally positioned in the chest due to edema). By relating the two angle axes to the heart itself, the degree of cardiac looping can be judged independently of inter-cardiac oddities which may arise. It also avoids the necessity to accurately assess the embryo's body position and mid-line angle.

The lumen ratio is a parameter that was defined in order to describe the relationship between the lumen diameter and wall thickness. The lumen ratio, R_{lumen}, is defined here as:

$$R_{lumen} = \frac{D_L}{D_H}$$

Where D_H is the total diameter of the atrium between outer edges the myocardium, and D_L is the diameter of the lumen between inner edges of the endocardium (Figure 5.7C). A large ratio indicates that a large amount of ballooning has occurred or that the wall is especially thin. Cardiac looping and lumen ratio measurements were taken at the end of atrial diastole in the middle of the atrium at its widest point.

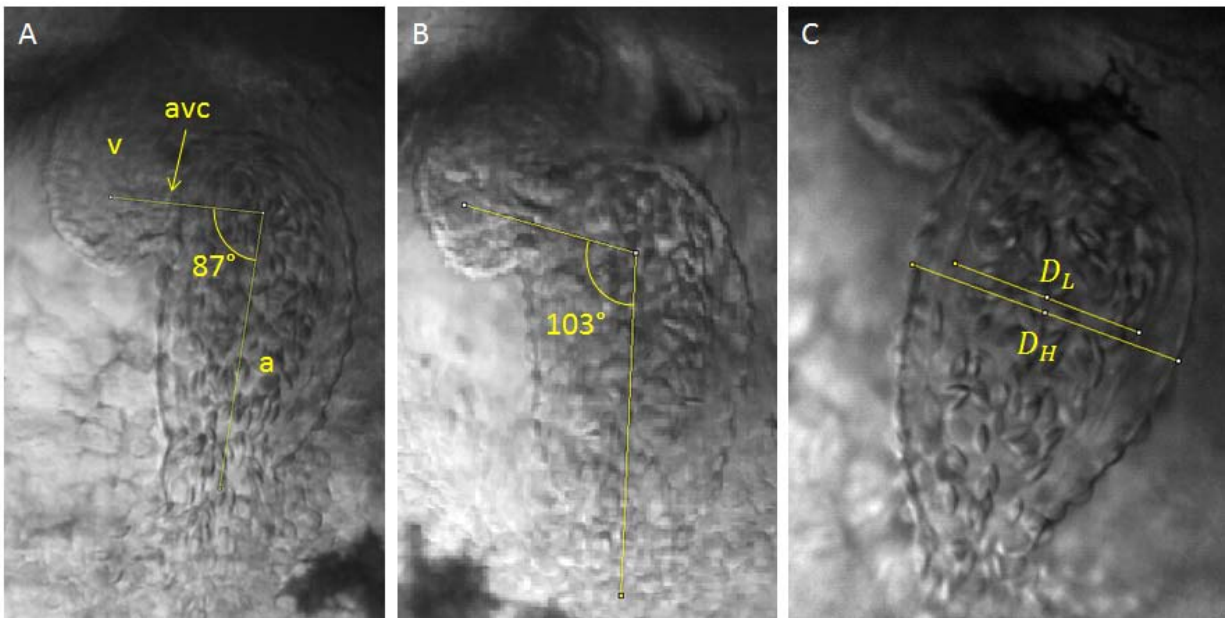

Figure 5.7 Looping Angle and Lumen Ratio Measurement
Looping angle is defined here as the inside angle between a line bisecting the atrium and a line parallel to the flow of blood through the atrioventricular canal. Two hearts are shown with looping angles 87° (A) and 103° (B). Lumen ratio is defined the ratio of the heart lumen, D_L, to the overall diameter of the heart, D_H (C). Abbreviations: v = ventricle, avc = atrioventricular canal, a = atrium.

5.15 Benchmark Results as 48 and 55 hpf

Figure 5.8 and Figure 5.9 show the raw data resulting from the methodology developed in Aim 1. Again, velocity and diameter measurements are used to estimate the flow rate and accumulated volume over time. All samples are plotted for each time point in order to indicate the consistency of the curves. The stroke volume is the final value reached in the accumulated volume plot. Box plots of stroke volume, cardiac output, regurgitant fraction, inlet diameter, looping angle, and wall fraction are shown in Figure 5.10.

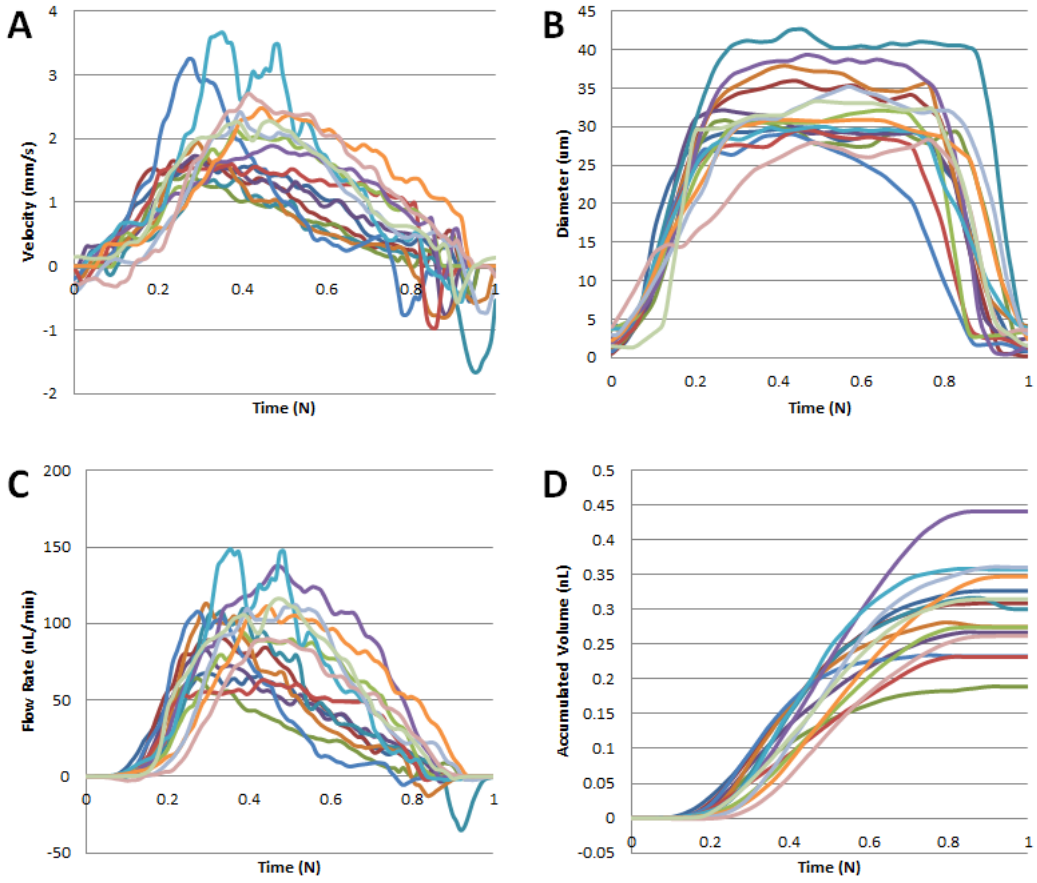

Figure 5.8 Raw Data for All 48 hpf Samples
Velocity (A), atrial inlet diameter (B), flow rate (C), and accumulated blood volume (D) are plotted above for all 48 hpf samples. Time is normalized such that a complete cardiac cycle spans from 0 to 1.

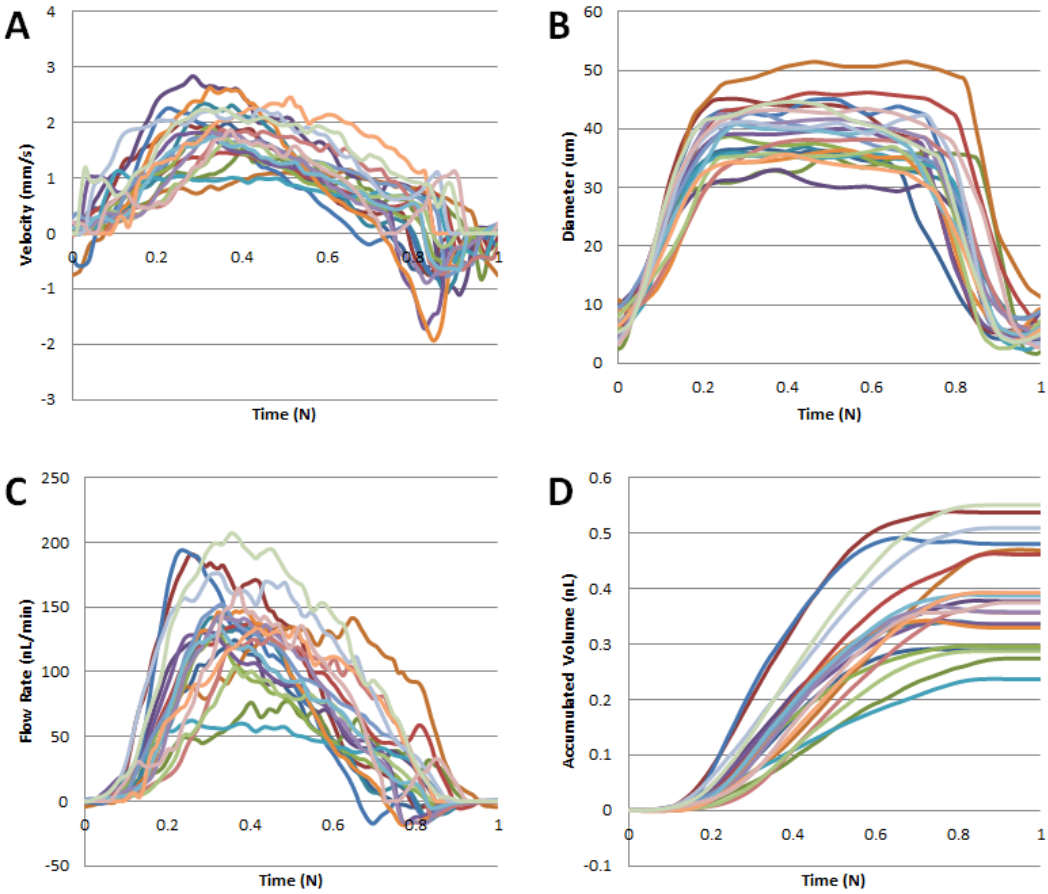

Figure 5.9 Raw Data for All 55 hpf Samples
Velocity (A), atrial inlet diameter (B), flow rate (C), and accumulated blood volume (D) are plotted above for all 55 hpf samples. Time is normalized such that a complete cardiac cycle spans from 0 to 1.

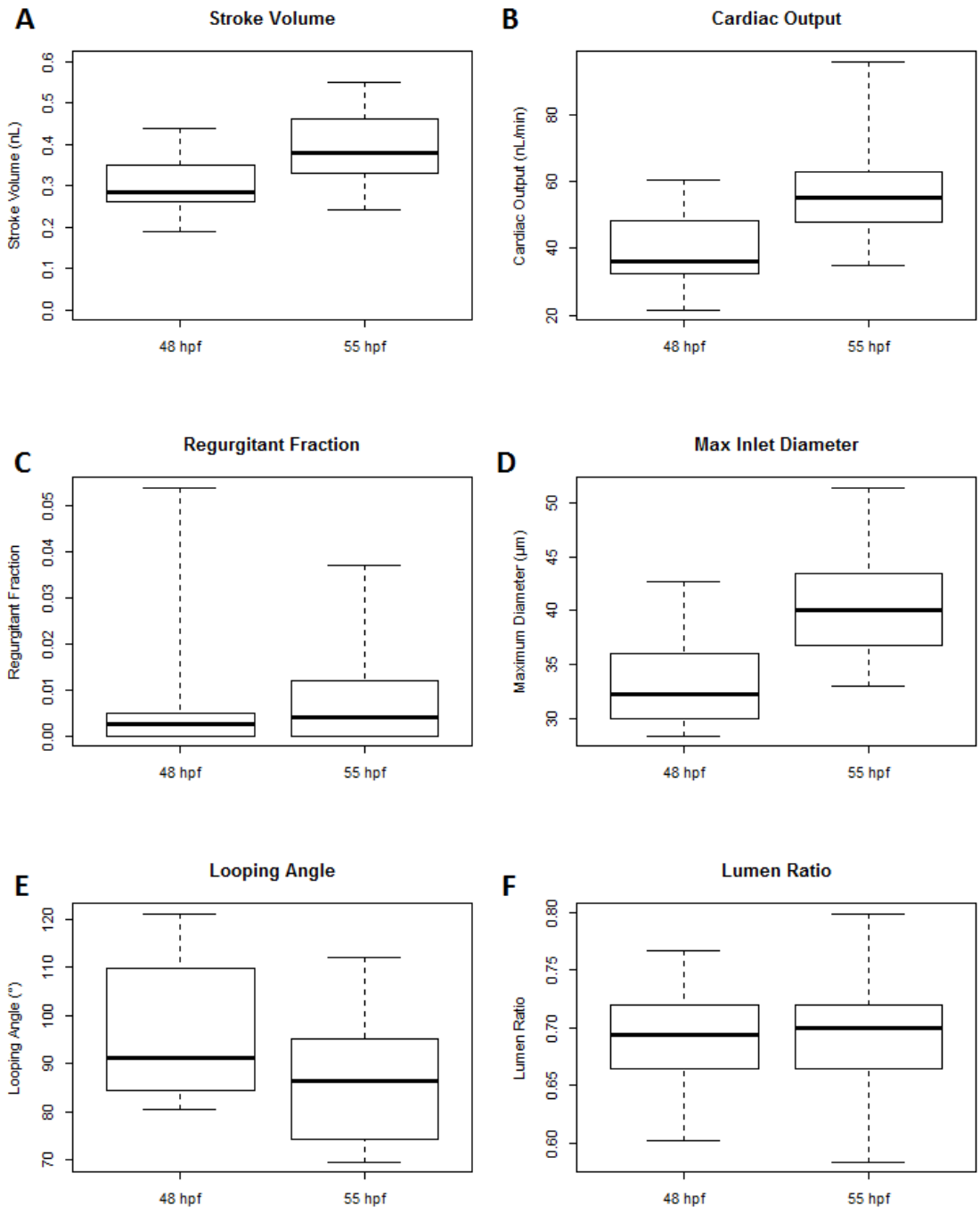

Figure 5.10 Box Plots of Parameters at 48 and 55 hpf
Stroke volume (A), cardiac output (B), regurgitant fraction (C), maximum atrial inlet diameter (D), looping angle (E), and lumen ratio (F) are plotted for wild-type embryos at 48 and 55 hpf. Boxes represent data boundaries for 25th and 75th percentile. The mean for the given parameter is marked by the black bar. Whiskers extend to the most extreme data points.

Because flow rate is calculated based on the blood velocity through the cross sectional area of the atrial inlet lumen, there is a direct physical relationship between the flow rate and the square of the atrial inlet diameter. This relationship was plotted in Figure 5.11.

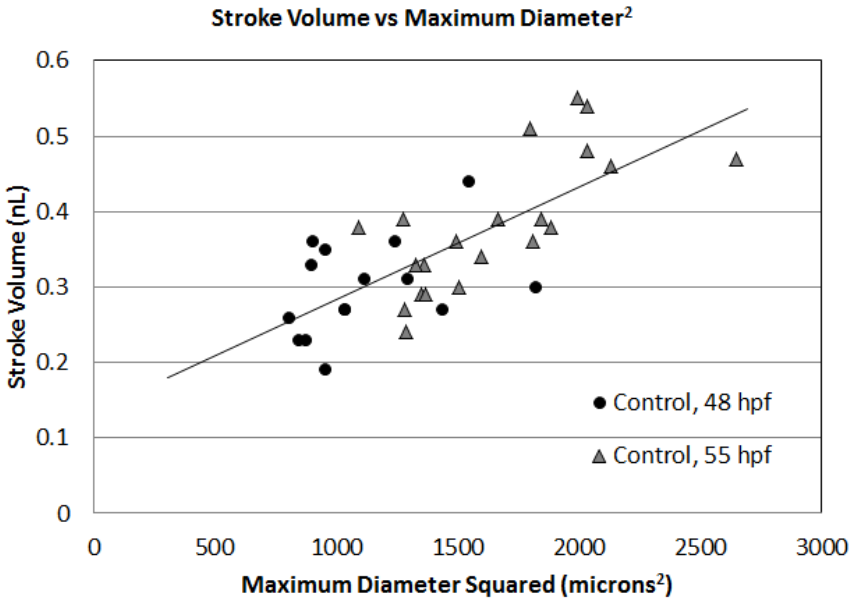

Figure 5.11 Stroke Volume vs. Square of Inlet Diameter
Stroke volume is the integral of flow rate over a complete cardiac cycle, and flow rate is a function of the area of the atrial inlet. Stroke volume was found to be strongly correlated to the square of the maximum atrial inlet diameter (R-square = 0.54). Correlation slope is $1.49X10^{-3}$ ($p<.0001$).

5.16 Discussion

The raw data in Figure 5.8 and Figure 5.9 provides an indication of the amount of variability that exists between wild-type fish. Although there is a fair amount of variability, each sample follows the same general curve. This indicates that all hearts have varying degrees of the same functionality. The box plots in Figure 5.10 confirm that heart size and function is increased in older fish: stroke volume ($p=0.0036$), cardiac output ($p=0.0006$) and maximum inlet diameter ($p<0.0001$) are all greater at 55 hpf than

at 48 hpf. There is no statistical difference (p=0.76) in the small amount of regurgitation that occurs in each group. Looping angle decreases (p=0.05) between 48 and 55 hpf. Although the majority of cardiac looping should be complete by 48 hpf, the heart morphology continues to change through 100+ hpf, as can be seen in Figure 2.4. Thus this result is consistent with expectations. There is no difference in lumen ratio between groups (p=0.87) indicating that chamber ballooning is essentially complete by 48 hpf.

Figure 5.11 shows the correlation (r-square = 0.53) between stroke volume and diameter squared. Although the relationship is not as closely correlated as might be expected, it can nonetheless be used to normalize stroke volume to heart size. This correlation will be used to investigate relative pumping efficiency in treatment groups in Aim 3.

5.17 Chapter Summary

In this chapter, pumping mechanics and cardiac function were examined in the wild-type zebrafish embryo. The drastic changes that occur in pumping mechanics from 30 to 48 hpf surely result in an equally drastic change in mechanical stresses on the heart. Considering the amount of evidence indicating that mechanical stress plays an important role in development, this is a very interesting time span in which to perform load-altering experiments. The benchmarks measured in this chapter will provide the basis for comparisons with treatment groups in Aim 3.

CHAPTER 6: AIM 3

6.1 Chapter Introduction

The final aim of the project was to use the methods developed in Aim 1 along with the benchmarks measured in Aim 2 in order to test the effect of the timing of altered loading on heart development. The final problem to solve was to design an experiment capable of testing this hypothesis. This is actually a deceptively difficult problem because virtually all previous studies involving altered cardiac loading used irreversible procedures (or procedures so invasive as to be essentially irreversible) to accomplish the task. To look at the effect of *timing* a technique must be used which can be applied and ceased at will. This was accomplished with centrifugation.

6.2 Centrifugation as a Method for Altering Cardiac Loading

Centrifugation has strengths over alternative approaches in that it is temporary and noninvasive. Most previous studies such as vitelline vein ligation, left atrial ligation, and conotruncal banding in chicks [15, 61-63], or surgical implantation of polymeric beads into the circulation of zebrafish [69] used invasive, irreversible procedures. Centrifugation is not as precise and direct in altering flow mechanics as surgical procedures such as atrial ligation, but it should theoretically create a similar change in cardiac loading. Preload is a measure of the amount that cardiomyocytes are stretched at the end of diastole (just before contraction). As the embryo is rotated, the induced

rotational acceleration is expected to cause pooling of blood at the extremities and within the yolk—effectively removing blood from the active circulation. With less blood returning to the heart, the heart does not fill as easily and the amount of blood in the heart before each contraction is reduced (i.e. decreased cardiac preload).

To ensure that pooling actually occurred as expected, a small experiment was performed on transgenic fish, Tg(gata1:mRFP)^{ko5} with fluorescent blood cells. Although the fluorescent signal was too dim to use with high speed imaging, it worked well for visualization of blood pooling. Images were acquired with 15 second exposure times. Under these conditions, circulating blood cells were seen as a blur while pooled cells were easily distinguished (Figure 6.1). Unfortunately, this mini-experiment was poorly documented and numbers do not exist for the following observations. However, pooling was consistently seen within the yolk of rotated fish. In more than half of cases, pooling was present in the tail as well. In a minority of cases, pooling was noticeable within the head vasculature. The results showed that pooling is present in the majority of cases, confirming that centrifugation is altering the blood flow dynamics.

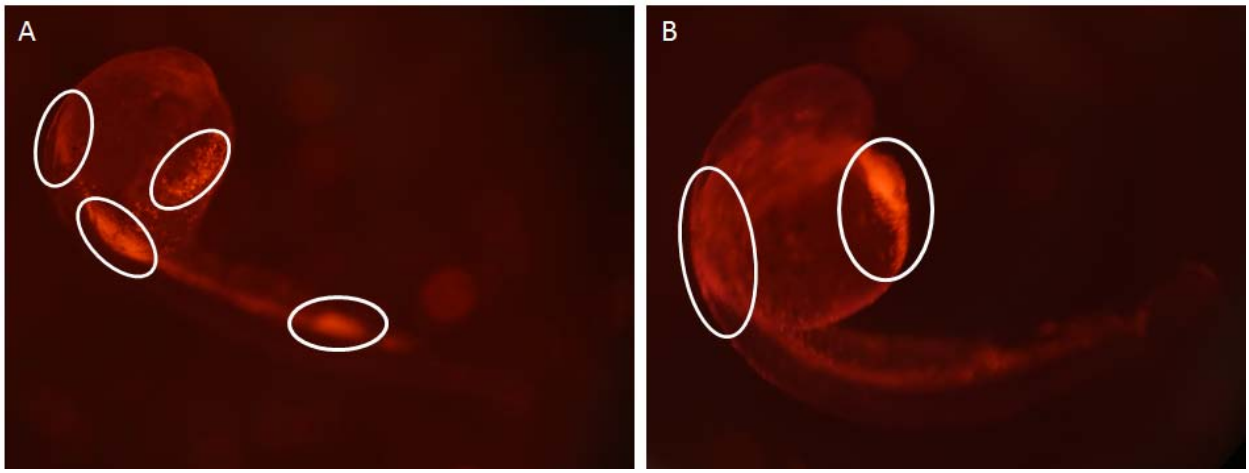

Figure 6.1 Blood Pooling Resulting from Centrifugation
Images were taken of transgenic fish using a 15 second exposure time. Some major areas of blood pooling are circled.

6.3 Centrifugation Experiment Methods

At the time point of interest, embryos were loaded head-down into a section of polymer tubing (Cole-Parmer, FEP tubing, 1/32” ID) which was held vertically within a water-filled centrifuge tube with agarose gel (Figure 6.2A). Centrifuge tubes were attached to a 3D printed centrifuge tube holder affixed to a variable-speed motor such that the final orientation of the embryos was head-out (Figure 6.2B). This orientation promoted blood flow toward the anterior extremity while preventing the tail from folding under centrifugally induced loading (Figure 6.2C). Fish were rotated at 15 Hz while continuing to be incubated at 28°C. Calculations indicated that 15 Hz should induce a pressure differential across the heart at a magnitude on the order of the pressure within the heart itself. In a series of tests, 15 Hz was confirmed to be a nonlethal rotation rate capable of inducing cardiac defects. After six hours of rotation, embryos were removed from the centrifuge and were placed in a petri dish of embryo water.

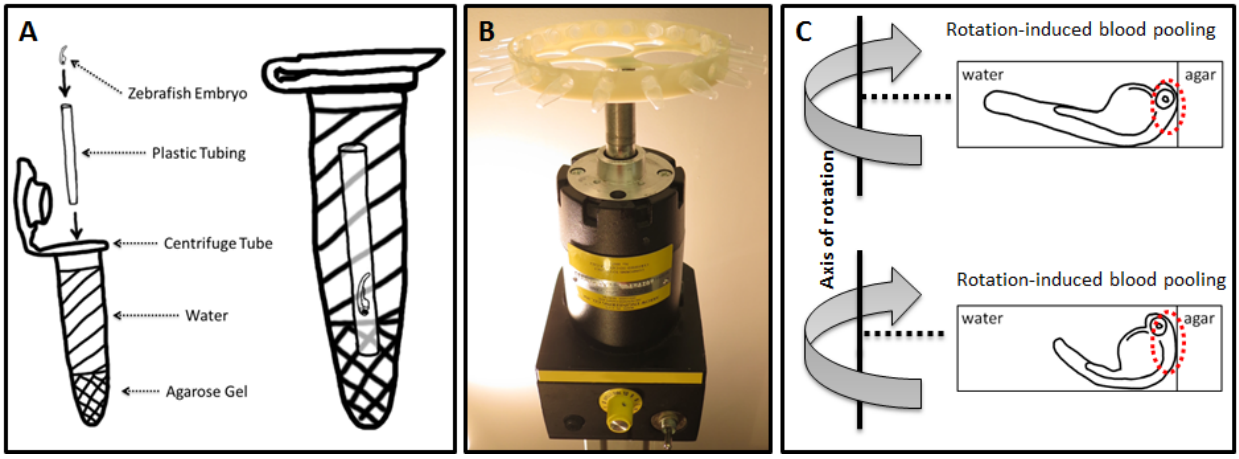

Figure 6.2 Rotation Experiment Setup
Centrifuge tubes were partially filled with agarose gel then topped off with water (A). Embryos were placed head-down within plastic tubing which was embedded into the gel to maintain orientation. Centrifuge tubes were loaded into centrifuge apparatus such that embryos were oriented with their heads radially outward (B). Rotation induces a centrifugal pull which acts to pool blood toward the extremities. The exact pooling pattern is likely dependent on the particular orientation of the embryo. Two likely orientations resulting from the procedure described are shown in (C) with area of likely pooling encircled by red dashed line.

Four six-hour treatment times were chosen: 24-30 hpf (beginning of circulation in heart tube), 30-36 hpf (heart tube and early cardiac looping), 36-42 hpf (mid-cardiac looping), and 42-48 hpf (late cardiac looping). An overview of the experiment timing and treatment groups is provided in Figure 6.3.Given the time consuming nature of the experimental setup and imaging, there was a limit to the number of embryos which could be observed in each group at a given time point. Embryos from several clutches were therefore used. Embryo development between wild-type clutches is highly repeatable and all other conditions were kept constant between groups. All embryos were dechorionated at approximately 24 hpf. Control embryos were kept within a petri dish of embryo water within the incubator for the duration of the experiment.

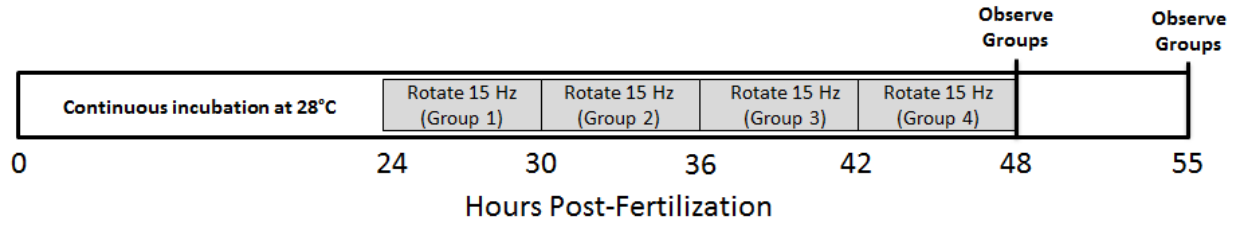

Figure 6.3 Overview of Study Timing
Four treatment groups were created by rotating embryos at 15 Hz at incremental 6-hour time periods. Embryos were observed at 48 and 55 hpf.

6.4 Centrifugation: Morphological Results

Table 2 shows the sample sizes for each group. Embryos appeared to be undamaged from centrifugation but showed temporary signs of stunted growth. Embryo head-trunk angle can be used as an indicator of developmental age[94]; between 24 and 72 hpf, the angle between the embryo's head and tail transitions from just under 90° to just under 180°. The overall embryo morphology appeared normal in all groups after rotation, but the head-trunk angle was initially stunted compared to control embryos. Embryos continued to develop in an apparently normal fashion and recovered comparable head-trunk angles to control embryos by 55 hpf (data not shown).

Table 2 Sample Sizes for Each Group

Group #	Description	Observed 48 hpf	Observed 55 hpf
0	Control	19	23
1	15 Hz, 24-30 hpf	9	11
2	15 Hz, 30-36 hpf	15	12
3	15 Hz, 36-42 hpf	10	9
4	15 Hz, 42-48 hpf	10	8

Overall heart morphology remained fairly consistent within control groups; the lowest performing hearts from the control groups were morphologically comparable to the rest of the group (Figure 6.4 and Figure 6.6). Heart morphology varied widely both between

and within treatment groups; hearts ranged from apparently normal to severely defective. Figure 6.4, Figure 6.5, and supplementary video SV6 show representative hearts from each group. The hearts shown in these figures had stroke volumes very near the group average. Hearts are shown during the end of atrial diastole and the end of atrial systole. Figure 6.6, Figure 6.7, and supplementary video SV7 show the lowest performing hearts from each group, where the most severe of the cardiac morphologies can be seen.

Qualitatively, severely defective hearts had a pronounced reduction in cardiac looping, altered chamber width (reduced in most cases), reduced blood cell concentration, and seemingly weaker chamber contractions. To describe morphology quantitatively, looping angle and lumen ratio were measured. Groups 1 and 4 had significantly larger looping angles (less cardiac looping) than controls at 48 hpf. Groups 1, 2, and 4 had significantly larger looping angles at 55 hpf (Figure 6.8 A and B). Group 1 had a significantly lower lumen ratio versus the control at 48 hpf while Groups 1, 2, and 4 had significantly lower lumen ratios versus the control at 55 hpf (Figure 6.8 C and D).

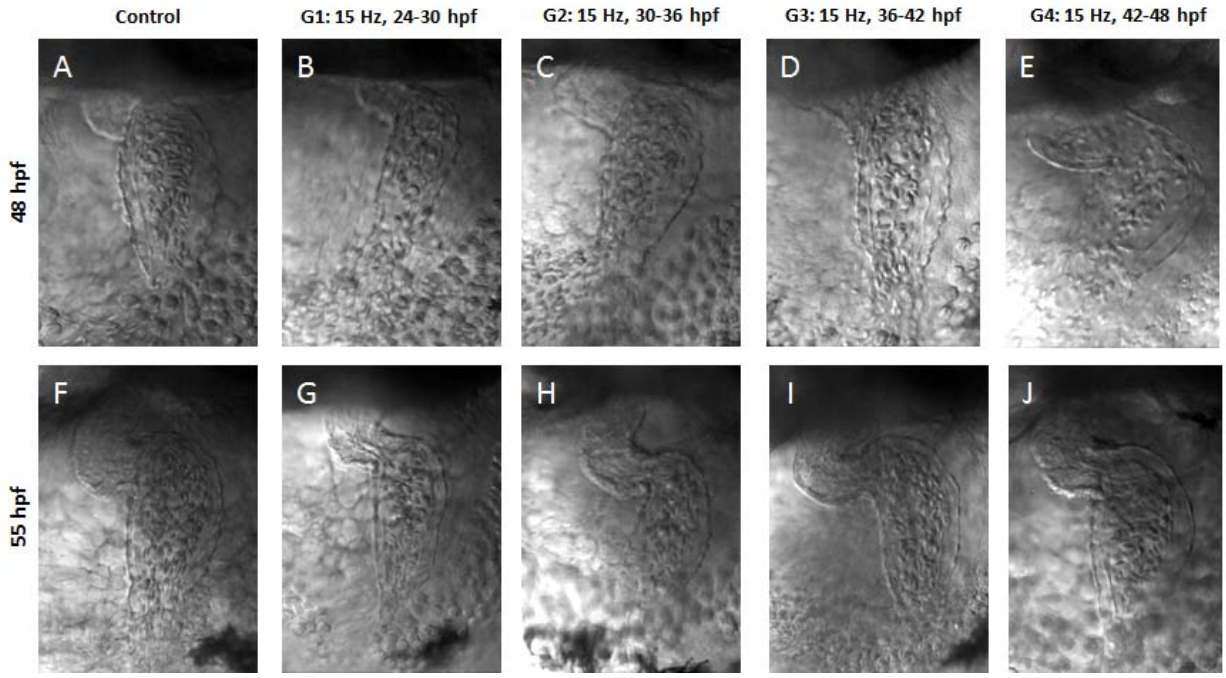

Figure 6.4 Representative Hearts at the end of Atrial Diastole
Hearts with stroke volumes very near the group mean were chosen from each group. Hearts are shown at the end of diastole at 48 hpf (A-E) and 55 hpf (F-J).

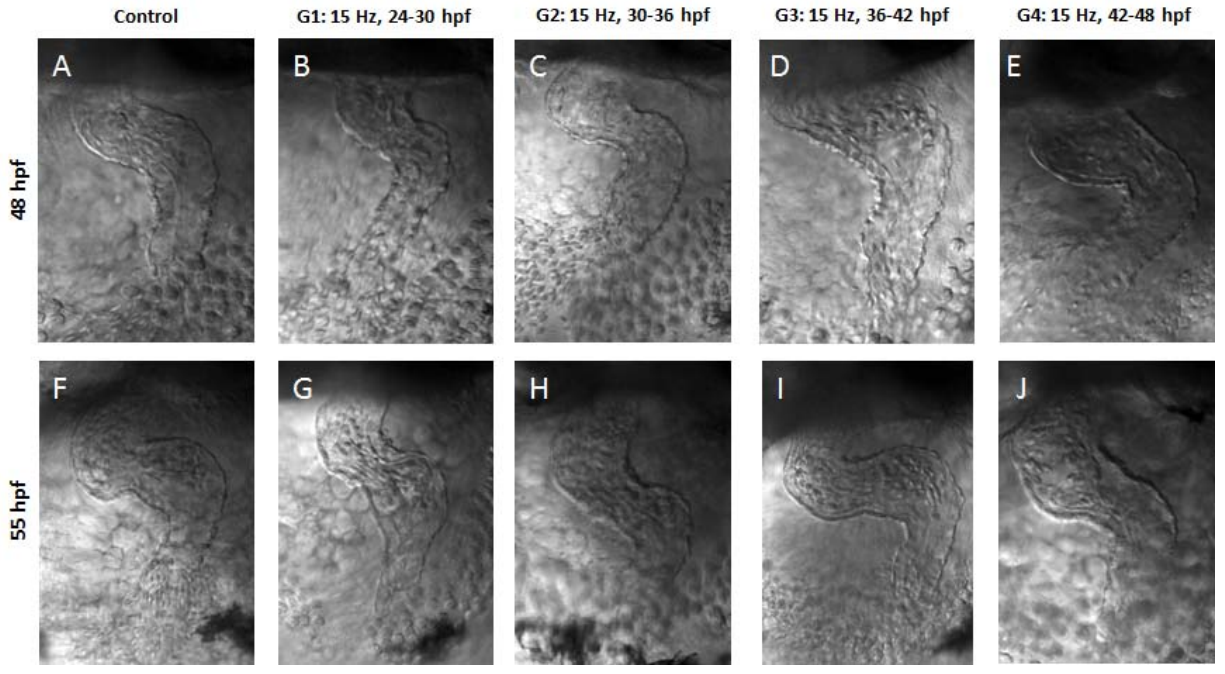

Figure 6.5 Representative Hearts at the end of Atrial Systole
Hearts with stroke volumes very near the group mean were chosen from each group. Hearts are shown at the end of systole at 48 hpf (A-E) and 55 hpf (F-J).

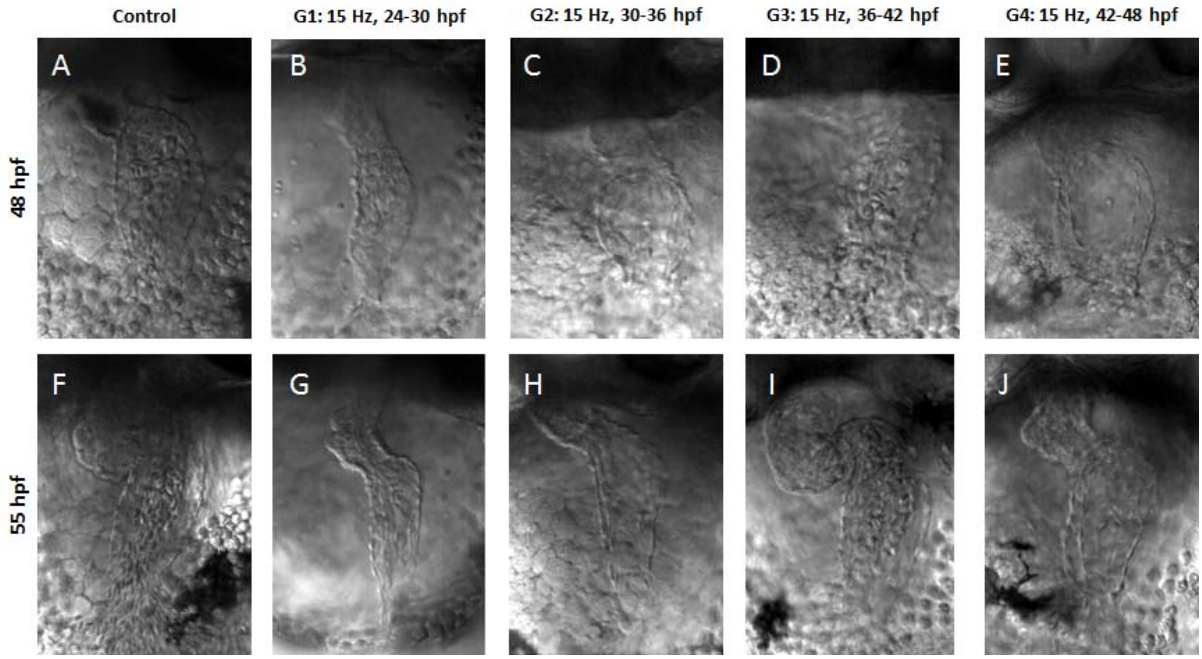

Figure 6.6 Low Performing Hearts at the end of Atrial Diastole
Hearts with the lowest stroke volume from each group are shown at 48 hpf (A-E) and 55 hpf (F-J). Impaired looping is present in G1, G2, and G4 and can most easily be seen at 55 hpf (G, H, and J). Blood cell density is similarly decreased and is especially obvious in G2 and G4.

.

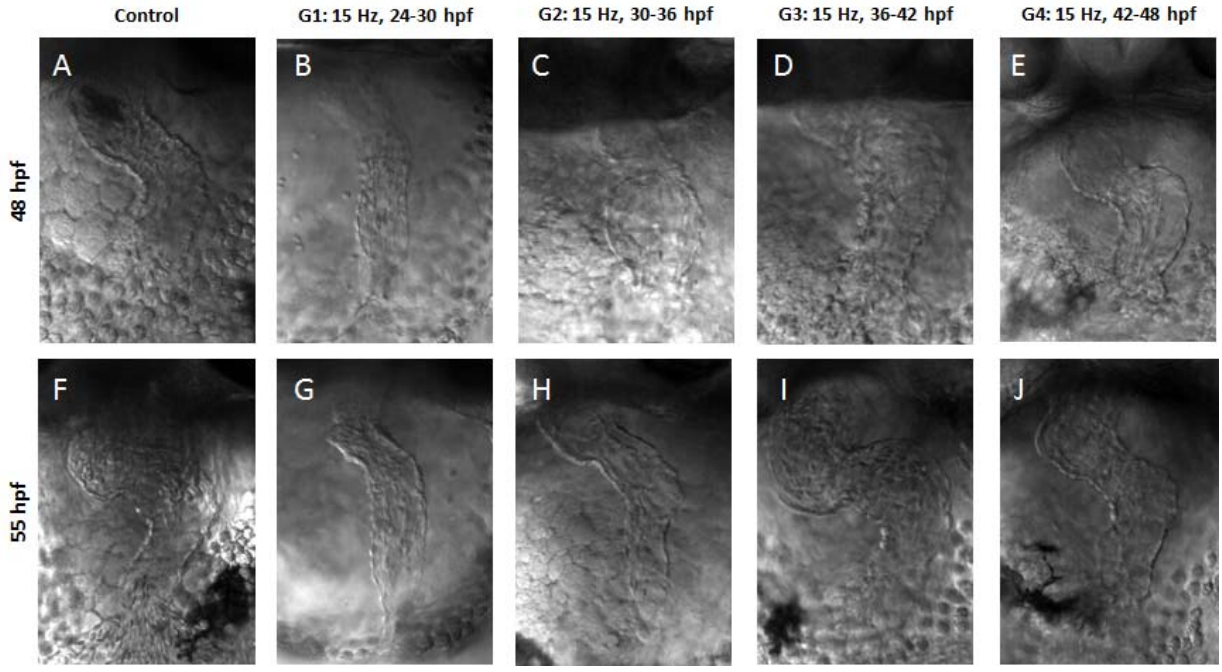

Figure 6.7 Low Performing Hearts at the end of Atrial Systole
Hearts with the lowest stroke volume from each group are shown at 48 hpf (A-E) and 55 hpf (F-J).

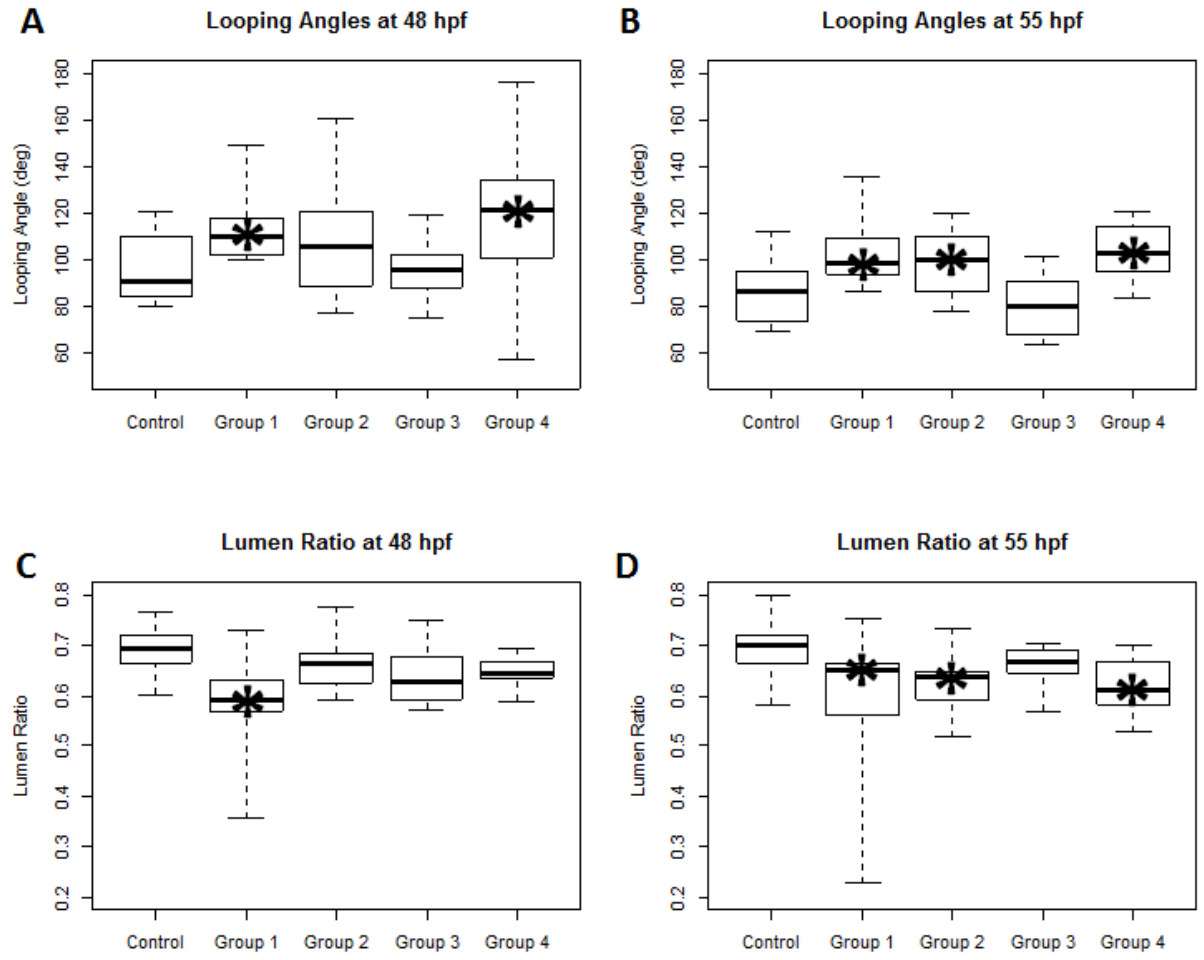

Figure 6.8 Box Plots of Looping Angle and Lumen Ratio
Asterisks (*) indicate statistical significance ($p<0.05$) versus the control group. Boxes represent data boundaries for 25th and 75th percentile. The mean for the given parameter is marked by the black bar. Whiskers extend to the most extreme data points.

6.5 Centrifugation: Blood Flow Results

The control group had an average stroke volume near 0.3 nL at 48 hpf and an average stroke volume near 0.4 at 55 hpf (Figure 6.9 A and B). Groups 1, 2, and 4 all had significantly lower ($p<0.05$) stroke volumes than the control at 48 hpf. Only Groups 1 and 2 had significantly lower stroke volumes at 55 hpf. As described in Section 5.15,

there is a correllation between the square of the inlet diameter and the flow rate (R-square = 0.54). In order to distinguish between stroke volume changes resulting from altered diameter and changes resulting from diameter-independent pumping capability, stroke volume was indexed by dividing by the square of the diameter (Figure 6.9 C and D). Similar to the raw stroke volume results, Groups 1, 2, and 4 had stroke volumes significantly lower than the control at 48 hpf. However, none of the treatment groups had indexed stroke volumes significantly different than the control at 55 hpf. Groups 1, 2, and 4 all had a much larger range for regurgitant fraction than the control at 48 hpf (Figure 6.9 E and F), but only Group 4 had a significantly higher overall value of regurgitant fraction. At 55 hpf, all groups had very low values of regurgitant fraction and none of the treatment groups were significantly different than the control.

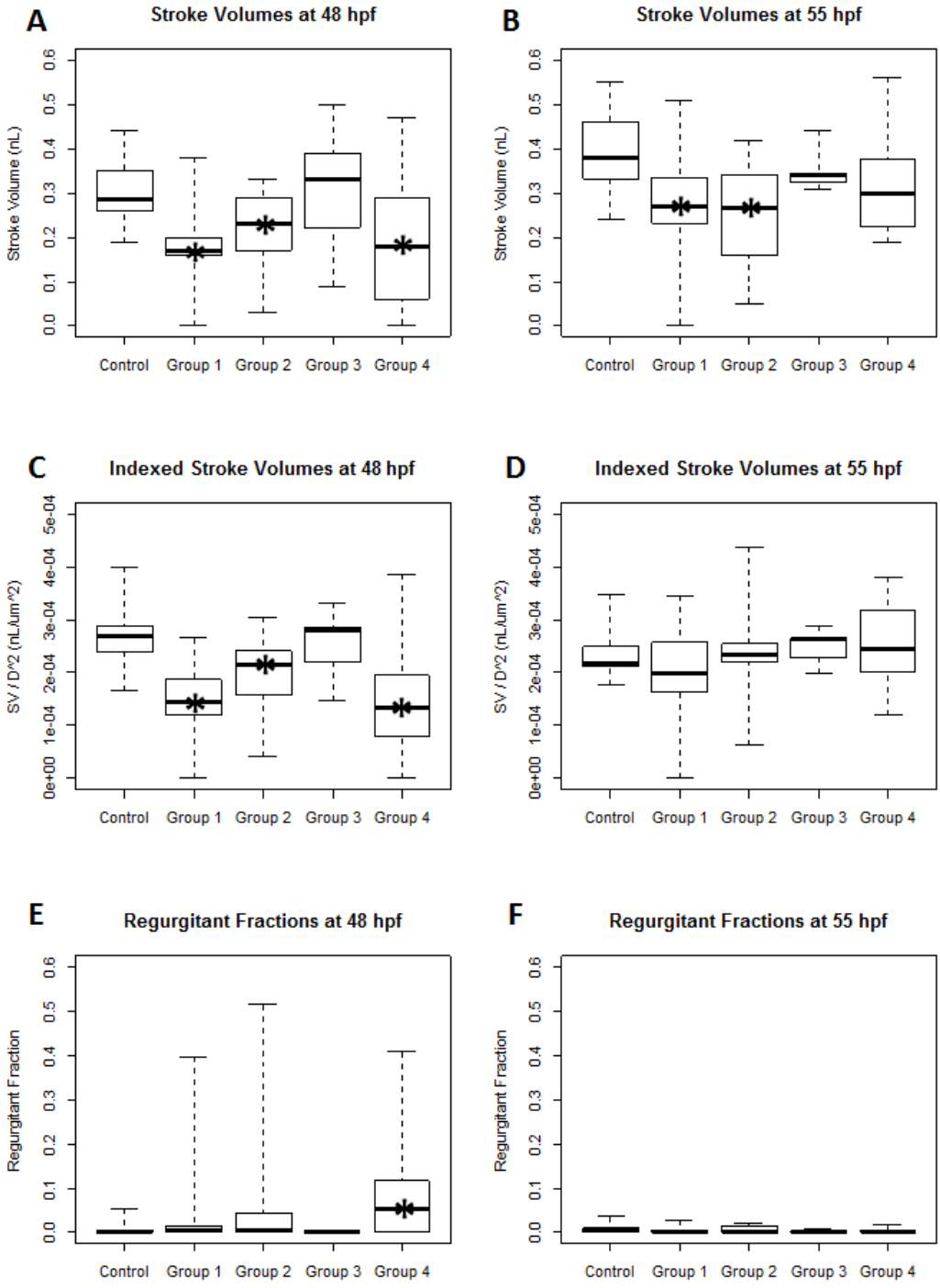

Figure 6.9 Box Plots of Stroke Volume and Regurgitant Fraction
Asterisks (*) indicate statistical significance ($p<0.05$) versus the control group. Boxes represent data boundaries for 25th and 75th percentile. The mean for the given parameter is marked by the black bar. Whiskers extend to the most extreme data points.

6.6 Centrifugation: Discussion

In the context of this study, stroke volume is perhaps the single most informative variable in describing heart function. Embryos which were rotated earlier in cardiac development had more severely impaired heart function than embryos rotated later in development. The lack of effect in Group 3, paired with the apparent recovery of stroke volume in Group 4, may be explained by the timing between treatment and observation. The centrifugation of Group 4 was applied from 42 hpf to 48 hpf, meaning that Group 4 was observed immediately following treatment. The other groups had between six and 18 hours to recover from treatment before observations were made. Centrifugation may have both temporary effects (such as blood pooling within the yolk and at the extremities) as well as long-term effects (such as alterations in gene expression and heart morphology). In this study, the initial effects lasted less than six hours; stroke volumes were not statistically different in Group 3 at 48 hpf, and the significant reduction in stroke volume in Group 4 at 48 hpf was no longer statistically significant by 55 hpf. Groups 1 and 2 were affected more permanently since stroke volumes were statistically lower than the controls at both 48 hpf and 55 hpf. This is especially noteworthy because these groups had the longest recovery times before observations were made. Based on the results observed here, altered cardiac loading at earlier time points—before and during early cardiac looping—results in longer-lasting changes in heart morphology and function compared to altered cardiac load occurring later in heart development.

Since stroke volume is based on flow rate through the cross-sectional area of the heart, it is not surprising that there is a correlation between stroke volume and the square of the atrial inlet diameter in control embryos. By indexing the stroke volume via division by the maximum atrial inlet diameter, we can investigate the question of *why* the stroke volumes were reduced in each case. If the cause of the reduced stroke volume is simply the result of a smaller heart, then the indexed stroke volumes for all groups should be similar. This was not the case at 48 hpf because Groups 1, 2, and 4 all retained statistical significance versus the control after indexing. The reduction in stroke volume was a result of factors other than the heart's size. One such factor may very well be regurgitation. The regurgitant fraction is a measure of the heart's ability to prevent backflow while pumping blood. Figure 6.9E shows that the range of regurgitant fraction values in Groups 1, 2, and 4 were all much larger than the control—at least one heart in each group reached regurgitant fractions of over 0.4. An example of this regurgitation can be seen in supplementary video SV1 (Group 4, 48 hpf).

At 55 hpf, we see a different story: none of the treatment groups have statistically different indexed stroke volumes versus the control (Figure 6.9F). This indicates that the reduced stroke volumes observed at 55 hpf are mainly a result of reduced orifice area. The reduced orifice area corresponds to the relative decrease in lumen ratio; at 55 hpf Groups 1, 2, and 4 all had significantly lower lumen ratios versus the control (Figure 6.8 C and D). The decreased lumen ratio appears to be a result of decreased atrial ballooning (easily seen in Figure 6.6 G and H). It appears that hearts were able to recover a level of function proportional to heart size by 55 hpf, as indicated by the

similarity in indexed stroke volumes (Figure 6.9D). This idea that hearts may have recovered general function is backed by the fact that all groups had very low values of regurgitation at 55 hpf (Figure 6.9F).

Looping angle was increased in Groups 1 and 4 at 48 hpf and in Groups 1, 2, and 4 at 55 hpf. Note that a larger angle reflects less cardiac looping, as the heart loops from a nearly linear tube (~180° at 24 hpf) to an s-shaped two-chambered heart (~85° at 55 hpf). Although it is unclear why the looping angle of Group 3 was unaffected by the treatment, it appears that centrifugation generally results in impaired cardiac looping. This is consistent with the impaired looping resulting from altered cardiac loading seen in previous studies [15, 61, 69].

A few central physical factors affect stroke volume: (1) the heart's contractility, (2) the efficiency of the heart, and (3) the resistance and compliance of the circulatory system. Contractility describes the ability of the heart muscle to contract. Centrifugation should have no direct effect on contractility. Here, the efficiency of the heart is referring to the ability of the heart to effectively pump blood, beyond the simple matter of how strongly the heart can contract. A heart may contract effectively, but if its valves are nonfunctional, it can result in a large amount of regurgitation which would greatly reduce stroke volume. The timing and coordination of contractions also plays an important role in the context of embryonic hearts. If the coordination of atrial and ventricular contractions are off, then the heart cannot pump blood forward to the body as effectively. This would also result in decreased stroke volume. Again, centrifugation

should not directly impact the efficiency of the heart. This leaves the resistance and compliance of the circulatory system as the key physical factors responsible for changes in stroke volume. As Figure 6.1 confirms, centrifugation draws blood from the active circulation where it pools at various places within the embryo. The ability of blood to pool is a result of the compliance of blood vessels. The compliance describes the vessels' ability to stretch under increased pressure. Resistance describes how difficult it is for blood to flow through the circulation. Centrifugation can drastically alter the resistance. If pressure differentials are altered enough, vessels within the circulation (in this case near the tail) can partially or completely collapse. This increases the resistance and can stop circulation entirely along certain vessels. Obviously these changes in flow would result in drastic changes in preload. Centrifugation is an effective means of altering loading on the heart.

6.7 Study Limitations

The opportunity for imaging the developing atrial inlet with bright field microscopy is limited to 55-65 hpf (somewhat dependent on the particular fish). Encroaching high-contrast exterior cells move anteriorly on the embryo's chest and eventually obscure the atrial inlet. Pigmentation also directly obscures the heart beyond this point, although pigmentation can be eliminated with the use of chemicals or albino fish. Because measurements could not reliably be taken of the fish at later time points, the analysis was not applied to older fish in the study. A limitation in the study design was caused by the fact that embryos were drawn at random from the pool of fish within each group.

The comparisons between 48 and 55 hpf time points are therefore not paired, and results are open to more influence from fish-fish variability. Although embryos were all identically positioned at the start of the rotation experiment, the near spherical shape of the body makes it possible for the embryo to turn within the plastic tubing and can lead to orientations other than those indicated in Figure 6.2. It is unknown how big of a role orientation plays, as blood can theoretically pool in any position. Observations of transgenic embryos immediately following rotation confirmed that all embryos had pooled blood in the yolk sack as well as the head or tail (data not shown). Alignment of embryos in a particular direction may therefore be unnecessary to achieve reductions in cardiac preload.

6.8 Chapter Summary

In this chapter, a new model has been presented for altering cardiac loading in the zebrafish embryo. Centrifugation is far less invasive than previously used methods and resulted in similar changes in heart development. Its main advantage is the ease and precision of starting and ceasing the treatment, which allows for the investigation of treatment timing as a variable. To my knowledge, the effect of treatment timing has not been previously studied to the extent presented here.

Interesting conclusions can be made from these results. First, low-speed centrifugation was shown to be an effective method for inducing cardiac irregularities in embryos without causing noticeable damage to the embryo as a whole. Rotation resulted in

hearts with impaired cardiac looping, impaired chamber ballooning, and reduced capacity to pump blood. The lack of effect seen in Group 3, paired with the significant recovery of function in Group 4, indicates that cardiac function can recover relatively quickly from the effects of altered loading applied during mid to late looping. Since this recovery in cardiac function was not seen in Groups 1 and 2—even though these groups had a significantly longer recovery time—there is strong evidence to suggest that altered cardiac loading at earlier time points has a greater and longer-lasting effect than altered loading at later time points. Treatment groups were not observed beyond 55 hpf but it is conceivable that this decrease in function may persist for the long term.

CHAPTER 7: FUTURE WORK

7.1 Chapter Introduction

There is still much to be learned in the area of epigenetics and heart development. There are multiple ways to approach the topic which span the fields of biology, engineering, computer science, and physics. Some of the future directions of this research will be presented here.

7.2 Continued Centrifugation Studies

The experiments in Aim 3 were designed as a pilot experiment to probe the idea of timing of altered loading as a variable in defect development. There are many ways to vary the experiment setup to extract more information. Groups 1 and 2 yielded similar results for most of the variables tested. This may indicate that the true critical time window lies in between the two groups. This could be tested by simply incorporating more timing windows into the study (e.g. rotating 15 Hz from 27-33 hpf). The length of rotation time can be altered to gain insight into exactly what the timing window is; it is difficult to say whether there is a particularly import small window of time that is important or if any alterations during early heart development have a similar effect. By expanding or narrowing the centrifugation timing window, this question could easily be answered. Other variables such as rotation rate and embryo orientation could also be investigated.

A crucial aspect to investigate in future studies is the persistence of reduced cardiac function after centrifugation. Because of the limitations caused by both the embryo's anatomy and the imaging equipment, a full analysis could not be performed beyond 55 hpf. However, any observations of the heart at later time points would be useful in assessing the lasting effects of centrifugation. Unlike the experiment performed for Aim 3, all samples should be paired across time points so that individual defect development could be observed. One approach is to use transgenic fish with fluorescent heart walls and/or blood cells (e.g. the Tg(*fli1a*:eGFP)^{y1} Tg(gata1:mRFP)^{ko5} line [106]). When observed under fluorescence microscopy, the heart and blood can be observed—even through tissue which would otherwise obscure the view of the heart under bright field microscopy. In an informal test experiment, I followed a centrifuged (15 Hz 30-36 hpf) transgenic fish out to 7 days post-fertilization and there appeared to be continued regurgitant flow through the atrioventricular junction beyond the time in which the control embryo had apparently developed a fully-functional AV valve. Finally, as with any experiment, a larger sample sizes would be beneficial and would help eliminate or explain confounding results.

7.3 Gene Expression Studies

Altered gene expression is the accepted cause of the defects witnessed in various studies on altered mechanical stress. It is therefore critical to investigate gene expression in order to fully understand how congenital defects occur. There are many genes involved in heart development and several of these genes have been linked to

shear stress and valve development. It could be very enlightening to look at changes in the expression of these genes at various points after centrifugation.

It may particularly useful to apply transcriptomics in order to learn more about gene expression. This provides a look at all of the RNA associated with a group of cells (in this case the heart, or even a specific portion of the heart) and is an indication of the gene expression occurring at a given time. Rather than testing for the expression of a particular gene of interest, this provides a look at *all* genes being expressed—a very powerful tool for discovering important genes. Assays could be applied before and after centrifugation, or applied to controls vs. centrifuged embryos in order to determine gene expression changes associated with the treatment. This could help elucidate the genetic origins of any associated heart defects.

7.4 Computational Fluid Dynamics

CFD simulates fluid flow using a computer model. When the boundary conditions are well-defined, CFD can provide very accurate simulations of the flow. In order to accurately define the 3D boundary conditions, more advanced imaging (e.g. confocal microscopy) would likely be needed. This could be incredibly useful for understanding the changes in shear stress and pressure that result from the altered cardiac morphology seen in the centrifugation studies.

CHAPTER 8: CONCLUSION

At the beginning of this project, I aimed to investigate the effect of mechanical loading on the zebrafish embryo. Although many studies had observed morphological changes as a result of altered loading, none had looked closely at the role the timing of altered loading—a variable that could be of significant influence. I aimed to determine if in fact there are periods of time in development in which altered loading induces lasting cardiac defects. This problem was approached by first developing the infrastructure in which to test it. A methodology was developed to quantify heart function from high speed bright field image sequences. This methodology yields more extensive measurements of heart function than has previously been shown in a zebrafish embryo, and provides both general measures of heart function (e.g. stroke volume) as well as more detailed, time resolved measurements (e.g. instantaneous flow rate vs. time). A new method for altering cardiac loading was also developed, in which embryos are rotated at low frequencies to induce reductions in cardiac preload. This method is far less invasive than those previously used, and the treatment can be applied and stopped at will. This permits the investigation of the timing of cardiac loading on development. Treatment groups were compared to control embryos using the developed methodology, and this led to enlightening results:

- Centrifugation resulted in lasting changes in cardiac morphology, including impaired looping and thinner chambers.

- Embryos treated at earlier time windows had reduced stroke volumes versus control embryos.
- Embryos treated during mid-late looping had very few changes in any parameters when compared to controls.
- Embryos treated at the end of cardiac looping had temporary reductions in stroke volume and temporary increases in regurgitant fraction. These effects were no longer statistically significant at the 55 hpf time point.
- The persistence of decreased heart function in earlier treatment groups paired with the recovery of function in later treatment groups supports the main hypothesis; altered loading at earlier time points appears to induce more severe, longer-lasting effects than altered loading applied at later time points.

This research may prove to be very beneficial in the future, as the methods developed here can be applied to future studies. Also, further centrifugation studies can be paired with gene expression studies to determine which genes play a role in the altered development observed here. This may ultimately lead to a better understanding of the role of epigenetic factors on heart development.

CHAPTER 9: ORIGINAL CONTRIBUTIONS

9.1 Peer-Reviewed Publications

BM Johnson, DM Garrity, LP Dasi. “Quantifying Function in the Early Embryonic Heart.” Journal of Biomechanical Engineering-Transactions of the ASME, 2013. 135(4).

BM Johnson, DM Garrity, LP Dasi. “The Transitional Cardiac Pumping Mechanics of the Embryonic Heart.” Journal of Cardiovascular Engineering and Technology. January, 2013.

C Lacerda, J Kisiday, BM Johnson, EC Orton. “Local serotonin mediates cyclic strain-induced phenotype transformation, matrix degradation, and glycosaminoglycan synthesis in cultured sheep mitral valves” American Journal of Physiology, Heart and Circulatory Physiology. January, 2012.

9.2 Conference Publications

BW Schroder, BM Johnson, DM Garrity, LP Dasi, D Krapf. “Force Spectroscopy in the Bloodstream of Live Embryonic Zebrafish with Optical Tweezers. American Physical Society, Division of Laser Science, OSA Frontiers in Optics. Submitted May 19, 2014.

BM Johnson, DM Garrity, LP Dasi. “The Brine Shrimp’s Butterfly Stroke.” American Physical Society, Division of Fluid Dynamics Gallery of Fluid Motion. Submitted October 18, 2011. arXiv:1110.4007. http://arxiv.org/abs/1110.4007

9.3 Conference/Seminar Oral Presentations

65th Annual Meeting of the American Physical Society’s Division of Fluid Dynamics. “A Methodology for Quantifying Heart Function in the Embryonic Zebrafish.” November 18-20, 2012. San Diego, CA.

CSU School of Biomedical Engineering Seminar, “Quantifying Heart Function in the Embryonic Zebrafish.” February 4, 2013. Fort Collins, CO.

CSU School of Biomedical Engineering Seminar, “Investigating the Biomechanics of the Developing Zebrafish Heart.” April 18, 2011. Fort Collins, CO.

63rd Annual Meeting of the American Physical Society's Division of Fluid Dynamics "Investigating the Flow and Biomechanics of the Embryonic Zebrafish Heart." November 21-23, 2010. Long Beach, CA.

9.4 Conference Poster/Video Presentations

2013 Colorado State University Research Colloquium. Poster: "Quantifying heart function in the Embryonic Zebrafish." April 4-5, 2013. Fort Collins, CO.

ASME 2012 Summer Bioengineering Conference. Poster: "Quantifying the Biomechanics of the Embryonic Zebrafish Heart." June 20-23, 2012. Fajardo, Puerto Rico.

64th Annual Meeting of the American Physical Society's Division of Fluid Dynamics, Gallery of Fluid Motion. Video: "The Brine Shrimp's Butterfly Stroke." November 20-22, 2011. Baltimore, MD.

9.5 Publications in Progress

Two more publications are very likely to result from my graduate work:

The results presented in Aim 3 will be submitted for peer review in July 2014.

We have demonstrated the first use of optical tweezers for the measurement of blood forces in the live zebrafish embryo. The preliminary results will be submitted as a methods paper, likely in July 2014.

REFERENCES

1. Go, A.S., et al., *Heart Disease and Stroke Statistics-2014 Update A Report From the American Heart Association.* Circulation, 2014. **129**(3): p. E28-E292.

2. Blue, G.M., et al., *Congenital heart disease: current knowledge about causes and inheritance.* Medical Journal of Australia, 2012. **197**(3): p. 155-159.

3. Pierpont, M.E., et al., *Genetic basis for congenital heart defects: Current knowledge - A scientific statement from the American heart association congenital cardiac defects committee, council on cardiovascular disease in the young.* Circulation, 2007. **115**(23): p. 3015-3038.

4. Parrie, L.E., et al., *Zebrafish tbx5 Paralogs Demonstrate Independent Essential Requirements in Cardiac and Pectoral Fin Development.* Developmental Dynamics, 2013. **242**(5): p. 485-502.

5. Chi, N.C., et al., *Cardiac conduction is required to preserve cardiac chamber morphology.* Proceedings of the National Academy of Sciences of the United States of America, 2010. **107**(33): p. 14662-14667.

6. Granados-Riveron, J.T. and J.D. Brook, *The Impact of Mechanical Forces in Heart Morphogenesis.* Circulation-Cardiovascular Genetics, 2012. **5**(1): p. 132-142.

7. McCain, M.L. and K.K. Parker, *Mechanotransduction: the role of mechanical stress, myocyte shape, and cytoskeletal architecture on cardiac function.* Pflugers Archiv-European Journal of Physiology, 2011. **462**(1): p. 89-104.

8. Santhanakrishnan, A. and L.A. Miller, *Fluid Dynamics of Heart Development.* Cell Biochemistry and Biophysics, 2011. **61**(1): p. 1-22.

9. Zhou, Y.Q., et al., *Applications for multifrequency ultrasound biomicroscopy in mice from implantation to adulthood.* Physiological Genomics, 2002. **10**(2): p. 113-126.

10. Wu, M.M. and T.N. Sato, *On the Mechanics of Cardiac Function of Drosophila Embryo.* Plos One, 2008. **3**(12).

11. Jones, E.A.V., et al., *Measuring hemodynamic changes during mammalian development.* American Journal of Physiology-Heart and Circulatory Physiology, 2004. **287**(4): p. H1561-H1569.

12. Al Naieb, S., C.M. Happel, and T.M. Yelbuz, *A detailed atlas of chick heart development in vivo.* Annals of Anatomy-Anatomischer Anzeiger, 2013. **195**(4): p. 324-341.

13. Groenendijk, B.C.W., et al., *The role of shear stress on ET-1, KLF2, and NOS-3 expression in the developing cardiovascular system of chicken embryos in a venous Ligation model.* Physiology, 2007. **22**(6): p. 380-389.

14. Icardo, J.M., *Endocardial cell arrangement - Role of hemodynamics.* Anatomical Record, 1989. **225**(2): p. 150-155.

15. Hogers, B., et al., *Extraembryonic venous obstructions lead to cardiovascular malformations and can be embryolethal.* Cardiovascular Research, 1999. **41**(1): p. 87-99.

16. Liu, A.P., et al., *Quantifying blood flow and wall shear stresses in the outflow tract of chick embryonic hearts.* Computers & Structures, 2011. **89**(11-12): p. 855-867.

17. Liu, A.P., et al., *Biomechanics of the Chick Embryonic Heart Outflow Tract at HH18 Using 4D Optical Coherence Tomography Imaging and Computational Modeling.* Plos One, 2012. **7**(7).

18. Hamburger, V. and H.L. Hamilton, *A SERIES OF NORMAL STAGES IN THE DEVELOPMENT OF THE CHICK EMBRYO.* Journal of Morphology, 1951. **88**(1): p. 49-&.

19. Chan, J. and J.D. Mably, *Dissection of Cardiovascular Development and Disease Pathways in Zebrafish*, in *Animal Models of Human Disease*, K.T. Chang and K.T. Min, Editors. 2011. p. 111-153.

20. Stainier, D.Y.R., R.K. Lee, and M.C. Fishman, *Cardiovascular development in the zebrafish 1. Myocardial fate map and heart tube formation.* Development, 1993. **119**(1): p. 31-40.

21. Thisse, C. and L.I. Zon, *Development - Organogenesis - Heart and wood formation from the zebrafish point of view.* Science, 2002. **295**(5554): p. 457-462.

22. Goenezen, S., M.Y. Rennie, and S. Rugonyi, *Biomechanics of early cardiac development.* Biomechanics and Modeling in Mechanobiology, 2012. **11**(8): p. 1187-1204.

23. Driever, W., et al., *A genetic screen for mutations affecting embryogenesis in zebrafish.* Development, 1996. **123**: p. 37-46.

24. Poon, K.L., et al., *Zebrafish Cardiac Enhancer Trap Lines: New Tools for In Vivo Studies of Cardiovascular Development and Disease.* Developmental Dynamics, 2010. **239**(3): p. 914-926.

25. Lawson, N.D. and B.M. Weinstein, *In vivo imaging of embryonic vascular development using transgenic zebrafish.* Developmental Biology, 2002. **248**(2): p. 307-318.

26. Long, Q.M., et al., *GATA-1 expression pattern can be recapitulated in living transgenic zebrafish using GFP reporter gene.* Development, 1997. **124**(20): p. 4105-4111.

27. Garrity, D.M., S. Childs, and M.C. Fishman, *The heartstrings mutation in zebrafish causes heart/fin Tbx5 deficiency syndrome.* Development, 2002. **129**(19): p. 4635-4645.

28. Sehnert, A.J., et al., *Cardiac troponin T is essential in sarcomere assembly and cardiac contractility.* Nature Genetics, 2002. **31**(1): p. 106-110.

29. Beis, D., et al., *Genetic and cellular analyses of zebrafish atrioventricular cushion and valve development.* Development, 2005. **132**(18): p. 4193-4204.

30. Beis, D. and D.Y.R. Stainier, *In vivo cell biology: following the zebrafish trend.* Trends in Cell Biology, 2006. **16**(2): p. 105-112.

31. Harvey, R.P., *Patterning the vertebrate heart.* Nature Reviews Genetics, 2002. **3**(7): p. 544-556.

32. Lieschke, G.J. and P.D. Currie, *Animal models of human disease: zebrafish swim into view.* Nature Reviews Genetics, 2007. **8**(5): p. 353-367.

33. Scherz, P.J., et al., *High-speed imaging of developing heart valves reveals interplay of morphogenesis and function.* Development, 2008. **135**(6): p. 1179-1187.

34. Liu, J.D. and D.Y.R. Stainier, *Zebrafish in the Study of Early Cardiac Development.* Circulation Research, 2012. **110**(6): p. 870-874.

35. Gittenberger-De Groot, A.C., et al., *Basics of cardiac development for the understanding of congenital heart malformations.* Pediatric Research, 2005. **57**(2): p. 169-176.

36. Bakkers, J., *Zebrafish as a model to study cardiac development and human cardiac disease.* Cardiovascular Research, 2011. **91**(2): p. 279-288.

37. Liebling, M., et al., *Rapid three-dimensional imaging and analysis of the beating embryonic heart reveals functional changes during development.* Developmental Dynamics, 2006. **235**(11): p. 2940-2948.

38. Staudt, D. and D. Stainier, *Uncovering the Molecular and Cellular Mechanisms of Heart Development Using the Zebrafish*, in *Annual Review of Genetics, Vol 46*, B.L. Bassler, Editor 2012. p. 397-418.

39. Manner, J., A. Wessel, and T.M. Yelbuz, *How Does the Tubular Embryonic Heart Work? Looking for the Physical Mechanism Generating Unidirectional Blood Flow in the Valveless Embryonic Heart Tube.* Developmental Dynamics, 2010. **239**(4): p. 1035-1046.

40. Jaffrin, M.Y. and A.H. Shapiro, *Peristaltic Pumping.* Annual Review of Fluid Mechanics, 1971. **3**: p. 13-&.

41. Forouhar, A.S., et al., *The embryonic vertebrate heart tube is a dynamic suction pump.* Science, 2006. **312**(5774): p. 751-753.

42. Avrahami, I. and M. Gharib, *Computational studies of resonance wave pumping in compliant tubes.* Journal of Fluid Mechanics, 2008. **608**: p. 139-160.

43. Hickerson, A.I., D. Rinderknecht, and M. Gharib, *Experimental study of the behavior of a valveless impedance pump.* Experiments in Fluids, 2005. **38**(4): p. 534-540.

44. Loumes, L., I. Avrahami, and M. Gharib, *Resonant pumping in a multilayer impedance pump.* Physics of Fluids, 2008. **20**(2): p. 11.

45. Maes, F., et al. *The Pumping Mechanism of Embryonic Hearts*. in *5th European Conference of the International Federation for Medical and Biological Engineering*. 2011. Budapest, HUNGARY.

46. Johnson, B.M., D.M. Garrity, and L.P. Dasi, *The Transitional Cardiac Pumping Mechanics in the Embryonic Heart.* Cardiovascular Engineering and Technology, 2013.

47. Davies, P.F., et al., *Influence of hemodynamic forces on vascular endothelial function - in vitro studies of shear stress and pinocytosis in bovine aortic cells.* Journal of Clinical Investigation, 1984. **73**(4): p. 1121-1129.

48. Vermot, J., et al., *Reversing Blood Flows Act through klf2a to Ensure Normal Valvulogenesis in the Developing Heart.* Plos Biology, 2009. **7**(11).

49. Replogle, R.L., Meiselma.Hj, and E.W. Merrill, *Clinical implications of blood rheology studies.* Circulation, 1967. **36**(1): p. 148-&.

50. Fish, R.J., et al., *Developmental expression and organisation of fibrinogen genes in the zebrafish.* Thrombosis and Haemostasis, 2012. **107**(1): p. 158-166.

51. Davies, P.F. and S.C. Tripathi, *Mechanical stress mechanisms and the cell - an endothelial paradigm.* Circulation Research, 1993. **72**(2): p. 239-245.

52. Topper, J.N. and M.A. Gimbrone, *Blood flow and vascular gene expression: fluid shear stress as a modulator of endothelial phenotype.* Molecular Medicine Today, 1999. **5**(1): p. 40-46.

53. Davies, P.F., et al., *Turbulent fluid shear stress induces vascular endothelial cell turnover in vitro.* Proceedings of the National Academy of Sciences of the United States of America, 1986. **83**(7): p. 2114-2117.

54. Dewey, C.F., et al., *The dynamic response of vascular endothelial cells to fluid shear stress.* Journal of Biomechanical Engineering-Transactions of the Asme, 1981. **103**(3): p. 177-185.

55. Helmlinger, G., et al., *Effects of pulsatile flow on cultured vascular endothelial cell morphology.* Journal of Biomechanical Engineering-Transactions of the Asme, 1991. **113**(2): p. 123-131.

56. Papadaki, M., L.V. McIntire, and S.G. Eskin, *Effects of shear stress on the growth kinetics of human aortic smooth muscle cells in vitro.* Biotechnology and Bioengineering, 1996. **50**(5): p. 555-561.

57. Stamatas, G.N., C.W. Patrick, and L.V. McIntire, *Intracellular pH changes of human aortic smooth muscle cells in response to fluid shear stress.* Tissue Engineering, 1997. **3**(4): p. 391-403.

58. Thi, M.M., et al., *The role of the glycocalyx in reorganization of the actin cytoskeleton under fluid shear stress: A "bumper-car" model.* Proceedings of the National Academy of Sciences of the United States of America, 2004. **101**(47): p. 16483-16488.

59. Li, C.H. and Q.B. Xu, *Mechanical stress-initiated signal transduction in vascular smooth muscle cells in vitro and in vivo.* Cellular Signalling, 2007. **19**(5): p. 881-891.

60. Schroder, E.A., et al., *Microtubule involvement in the adaptation to altered mechanical load in developing chick myocardium.* Circulation Research, 2002. **91**(4): p. 353-359.

61. Broekhuizen, M.L.A., et al., *Altered hemodynamics in chick embryos after extraembryonic venous obstruction.* Ultrasound in Obstetrics & Gynecology, 1999. **13**(6): p. 437-445.

62. Hogers, B., et al., *Unilateral vitelline vein ligation alters intracardiac blood flow patterns and morphogenesis in the chick embryo.* Circulation Research, 1997. **80**(4): p. 473-481.

63. Reckova, M., et al., *Hemodynamics is a key epigenetic factor in development of the cardiac conduction system.* Circulation Research, 2003. **93**(1): p. 77-85.

64. Tobita, K., et al., *Three-dimensional myofiber architecture of the embryonic left ventricle during normal development and altered mechanical loads.* Anatomical Record Part a-Discoveries in Molecular Cellular and Evolutionary Biology, 2005. **283A**(1): p. 193-201.

65. Filas, B.A., I.R. Efimov, and L.A. Taber, *Optical coherence tomography as a tool for measuring morphogenetic deformation of the looping heart.* Anatomical Record-Advances in Integrative Anatomy and Evolutionary Biology, 2007. **290**(9): p. 1057-1068.

66. Nerurkar, N.L., A. Ramasubramanian, and L.A. Taber, *Morphogenetic adaptation of the looping embryonic heart to altered mechanical loads.* Developmental Dynamics, 2006. **235**(7): p. 1822-1829.

67. Voronov, D.A., et al., *The role of mechanical forces in dextral rotation during cardiac looping in the chick embryo.* Developmental Biology, 2004. **272**(2): p. 339-350.

68. Voronov, D.A. and L.A. Taber, *Cardiac looping in experimental conditions: Effects of extraembryonic forces.* Developmental Dynamics, 2002. **224**(4): p. 413-421.

69. Hove, J.R., et al., *Intracardiac fluid forces are an essential epigenetic factor for embryonic cardiogenesis.* Nature, 2003. **421**(6919): p. 172-177.

70. Malone, M.H., et al., *Laser-scanning velocimetry: A confocal microscopy method for quantitative measurement of cardiovascular performance in zebrafish embryos and larvae.* Bmc Biotechnology, 2007. **7**.

71. Yalcin, H.C., et al., *Hemodynamic Patterning of the Avian Atrioventricular Valve.* Developmental Dynamics, 2011. **240**(1): p. 23-35.

72. Groenendijk, B.C.W., et al., *Development-related changes in the expression of shear stress responsive genes KLF-2, ET-1, and NOS-3 in the developing cardiovascular system of chicken embryos.* Developmental Dynamics, 2004. **230**(1): p. 57-68.

73. Groenendijk, B.C.W., et al., *Changes in shear stress-related gene expression after experimentally altered venous return in the chicken embryo.* Circulation Research, 2005. **96**(12): p. 1291-1298.

74. Mammoto, A., T. Mammoto, and D.E. Ingber, *Mechanosensitive mechanisms in transcriptional regulation.* Journal of Cell Science, 2012. **125**(13): p. 3061-3073.

75. Chen, C.Y., et al., *Time-resolved OCT-mu PIV: a new microscopic PIV technique for noninvasive depth-resolved pulsatile flow profile acquisition.* Experiments in Fluids, 2013. **54**(1).

76. Chen, Q., et al., *Haemodynamics-Driven Developmental Pruning of Brain Vasculature in Zebrafish.* Plos Biology, 2012. **10**(8).

77. Gu, S., et al., *Optical coherence tomography captures rapid hemodynamic responses to acute hypoxia in the cardiovascular system of early embryos.* Developmental Dynamics, 2012. **241**(3): p. 534-544.

78. Jenkins, M.W., M. Watanabe, and A.M. Rollins, *Longitudinal Imaging of Heart Development With Optical Coherence Tomography.* Ieee Journal of Selected Topics in Quantum Electronics, 2012. **18**(3): p. 1166-1175.

79. Li, P. and R.K.K. Wang, *Optical coherence tomography provides an ability to assess mechanical property of cardiac wall of developing outflow tract in embryonic heart in vivo.* Journal of Biomedical Optics, 2012. **17**(12).

80. Liu, A.P., et al., *Efficient postacquisition synchronization of 4-D nongated cardiac images obtained from optical coherence tomography: application to 4-D reconstruction of the chick embryonic heart.* Journal of Biomedical Optics, 2009. **14**(4).

81. Jamison, R.A., A. Fouras, and R.J. Bryson-Richardson, *Cardiac-phase filtering in intracardiac particle image velocimetry.* Journal of Biomedical Optics, 2012. **17**(3): p. 7.

82. Drew, P.J., et al., *Rapid determination of particle velocity from space-time images using the Radon transform.* Journal of Computational Neuroscience, 2010. **29**(1-2): p. 5-11.

83. Japee, S.A., R.N. Pittman, and C.G. Ellis, *A new video image analysis system to study red blood cell dynamics and oxygenation in capillary networks.* Microcirculation, 2005. **12**(6): p. 489-506.

84. Japee, S.A., R.N. Pittman, and C.G. Ellis, *Automated method for tracking individual red blood cells within capillaries to compute velocity and oxygen saturation.* Microcirculation, 2005. **12**(6): p. 507-515.

85. Pan, X.T., et al., *Characterization of flow direction in microchannels and zebrafish blood vessels by scanning fluorescence correlation spectroscopy.* Journal of Biomedical Optics, 2007. **12**(1).

86. Tam, J., J.A. Martin, and A. Roorda, *Noninvasive Visualization and Analysis of Parafoveal Capillaries in Humans.* Investigative Ophthalmology & Visual Science, 2010. **51**(3): p. 1691-1698.

87. Tam, J. and A. Roorda, *Speed quantification and tracking of moving objects in adaptive optics scanning laser ophthalmoscopy.* Journal of Biomedical Optics, 2011. **16**(3).

88. Tam, J., A. Roorda, and Ieee, *Enhanced detection of cell paths in spatiotemporal plots for noninvasive microscopy of the human retina*, in *2010 7th Ieee International Symposium on Biomedical Imaging: from Nano to Macro*2010. p. 584-587.

89. Duncan, D.D., et al., *Absolute blood velocity measured with a modified fundus camera.* Journal of Biomedical Optics, 2010. **15**(5).

90. Lee, J., et al., *Moving Domain Computational Fluid Dynamics to Interface with an Embryonic Model of Cardiac Morphogenesis.* Plos One, 2013. **8**(8).

91. Jamison, R.A., et al., *In Vivo Wall Shear Measurements within the Developing Zebrafish Heart.* Plos One, 2013. **8**(10).

92. Poelma, C., et al., *Accurate Blood Flow Measurements: Are Artificial Tracers Necessary?* Plos One, 2012. **7**(9).

93. Westerfield, M., *The Zebrafish Book*, 1995, University of Oregon Press: Eugene, OR.

94. Kimmel, C.B., et al., *Stages of embryonic development of the zebrafish.* Developmental Dynamics, 1995. **203**(3): p. 253-310.

95. Kopp, R., B. Pelster, and T. Schwerte, *How does blood cell concentration modulate cardiovascular parameters in developing zebrafish (Danio rerio)?* Comparative Biochemistry and Physiology a-Molecular & Integrative Physiology, 2007. **146**(3): p. 400-407.

96. Denvir, M.A., C.S. Tucker, and J.J. Mullins, *Systolic and diastolic ventricular function in zebrafish embryos: Influence of norepenephrine, MS-222 and temperature.* Bmc Biotechnology, 2008. **8**.

97. Wilson, J.M., R.M. Bunte, and A.J. Carty, *Evaluation of Rapid Cooling and Tricaine Methanesulfonate (MS222) as Methods of Euthanasia in Zebrafish (Danio rerio).* Journal of the American Association for Laboratory Animal Science, 2009. **48**(6): p. 785-789.

98. Lin, Y.F., I. Swinburne, and D. Yelon, *Multiple influences of blood flow on cardiomyocyte hypertrophy in the embryonic zebrafish heart.* Developmental Biology, 2012. **362**(2): p. 242-253.

99. Petzold, A.M., et al., *SCORE Imaging: Specimen in a Corrected Optical Rotational Enclosure.* Zebrafish, 2010. **7**(2): p. 149-154.

100. Schwerte, T. and B. Pelster, *Digital motion analysis as a tool for analysing the shape and performance of the circulatory system in transparent animals.* Journal of Experimental Biology, 2000. **203**(11): p. 1659-1669.

101. Johnson, B.M., D.M. Garrity, and L.P. Dasi, *Quantifying Function in the Early Embryonic Heart.* Journal of Biomechanical Engineering-Transactions of the Asme, 2013. **135**(4).

102. Bagatto, B. and W. Burggren, *A three-dimensional functional assessment of heart and vessel development in the larva of the zebrafish (Danio rerio).* Physiological and Biochemical Zoology, 2006. **79**(1): p. 194-201.

103. Hickerson, A.I. and M. Gharib, *On the resonance of a pliant tube as a mechanism for valveless pumping.* Journal of Fluid Mechanics, 2006. **555**: p. 141-148.

104. Taber, L.A., J.M. Zhang, and R. Perucchio, *Computational model for the transition from peristaltic to pulsatile flow in the embryonic heart tube.* Journal of Biomechanical Engineering-Transactions of the Asme, 2007. **129**(3): p. 441-449.

105. Bhat, S., J. Ohn, and M. Liebling, *Motion-Based Structure Separation for Label-Free High-Speed 3-D Cardiac Microscopy.* Ieee Transactions on Image Processing, 2012. **21**(8): p. 3638-3647.

106. Iida, A., et al., *Metalloprotease-Dependent Onset of Blood Circulation in Zebrafish.* Current Biology, 2010. **20**(12): p. 1110-1116.